10-19

SANDIA REPORT

SAND95–1546 • UC–814
Unlimited Release
Printed September 1995

Yucca Mountain Site Characterization Project

Alternative Conceptual Models and Codes for Unsaturated Flow in Fractured Tuff: Preliminary Assessments for GWTT-95

Clifford K. Ho, Susan J. Altman, Bill W. Arnold

Prepared by
Sandia National Laboratories
Albuquerque, New Mexico 87185 and Livermore, California 94550
for the United States Department of Energy
under Contract DE-AC04-94AL85000

Approved for public release; distribution is unlimited.

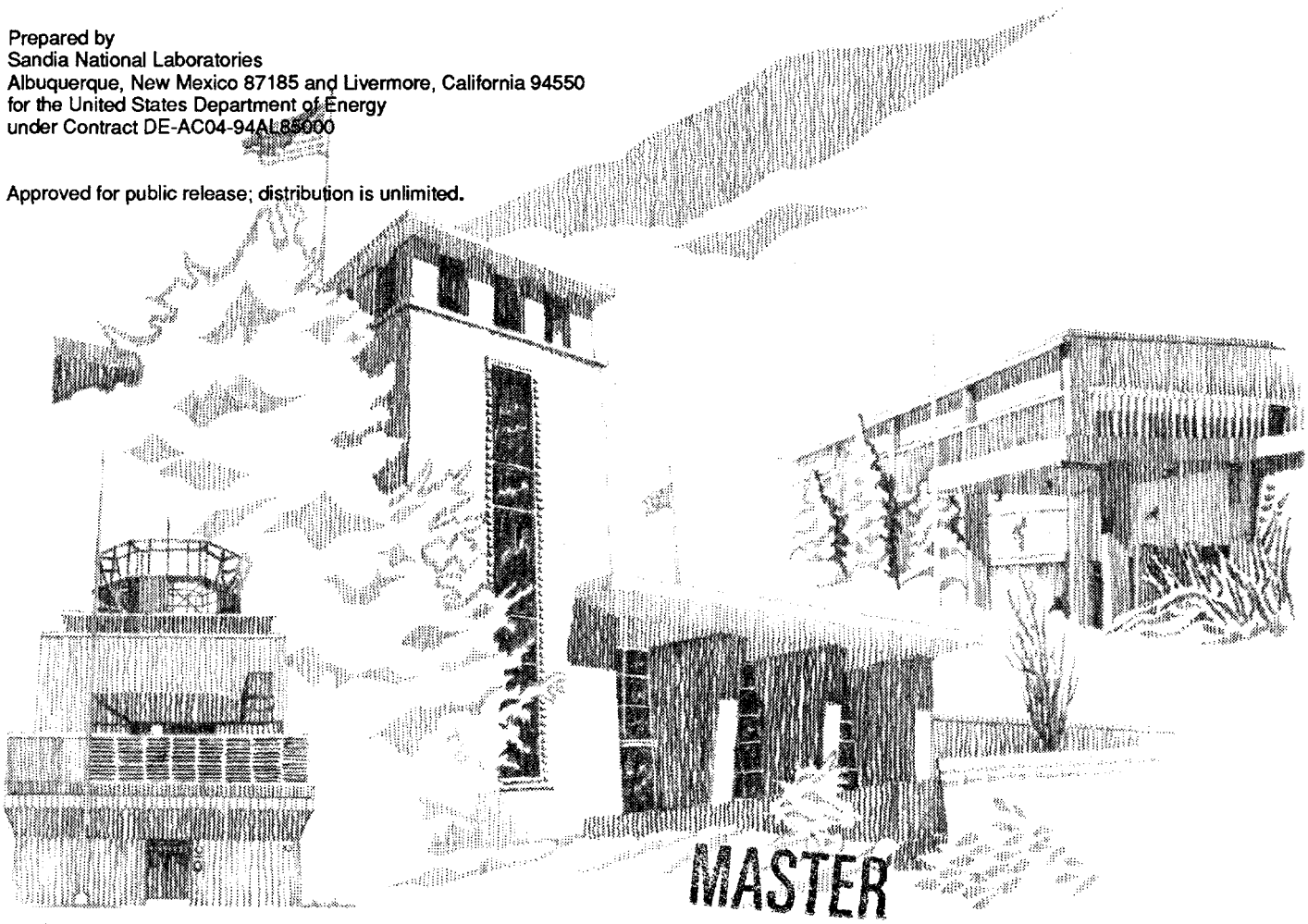

SF2900Q(8-81)

"Prepared by Yucca Mountain Site Characterization Project (YMSCP) participants as part of the Civilian Radioactive Waste Management Program (CRWM). The YMSCP is managed by the Yucca Mountain Project Office of the U.S. Department of Energy, DOE Field Office, Nevada (DOE/NV). YMSCP work is sponsored by the Office of Geologic Repositories (OGR) of the DOE Office of Civilian Radioactive Waste Management (OCRWM)."

Issued by Sandia National Laboratories, operated for the United States Department of Energy by Sandia Corporation.

Available to DOE and DOE contractors from
Office of Scientific and Technical Information
PO Box 62
Oak Ridge, TN 37831

Prices available from (615) 576-8401, FTS 626-8401

Available to the public from
National Technical Information Service
US Department of Commerce
5285 Port Royal Rd
Springfield, VA 22161

NTIS price codes
Printed copy: A07
Microfiche copy: A01

Distribution Category
UC-814

SAND95–1546
Unlimited Release
Printed September, 1995

Alternative Conceptual Models and Codes for Unsaturated Flow in Fractured Tuff: Preliminary Assessments for GWTT-95

Clifford K. Ho
Geohydrology Department
Sandia National Laboratories
Albuquerque, New Mexico 87185-1324

Susan J. Altman and Bill W. Arnold
YMP System Performance Assessment Department
Sandia National Laboratories
Albuquerque, New Mexico 87185-1326

Abstract

A suite of benchmark studies and analyses were performed to assess the strengths, weaknesses, and capabilities of three numerical codes (DUAL, FEHMN, and TOUGH2) for simulating flow through fractured media. Alternative conceptual models of fracture flow that included the equivalent continuum and dual permeability models were investigated in each study. Each benchmark was designed to investigate important issues such as layering, capillary barriers, heterogeneous material properties, boundary conditions, and fracture-matrix conductances that might initiate and contribute to flow in fast paths in the unsaturated zone of Yucca Mountain. Field-scale simulations and comparisons to data obtained from drillhole UZ-16 at Yucca Mountain, Nevada, were also performed to provide a "reality check" on the models, methods, and parameters that were used in this study. Results indicate that the dual permeability model provides the most reasonable behavior of flow through fractures under a variety of infiltration conditions because of its ability to simulate non-equilibrium conditions between the fractures and matrix. In addition, both the TOUGH2 and FEHMN codes appear to be viable tools for simulating the domains and conditions that will be used for groundwater travel time calculations.

PREFACE

This work was performed under the guidance of the US Department of Energy, Office of Civilian Radioactive Waste Management, Yucca Mountain Site Characterization Project, under contract #DE-AC04-94AL85000. The scientific investigation discussed in this report is covered under the description of work for WBS 1.2.5.4.4. The planning document that directed this work activity is WA-0192, Revision 00. None of the studies described in this report represent work that is defined as quality affecting.

ACKNOWLEDGMENTS

The authors gratefully acknowledge Mike Wilson, Roger Eaton, and Peter Davies for their careful and thorough review of this report. We also thank Tom Robey, George Zyvoloski, and Karsten Pruess—the authors of the numerical codes presented in this report—for their assistance and suggestions. Finally, we thank Rally Barnard, Sharon Shannon, Andy Wolfsberg, Steve Webb, Sean McKenna, and Chris Rautman for their insightful discussions during various phases of this report.

EXECUTIVE SUMMARY

Groundwater travel time (GWTT) calculations will play an important role in addressing site-suitability criteria for the potential high-level nuclear waste repository at Yucca Mountain, Nevada. In support of these calculations, preliminary assessments of the candidate codes and models are presented in this report. A series of benchmark studies have been designed to address important aspects of modeling flow through fractured media representative of flow at Yucca Mountain. Three codes (DUAL, FEHMN, and TOUGH2) are compared in these benchmark studies. DUAL is a single-phase, isothermal, two-dimensional flow simulator based on the dual mixed finite element method (Robey, 1994). FEHMN is a nonisothermal, multiphase, multidimensional simulator based primarily on the finite element method (Zyvoloski et al., 1995). TOUGH2 is a nonisothermal, multiphase, multidimensional simulator based on the integral finite difference method (Pruess, 1987; Pruess, 1991). Alternative conceptual models of fracture flow consisting of the equivalent continuum model (ECM) and the dual permeability (DK) model are used in the different codes.

In Benchmark 1 (Chapter 2), simulations of one-dimensional infiltration into a homogeneous fractured domain using DUAL, FEHMN, and TOUGH2 were performed. The purpose of this benchmark was to verify the proper implementation and function of the ECM within each code by comparing the simulated results to a semi-analytical solution. Results showed that FEHMN and TOUGH2 yielded accurate steady-state solutions using the ECM. However, DUAL could not replicate the semi-analytical saturation distribution for this one-dimensional homogeneous problem.

Benchmark 2 (Chapter 3) introduced layers of different geologic units to the one-dimensional column described in Benchmark 1. Simulations of steady infiltration into this domain were performed to compare DUAL, FEHMN, and TOUGH2 in layered media and to assess different conceptual models of fracture flow using the ECM and DK models. Results showed that FEHMN and TOUGH2 yielded very similar steady-state saturation profiles for steady infiltration rates ranging from 0.1 to 4.0 mm/year. DUAL, however, had troubles simulating infiltration rates other than 0.2 mm/year. At this infiltration rate, the resulting saturation profiles from DUAL were lower

than the predicted saturations of FEHMN and TOUGH2. Comparison of the ECM and DK models of fracture flow revealed that the geometric conductance term between the fractures and matrix played an important role in simulations of the system behavior and could be made equivalent between FEHMN and TOUGH2 through the appropriate specification of a length scale in FEHMN (see Appendix B). The conductance term could be modified in the DK model to account for small scale processes such as fingering and channeling that effectively reduce the conductance between the fractures and matrix. The DK model was shown to be capable of producing significant flow through the fracture continuum, even under low infiltration rates and steady-state conditions.

Benchmark 3 (Chapter 4) included simulations of infiltration into a two-dimensional domain with dipping layers to investigate lateral diversion of flow and localized infiltration sources. Results showed that capillary diversion occurred at unit interfaces as a result of capillary pressure and conductivity differences in different materials. At low infiltration rates (≤ 0.1 mm/year), all the units remained unsaturated and a capillary diversion existed at the TCw-PTn interface. At higher infiltration rates (≥ 1.0 mm/year), the welded units became saturated and capillary diversion occurred at the PTn-TSw interface. Results also showed that lateral diversion in the PTn was very sensitive to the choice of two-phase matrix parameters that were used in the PTn unit. In particular, smaller values of the air entry parameter, α, that were used for the PTn matrix yielded greater lateral diversion through the PTn. The use of the DK model showed greater propagation of flow through the TCw unit resulting in lower matrix saturations, and, hence, greater capillary diversions above the PTn. Localized infiltration also resulted in greater capillary diversion in the TCw as a result of the lower matrix saturations in the TCw unit away from the source. In general, the localized infiltration produced a greater range of saturations throughout the entire domain when compared to a uniform infiltration. Results of steady-state saturations using the ECM were similar for TOUGH2 and FEHMN.

Benchmark 4 (Chapter 5) examined steady and transient infiltration into a completely heterogeneous, unsaturated domain using the ECM and DK models. The purpose was to determine the capabilities of different codes and models in handling flow though a domain with hundreds of different materials. Results showed that DUAL and TOUGH2[†] were capable of simulating flow in the heterogeneous domain and yielded similar distributions of saturation. The use of the DK model in TOUGH2 showed that "realistic" propagation of fracture flow could be modeled under transient infiltration boundary conditions. Flow resembling fingering and channeling in the fracture domain was observed when the TOUGH2 DK model was used to

[†] The material dimensions were increased from 27 to 2007 in TOUGH2. Currently, in FEHMN, the maximum number of parameter sets defining the two-phase curves is limited to 25, so FEHMN was not used in Benchmark 4. However, the number of different materials in FEHMN can also be increased to an arbitrary amount.

simulate high infiltration conditions in the heterogeneous domain. The ECM model, in contrast, was unable to show significant propagation of flow through the fractures under the high infiltration condition.

Finally, all of the important issues addressed in the benchmark problems—layering, capillary barriers, heterogeneous material properties, and boundary conditions—were combined and applied in the analysis of field data obtained from drillhole UZ-16 at Yucca Mountain, Nevada (Chapter 6). Starting with measured values of matrix porosities at UZ-16, all other hydrologic parameters were derived and used in TOUGH2 models (1-D and 2-D) to simulate steady-state saturation distributions. These saturations were then compared to measured saturations at UZ-16 to place a "reality check" on the methods, processes, and parameters being used. Results showed that the simulated saturations generally matched well with the measured saturations using a variety of alternative conceptual models of fracture flow at an infiltration rate of 0.1 mm/year. It was determined, however, that the regression used to correlate saturated conductivity and porosity for all the non-zeolitized units could not be used for the Calico Hills unit because of significant discrepancies that resulted between the measured and predicted saturations in the Calico Hills region. This indicated that the Calico Hills unit in the vicinity of UZ-16 was predominantly zeolitized and had to be treated separately using a different correlation between saturated conductivity and porosity to obtain good matches in that unit. Also, the measured saturations in the TCw were considerably lower than any predicted values. It was concluded that surface processes contributing to mass loss, such as evaporation, must be incorporated to better replicate the measured saturation in the TCw unit. This would subsequently require higher infiltration rates to match the measured saturations throughout the rest of the units.

Recommendations for GWTT-95 include the use of the dual permeability model, which improves our capability of modeling flow through fractures when transient or high infiltration boundary conditions are applied. Because of its present inability to implement the DK model, the DUAL code is not suitable for GWTT-95 calculations. FEHMN should be retained for further comparisons and analysis of groundwater travel time calculations, but TOUGH2 should be used as the primary code for GWTT-95 because of its maturity, reliable history, and demonstrated ability to simulate all of the benchmarks in this study. TOUGH2 is also currently being used in the LBL/USGS 3-D site-scale model of Yucca Mountain (Bodvarsson et al., 1995). Finally, laboratory and field studies should be included in future analyses to better quantify processes and parameters that affect the large-scale behavior being simulated in GWTT-95. Some of these include the geometric conductance term between the fractures and matrix, a description of the spatially and temporally varying infiltration boundary, and fracture continuum properties that are required in the currently available models.

CONTENTS

LIST OF FIGURES

LIST OF TABLES

NOMENCLATURE

$A_{f\text{-}m}$	connection area between the fracture and matrix elements (m^2)
b	fracture aperture (m)
CHnv	Calico Hills non-welded vitric unit at Yucca Mountain
CHnz	Calico Hills non-welded zeolitic unit at Yucca Mountain
D	fracture spacing (m)
d	distance used to calculate fracture-matrix pressure gradients
DK	dual permeability
ECM	equivalent continuum model
GWTT	groundwater travel time
k	permeability (m^2)
k_r	relative permeability
$m_{f->m}$	mass flow from the fracture to the matrix (kg/sec)
MINC	Multiple INteracting Continua (part of TOUGH2 code to generate dual permeability models)
P_c	capillary pressure (Pa)
P_g	gas pressure (Pa)
P_l	liquid pressure (Pa)
PPnw	Prow Pass non-welded to partially welded unit at Yucca Mountain
PTn	Paintbrush non-welded interval of the Topopah Springs unit at Yucca Mountain
q	infiltration rate (mm/year)
S	liquid saturation
S_r	residual liquid saturation
S_s	full liquid saturation
T	geometric conductance term between fracture and matrix elements
TCw	Tiva Canyon welded unit at Yucca Mountain
TSw	Topopah Springs welded unit at Yucca Mountain
α	van Genuchten air-entry fitting parameter (1/Pa)
β	van Genuchten fitting parameter
λ	two-phase fitting parameter used in TOUGH2 ($= 1 - 1/\beta$)
ρ	liquid density (kg/m^3)
μ	dynamic liquid viscosity (kg/m-sec)
σ	surface tension of water (0.073 N/m @ 20°C)

Subscripts:

f	fracture
m	matrix

Chapter

ONE

Introduction

1.1 Problem Statement

Flow through fractures is expected to strongly influence the overall hydrologic behavior in the unsaturated zone within the variably welded tuff units at the potential repository site at Yucca Mountain, Nevada. The system behavior can be influenced by several processes that are dominated by the hydraulic state of the fractures. These include capillary barrier effects resulting from dry fractures, which may act to increase saturations and flow in adjacent areas, and fast-flow paths resulting from the relatively large conductivities of wetted fractures. While the existence of fast-flow paths through the fractures can be a possible means of enhancing the transport of radionuclides from buried nuclear waste packages, predictions of flow and transport through fractured rock is extremely difficult. Models capable of rigorously simulating flow in realistic discrete fracture networks are lacking, and accurate characterization of subsurface fracture networks required for modeling efforts is rarely attainable. Nevertheless, estimations of the flow behavior through the variably welded, fractured tuff units at Yucca Mountain are required for calculations of groundwater travel time (GWTT). These calculations are necessary to address site suitability criteria for the potential repository at Yucca Mountain (Arnold et al., 1995).

This report, therefore, focuses on currently available alternative conceptual models and codes that are capable of representing flow through fractured media. Through a series of benchmark studies including comparisons to analytical solutions and field data, these models and codes are assessed to determine strengths, weaknesses, and important parameters within each model and code. The following sections provide descriptions of the codes, explanations of the alternative models of fracture flow, and an overview of the various benchmarks and analyses included in the report.

1.2 Numerical Codes

Three different numerical codes are used in the analyses of this report: DUAL, FEHMN, and TOUGH2. Both FEHMN and TOUGH2 have previously been recommended by Reeves et al. (1994) for use in YMP related calculations. Different conceptual models that are available in each model to represent flow through fractures are explored, and comparisons are made through benchmark studies. A short description of each code follows.

The DUAL flow code calculates the solution for steady-state, single-phase, unsaturated groundwater flow in a two-dimensional domain, using the equivalent continuum conceptual model (Robey, 1994; Arnold et al., 1995). The code employs the dual mixed finite-element method (Robey, 1990; Roberts and Thomas, 1990). In contrast to classical finite-element technique, the dual method enforces continuity of normal flux at adjacent element boundaries. Because pressure is a secondary variable in the dual method, it is discontinuous across element boundaries (i.e. the pressure calculated at a given node may be different for each of the elements containing that node). The dual method retains the effects of material heterogeneity in the flow simulation at relatively coarser levels of discretization because higher contrast in pressure in adjacent elements results in greater contrast in unsaturated hydraulic conductivity and greater heterogeneity in the flow field. Previous uses of the DUAL flow code include calculations for GWTT-94, where particle travel times and the effects of significant heterogeneity using the equivalent continuum model were investigated.

The FEHMN (Finite Element Heat and Mass Transfer Nuclear) numerical code (version FEHMN 95-05-01p-sun4) simulates transient, multi-phase, non-isothermal, unsaturated and saturated flow in one, two, or three dimensions using the finite element method as the primary numerical method (Zyvoloski et al., 1995(a)&(b)). FEHMN can also simultaneously simulate the transport of multiple solutes in addition to air and water, and a particle tracking model is included in the code. FEHMN supports a variety of different element shapes ranging from triangles and quadrilateral elements for one- and two-dimensional applications to tetrahedrons and parallelepipeds for three dimensions. FEHMN also employs several different conceptual models of fracture flow. The equivalent continuum, dual porosity, and dual permeability models (described in the next section) are all available within FEHMN. However, rigorous testing of these conceptual models for use in a groundwater travel time calculation has been minimal.

Finally, the TOUGH2 (Transport of Unsaturated Groundwater and Heat) numerical code (versions 3.0 and 3.1 in the SNL software quality assurance configuration management) simulates transient, multi-phase, non-isothermal, unsaturated and saturated flow in one, two, or three

dimensions using the integral finite difference numerical method (Pruess, 1987; Pruess, 1991). The fundamental formulation for the governing equations is very similar to that used in FEHMN. In the integral finite difference approach, however, no reference is made to a global coordinate system. Volume elements of arbitrary size and shape are specified by information describing the volume of each element and connection parameters to adjacent elements. Also included in the TOUGH2 code is the MINC (Multiple INteracting Continua) formulation for describing dual porosity and dual permeability systems of fracture flow (Pruess, 1983). Although the equivalent continuum model is not included in TOUGH2, it has been added to the code following the formulation described in Klavetter and Peters (1986) and Dudley et al. (1988).† TOUGH2 incorporates equation-of-state modules (used interchangeably) that govern more specific features of the system such as single-phase flow described by Richards' equation (1931), chemical species transport, and vapor pressure lowering. TOUGH2 has probably received the most widespread use and testing of the three codes.

1.3 Alternative Conceptual Models of Fracture Flow

The inability to accurately characterize fracture networks in situ and the lack of rigorous discrete fracture flow models has prompted the need for alternative conceptual models of fracture flow. Two of these models that are studied in this report include the equivalent continuum model (ECM) and the dual permeability (DK) model. Figure 1.1 shows a sketch of the representative domains of each model, along with a more rigorous discrete fracture model for comparison.

The equivalent continuum model has been described in detail by Klavetter and Peters (1986) and Dudley et al. (1988). This model has been used extensively in describing flow through fractured rock as a result of its relative simplicity and ease of computational implementation (Arnold et al., 1995; Robey, 1994; Dudley et al., 1988). In this model, the pressures in the matrix and fractures are assumed equal. As a result, the flow through this fracture-matrix system is equivalent to flow through a composite porous medium, which has hydraulic properties comprised of both fractures and matrix properties. Dudley et al. express that for conditions similar to those found at Yucca Mountain (i.e. low infiltration rates and good coupling between the fracture and matrix), the equivalent continuum model provides a reasonable approximation to fracture-matrix flow. However, recent studies have shown that flow processes such as fingering in fractures (Glass and Tidwell, 1991) and mechanical aspects such as fracture coatings may effectively reduce

† Several of the benchmarks in this report verify the appropriate implementation of the equivalent continuum formulation in TOUGH2.

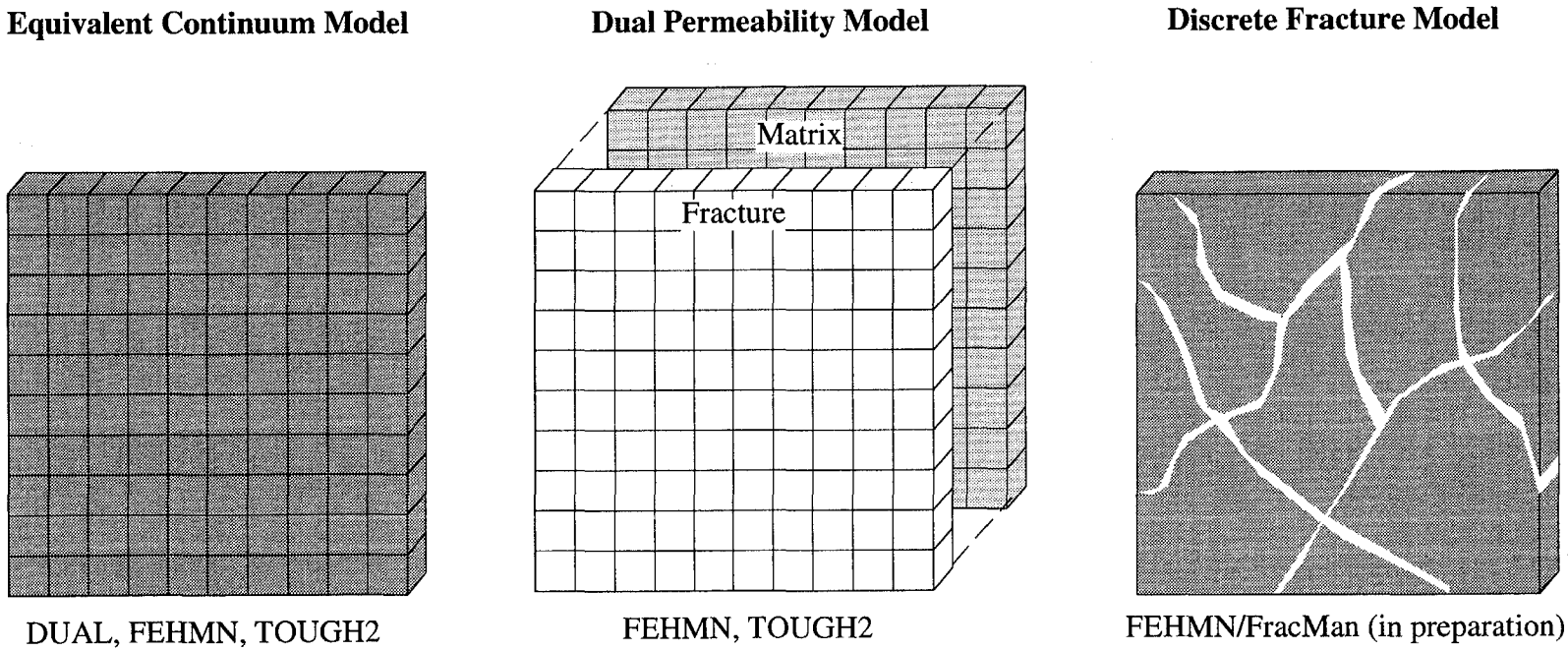

Figure 1.1. Sketch of alternative conceptual models of fracture flow. The numerical codes that implement the models in this study are listed below each figure.

the coupling between the fractures and matrix. This may cause pressure disequilibrium between the fractures and matrix, even under low infiltration rates.

If pressure equilibrium cannot be assumed, other models such as the DK model must be used. Details of the DK model can be found in Pruess and Narasimhan (1985) and Pruess (1983). Unlike the ECM, the DK model represents the fractures and matrix as separate continua. As a result, different pressures can exist in the fractures and matrix, which allows flow to occur between the two continua. Propagation of flow in fractures is more likely to be observed in these models, depending on parameters such as fracture-matrix conductance and capillary pressure gradients between the fractures and matrix. However, relatively few analyses have been performed with the dual permeability model in conjunction with analyzing fast flow paths for the assessment of a potential nuclear waste repository (Narasimhan and Wang, 1992).

1.4 Overview of Report

The alternative conceptual models and codes described above are assessed through a series of benchmarks and studies that investigate various aspects of flow through fractured rock. In the first benchmark, steady infiltration into a one-dimensional, homogeneous, vertical domain is simulated to compare the equivalent continuum results of each code to a semi-analytical solution. The second benchmark investigates infiltration into a layered, one-dimensional domain using the ECM and DK models of fracture flow. Identification of important parameters affecting the hydrologic behavior of the system are presented and discussed for each model. In the third benchmark, infiltration into a layered, dipping, two-dimensional domain is considered. The effects of lateral diversion due to capillary barriers and localized infiltration are examined using the ECM and DK models of fracture flow. A fourth benchmark introduces a completely heterogeneous domain in which each element within the domain has its own unique set of properties and parameters. Both steady and transient infiltration processes are investigated to compare the ECM and DK models in this heterogeneous environment. Finally, simulations of steady-state infiltration at Yucca Mountain are performed using data available from drillhole UZ-16. Comparison between simulated and measured saturation profiles are made to provide a "reality check" on the methods and models being used in this study.

Chapter

TWO

Benchmark 1: Homogeneous 1-D Infiltration

Simulations of steady-state, isothermal, one-dimensional infiltration into a homogeneous fractured domain using DUAL, FEHMN, and TOUGH2 are presented in this chapter. The equivalent continuum model (ECM) is used in the numerical codes to describe flow in the fractured domain. The motivation behind this exercise is to verify the proper implementation and function of the ECM within each code by comparing the simulated results to a semi-analytical solution. In addition, other issues such as harmonic vs. upstream weighting and single-phase vs. multi-phase simulations will be addressed.

A description of the problem domain and the model parameters for Benchmark 1 is presented first. Then, results of the numerical simulations are given along with a discussion of the comparisons to the semi-analytical solution (Appendix A). Following the discussion, sensitivity analyses are provided to investigate the importance of code-specific parameters and options and their implication on relevant hydrologic processes. Finally, important findings are summarized at the end of this chapter.

2.1 Description of Benchmark 1

The one-dimensional domain that is used for Benchmark 1 extends vertically 530 meters and is modeled with 106 elements (each 10 meters wide x 5 meters high (x 1 meter thick in TOUGH2)) as shown in Figure 2.1. In DUAL and FEHMN, quadrilateral elements are used resulting in a total of 214 nodes. The boundaries of this domain include a water table at the bottom and a constant infiltration rate of 0.1 mm/year (3.2×10^{-8} kg/sec) at the top. Although this domain is hypothetical, it represents the TSw2 (Topopah Spring welded) unit at Yucca Mountain. The material properties of both the fractures and matrix are taken from Klavetter and Peters (1986) and are shown in Table

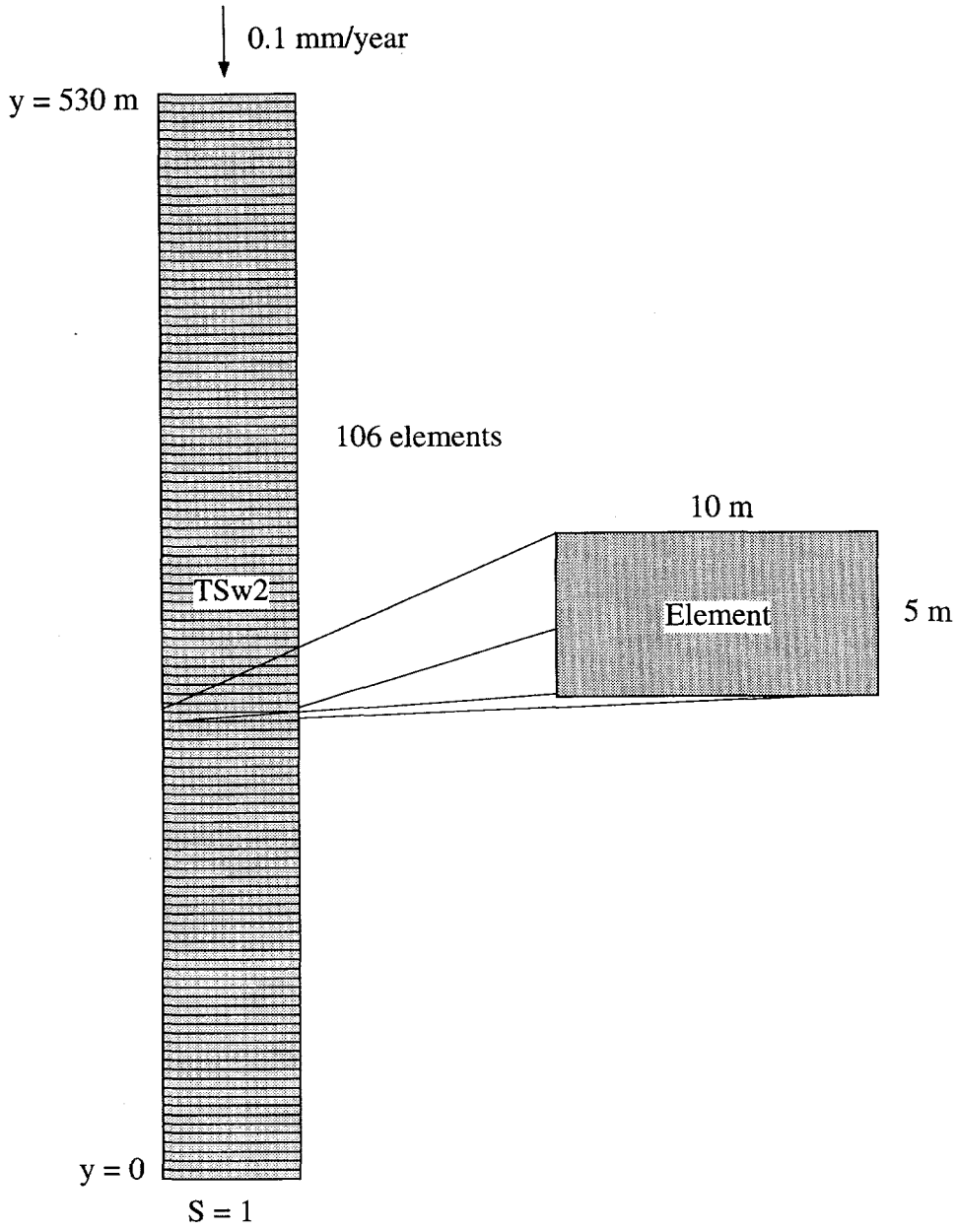

Figure 2.1. Model of the homogeneous domain used in the one-dimensional simulations of Benchmark 1.

2.1. The van Genuchten parameters (van Genuchten, 1980) are used to generate the two-phase characteristic curves for this problem. All three numerical codes that were introduced in Chapter 1 are compared to each other and to a semi-analytical solution (see Appendix A for a derivation) in this benchmark using the ECM.

Table 2.1. TSw2 properties used in Benchmark 1 (Klavetter and Peters, 1986)

	Matrix	Fracture	Composite
porosity	0.11	1.8e-4	0.11
permeability (m^2)	1.9e-18	1.7e-12	3.1e-16
residual saturation	0.08	0.0395	—
α (1/Pa)	5.78e-7	1.31e-4	—
β	1.798	4.23	—

2.2 Results and Discussion of Code Comparisons

The steady-state saturations resulting from Benchmark 1 are shown in Figure 2.2 for the semi-analytical solution and the numerical simulations using DUAL, FEHMN, and TOUGH2. At 0.1 mm/year, the semi-analytical solution predicts saturations near 0.87 at elevations greater than 350 m above the water table in the unsaturated domain. Near the water table at the bottom boundary, the solution shows the saturation rising to one. Both FEHMN† and TOUGH2 yield saturations very similar to the semi-analytical solution throughout the entire domain. Exact matches are not expected since the semi-analytical solution assumes a constant gas pressure (single-phase Richards equation), whereas the numerical simulations resulting from FEHMN and TOUGH2 do not. Section 2.3.2 presents a sensitivity analysis on the use of single- and multi-phase models of this problem.

The results of DUAL show significant deviations from the other predicted steady-state saturation profiles (Figure 2.2). DUAL predicts much lower saturations throughout most of the unsaturated domain. Attempts to address the discrepancies in the saturations using the code DUAL have been unresolved for this particular problem. Ironically, DUAL appears to give more accurate results for completely heterogeneous, two-dimensional systems (see Benchmark 4). One possible source of the discrepancy is the inter-element averaging method used in the DUAL code. In the

† Note that a recent version of FEHMN (FEHMN 95-05-01p-sun4) has been used in Figure 2.2. In previous versions of FEHMN, a parameter called SUPM (specified in the source files) had a significant effect on the results of this problem. Section 2.3 examines the sensitivity of the FEHMN results to this parameter.

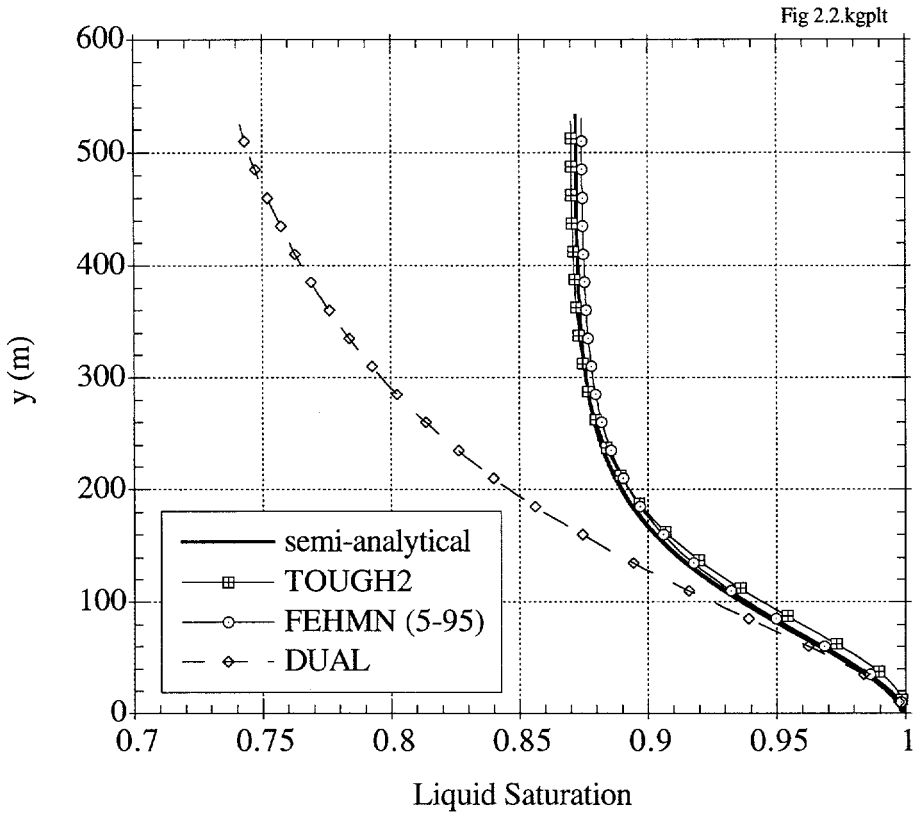

Figure 2.2. Steady-state liquid saturations in a 1-D homogeneous column with a steady infiltration of 0.1 mm/year. Predictions are shown from DUAL, FEHMN, and TOUGH2 along with the semi-analytical solution.

present version of DUAL, relative permeability is calculated using harmonic averaging, whereas an upstream weighting technique is used in the TOUGH2 simulation for this problem.

2.3 Sensitivity Analyses

2.3.1 Sensitivity Analysis of FEHMN

The results of older versions (prior to 5/95) of the FEHMN code for unsaturated problems have been shown to be sensitive to a code-specific parameter called SUPM. This parameter represents an upper cut-off saturation which is used in the calculation of the two-phase characteristic curves. The most current version of FEHMN has eliminated the need to specify this parameter within a source file of the code. However, users should be aware that versions of FEHMN released prior to 5/95 may contain the SUPM parameter in the 'rlperm.f' source file. This section presents a sensitivity analysis of the results of FEHMN using different values of SUPM. All of the parameters and boundary conditions remain the same as in the original Benchmark 1 problem; only the value of SUPM is varied in the code. Figure 2.3 shows the resulting steady-state saturations for different values of SUPM. The semi-analytical solution is also plotted in Figure 2.3 for comparison.

Figure 2.3 shows that for lower values of SUPM, the predicted saturations deviate further from the semi-analytical solution. Since SUPM represents an upper cut-off saturation for the calculation of the capillary pressure curve, lower values of SUPM result in less accurate capillary pressures at high saturations. Hence, larger values of SUPM (≥ 0.99) are required to produce accurate saturation distributions near the water table at the bottom boundary as shown in Figure 2.3. However, a trade-off occurs in the simulation time at these higher SUPM values. In general, simulations with a higher SUPM value require longer simulation times—most likely to resolve the steep gradient in the capillary pressure curve at high saturations. The new version of FEHMN appears to have circumvented this tradeoff without specifying a SUPM parameter, providing accurate solutions and faster simulation times than those obtained with older versions using values of SUPM ≥ 0.99.

2.3.2 Single-Phase vs. Two-Phase Simulations

Both FEHMN and TOUGH2 are multi-phase simulators—they simulate the transport of both liquid- and gas-phase components in porous materials. Both codes are also capable of eliminating the gas-phase balance law from the numerical solution. In FEHMN, this is achieved by specifying

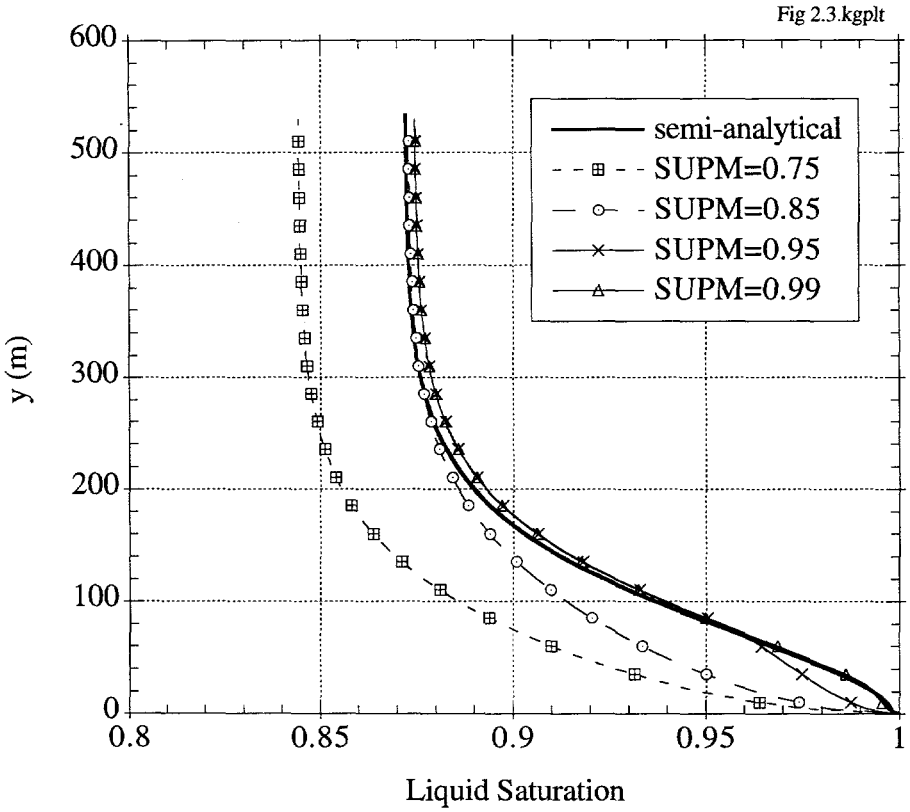

Figure 2.3. FEHMN steady-state liquid saturations in a 1-D homogeneous column with a steady infiltration of 0.1 mm/year. Predictions are shown for different values of the SUPM parameter found in older versions of FEHMN (prior to 5/95).

appropriate parameters in the AIRWATER macro. In TOUGH2, the single-phase equation-of-state module EOS9 must be used (version 3.1 in SNL's configuration management system). These modifications result in the solution of a single-phase system described by Richards' equation (1931). In this system, the transport of gas is neglected and the gas pressure is assumed constant everywhere. For many problems such as infiltration into a region where the gas-phase is able to redistribute freely, this approximation often provides accurate results. This assertion is tested in this section by using the single-phase modifications to FEHMN and TOUGH2.

Figure 2.4 shows the steady-state saturations for Benchmark 1 using single-phase models in FEHMN and TOUGH2. For comparison, the two-phase and semi-analytical solutions are also plotted. The single-phase solutions produce nearly identical results to the two-phase solutions, except for simulations using TOUGH2 where the single-phase solutions show slightly lower saturations near the water table. These lower saturations resulting from the single-phase simulations are actually closer to the semi-analytical solution. This is not surprising, however, since the semi-analytical solution is based on a single-phase system and does not include pressure variations resulting from the gas-phase.

2.3.3 Upstream vs. Harmonic Weighting of the Mobility Terms

In this section, two different weighting schemes are implemented for the product of the permeability and relative permeability calculated at the interface of two adjacent elements in TOUGH2. Harmonic weighting yields more accurate solutions in particular cases, but previous studies have shown that upstream weighting is necessary to avoid gross errors for transient problems in layered media (Tsang and Pruess, 1990). In this steady-state, homogeneous problem, the use of harmonic weighting is not expected to cause problems. However, a comparison between harmonic weighting and upstream weighting is desired to compare the accuracy of the resulting solutions for this simple problem.

Figure 2.5 shows the results of TOUGH2 simulations using harmonic and upstream weighting for the product of the absolute and relative permeabilities at each element interface. Results are shown for both the single- and two-phase models. In each model, the different weighting schemes provide nearly identical results. As a result of this simple comparison and recommendations made by Pruess (1991), upstream weighting is implemented for the remaining problems in this report.

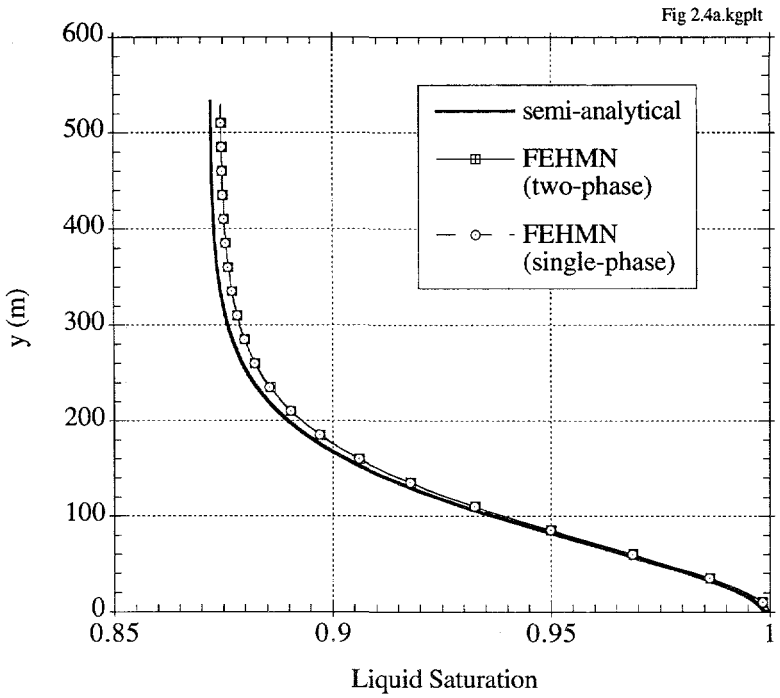

(a)

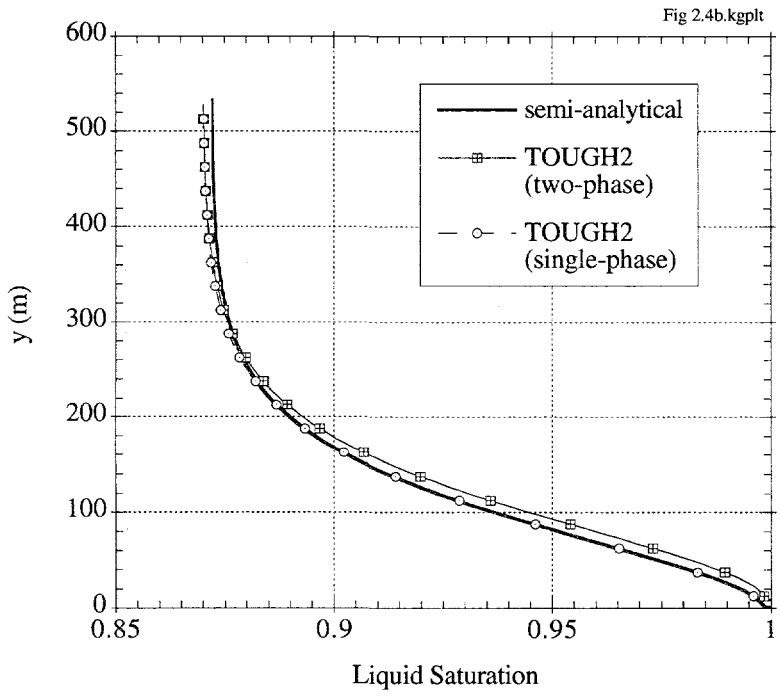

(b)

Figure 2.4. Steady-state liquid saturations in a 1-D homogeneous column with a steady infiltration of 0.1 mm/year using the single- and two-phase versions of a) FEHMN and b) TOUGH2.

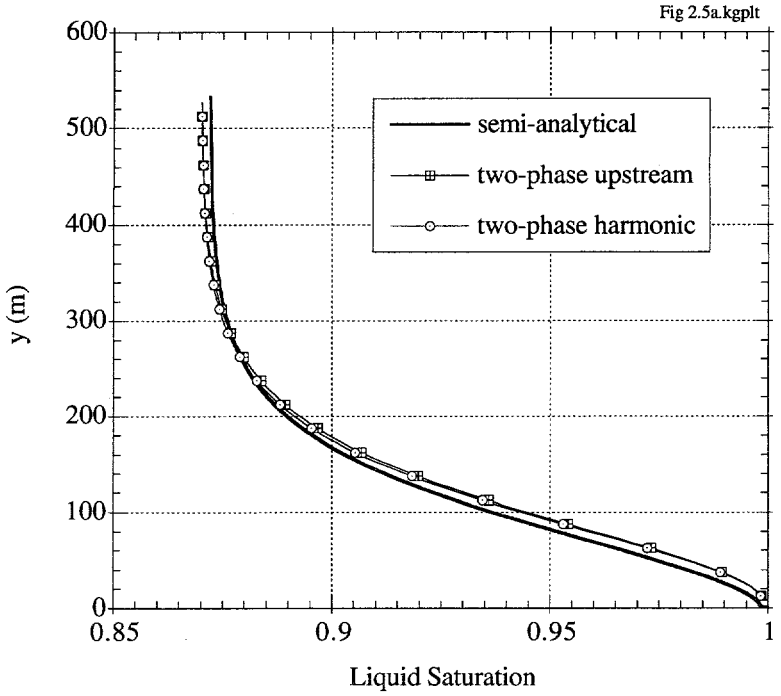

(a)

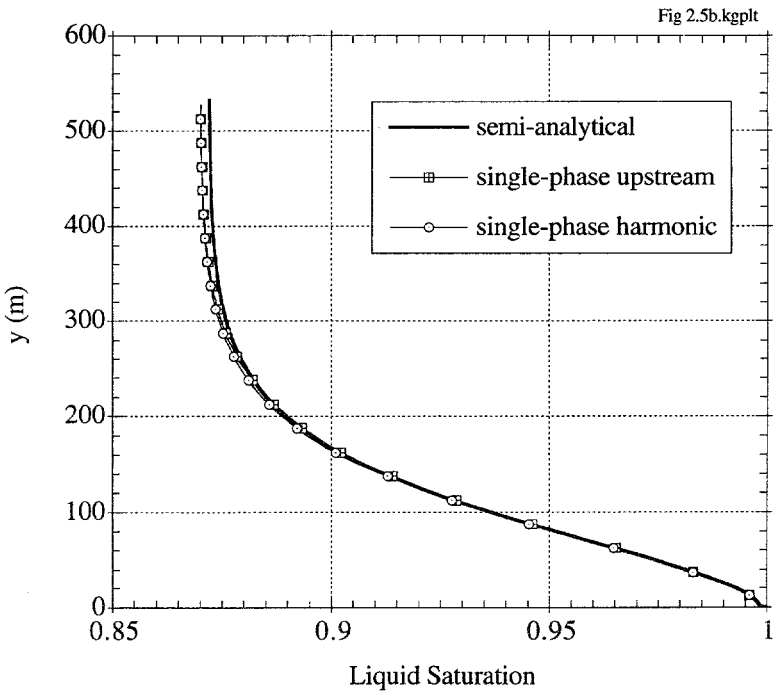

(b)

Figure 2.5. TOUGH2 steady-state liquid saturations in a 1-D homogeneous column with a steady infiltration of 0.1 mm/year. Upstream and harmonic weighting schemes are used on $k \cdot k_r$ for a) two-phase and b) single-phase versions of TOUGH2.

2.4 Summary

Infiltration into a one-dimensional vertical domain consisting of homogeneous fractures and matrix has been modeled to compare several numerical codes. The implementation and function of the ECM in the numerical codes DUAL, FEHMN, and TOUGH2 have been tested using this problem. Results show that both FEHMN and TOUGH2 yield accurate steady-state solutions using the ECM. DUAL could not replicate the semi-analytical saturation distribution for this one-dimensional homogeneous problem, but other analyses indicate that DUAL works reasonably well for heterogeneous, two-dimensional systems (Arnold et al., 1995; Benchmark 4 (this report)).

Sensitivity analyses for Benchmark 1 reveal that older versions of FEHMN may require modification of the parameter SUPM found in one of the FEHMN source files. This parameter defines a cut-off saturation which is used in the calculation of the capillary pressure. Lower values of SUPM result in less accurate results near regions of high saturation. The most recent version (5/95) of FEHMN has circumvented this problem.

Single-phase models using Richards equation included in FEHMN and TOUGH2 were also compared to the two-phase models in this problem. Results showed that the saturations through most of the unsaturated region were nearly identical for the single- and two-phase models. Near the water table, the single-phase model produced slightly lower saturations than the two-phase model in TOUGH2. Saturations resulting from FEHMN using both models remained nearly identical. In terms of computational efficiency, the single-phase model in TOUGH2 yielded simulation times that were much faster than the two-phase model. In FEHMN, the single- and two-phase simulations produced similar simulation times. Details of the computational efficiency of the two models are examined more closely in the next chapter. Finally, upstream weighting of permeability and relative permeability was found to yield similar results to harmonic weighting for the Benchmark 1 problem using TOUGH2.

Chapter

THREE

Benchmark 2: Layered 1-D Infiltration

In this chapter, layers of different geologic units are added to the one-dimensional vertical domain described in Benchmark 1. Simulations of one-dimensional infiltration into the layered domain are performed using DUAL, FEHMN, and TOUGH2. The objectives here are again to compare the different codes to ensure that they are performing properly for the purposes of calculating a groundwater travel time. Comparisons are made to previous code comparisons performed by Dykhuizen and Barnard (1992) to verify the results of the codes. Additional studies are also performed to assess different conceptualizations of fracture flow using the equivalent continuum model (ECM) and dual permeability (DK) models.

This chapter first provides a description of the problem used in the layered one-dimensional infiltration problem. Results of the code comparisons for this problem are then presented and discussed. Additional studies are then presented regarding the use of the ECM and DK models. Finally, single-phase vs. two-phase modeling results for Benchmark 2 are discussed.

3.1 Description of Benchmark 2

The one dimensional domain that is used for Benchmark 2 is nearly identical to the one used in Benchmark 1. The only difference is that the domain has been divided into five different geologic layers that are representative of the variably welded tuff units at Yucca Mountain. The modeled domain is the same as the one used by Dykhuizen and Barnard (1992) and is shown in Figure 3.1. The domain extends vertically 530 meters and is modeled with 106 elements (each 10 meters wide x 5 meters high (x 1 meter thick in TOUGH2)). In DUAL and FEHMN, quadrilateral elements are used resulting in a total of 214 nodes. The boundaries of this domain include a water table at the bottom and a constant infiltration rate at the top. Different infiltration rates of 0.1 mm/year (3.2e-8 kg/sec), 0.2 mm/year (6.3e-8 kg/sec), and 4.0 mm/year (1.3e-6 kg/sec) are used

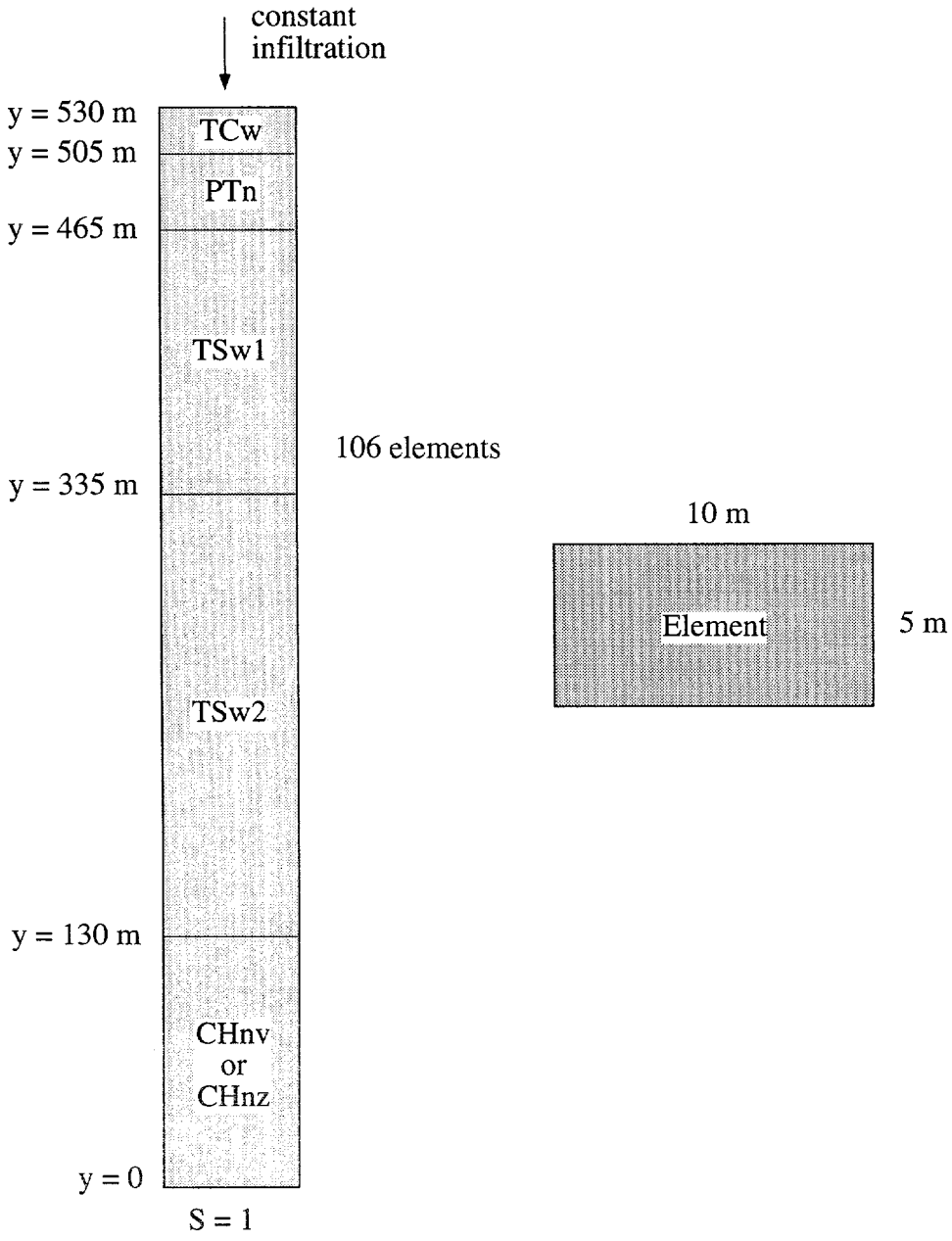

Figure 3.1. Model of the layered domain used in the one-dimensional simulations of Benchmark 2.

in this benchmark. The material properties of both the fractures and matrix in each of the geologic units are taken from Klavetter and Peters (1986) and are shown in Table 3.1. The van Genuchten (1980) parameters are used to generate the two-phase characteristic curves for this problem. Note that these parameters are used only for the *code* comparisons in section 3.2 to be consistent with Dykhuizen and Barnard (1992). For comparisons of the alternative conceptual models of fracture flow in section 3.3, more recent parameters are used and are presented in that section.

3.2 Results and Discussion of Code Comparison

In this section, comparisons of DUAL, FEHMN, and TOUGH2 are made using the ECM model of the problem shown in Figure 3.1. Several different infiltration rates ranging from 0.1 mm/year to 4.0 mm/year are used in this problem. It should be noted that while FEHMN and TOUGH2 were able to simulate the entire range of infiltrations, DUAL could only successfully simulate an infiltration rate of 0.2 mm/year.

Figure 3.2 shows the steady-state saturations for all three codes using an infiltration rate of 0.2 mm/year (6.3e-8 kg/sec). The results of FEHMN and TOUGH2 are very similar, whereas the saturations resulting from DUAL are slightly lower (~5%) throughout much of the domain. This discrepancy is consistent with the results of Benchmark 1, which showed that the saturations resulting from DUAL were lower than the saturations resulting from the other two codes. In general, Figure 3.2 shows that the saturations are higher in the welded units (TCw, TSw1, and TSw2) and in the zeolitized Calico Hills unit. Although the Calico Hills unit is non-welded, the permeability and air-entry parameter, α (inverse of the air-entry pressure), are considerably less than other non-welded units (presumably due to the zeolites). As a result, higher saturations occur in that unit. The anomalous behavior of the zeolitized Calico Hills unit is investigated further in Chapter 6.

Figure 3.3 shows a comparison of the steady-state saturations resulting from FEHMN and TOUGH2 for an infiltration rate of 0.1 mm/year. The results from Dykhuizen and Barnard (1992) are also presented in that figure as a thick solid line (labeled COVE-2A). In that study, five different codes (TOSPAC, TRACR3D, TRUST, LLUVIA, and NORIA) using the single-phase (Richards equation) formulation were compared. The results of all five essentially fall on the same line as shown in Figure 3.3. The results of FEHMN and TOUGH2 compare very well with those results through the entire domain. TOUGH2 appears to have slightly higher saturations near the bottom of the TSw2 unit. This slight discrepancy may be a result of the two-phase model that was used in TOUGH2 for this comparison. Recall that the single-phase version of TOUGH2 resulted

Table 3.1. Material properties used in Benchmark 2 (Klavetter and Peters, 1986)

	TCw	PTn	TSw1	TSw2	CHnz
Matrix					
porosity	0.08	0.40	0.11	0.11	0.28
permeability (m^2)	9.7e-19	3.9e-14	1.9e-18	1.9e-18	2.0e-18
α (1/Pa)	8.37e-7	1.53e-6	5.78e-7	5.78e-7	3.14e-7
β	1.558	6.872	1.798	1.798	1.602
S_r	0.002	0.10	0.08	0.08	0.11
S_s†	1.0	1.0	1.0	1.0	1.0
Fracture					
porosity	1.4e-4	2.7e-5	4.1e-5	1.8e-4	4.6e-5
intrinsic permeability (m^2)	3.8e-12	6.1e-11	2.2e-12	1.7e-12	2.0e-11
continuum permeability (m^2)††	5.3e-16	1.6e-15	0.9e-16	3.1e-16	9.2e-16
α (1/Pa)	1.31e-4	1.31e-4	1.31e-4	1.31e-4	1.31e-4
β	4.23	4.23	4.23	4.23	4.23
S_r	0.0395	0.0395	0.0395	0.0395	0.0395
S_s†	1.0	1.0	1.0	1.0	1.0
Composite					
porosity	0.08	0.40	0.11	0.11	0.28
permeability (m^2)	5.3e-16	4.1e-14	9.2e-17	3.1e-16	9.2e-16

†The full saturations, S_s, of both the matrix and fractures are assumed to equal 1.0.

††The continuum permeability is equal to the intrinsic permeability multiplied by the fracture porosity.

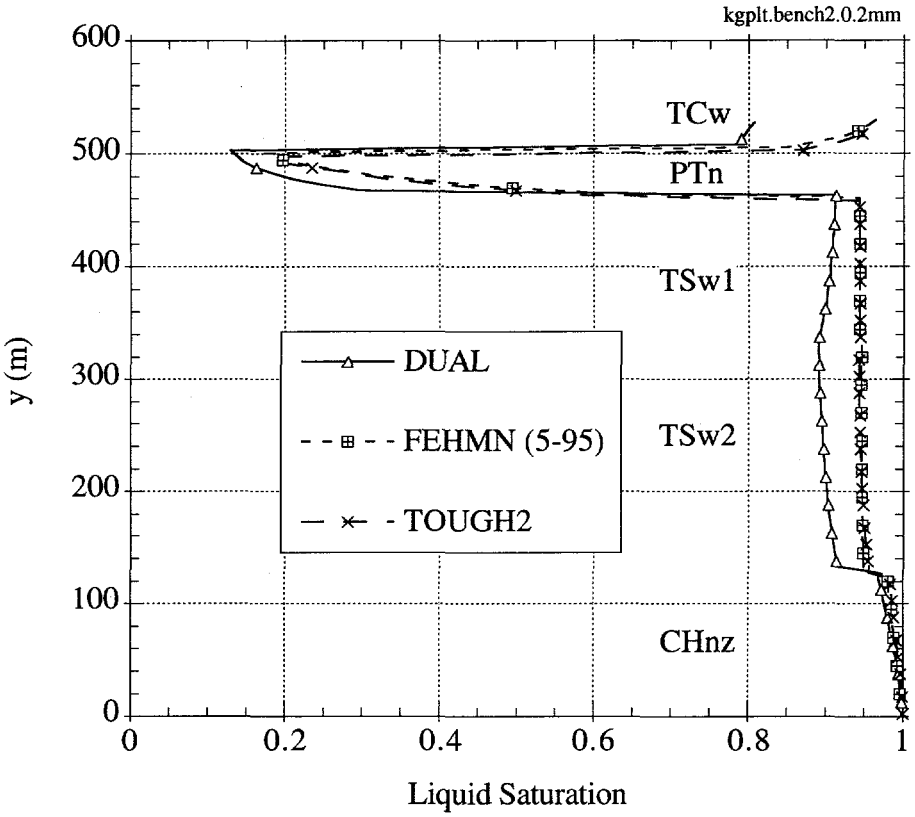

Figure 3.2. Steady-state ECM matrix saturations predicted by DUAL, FEHMN, and TOUGH2 in a 1-D layered column with a steady infiltration of 0.2 mm/year and a saturated bottom boundary.

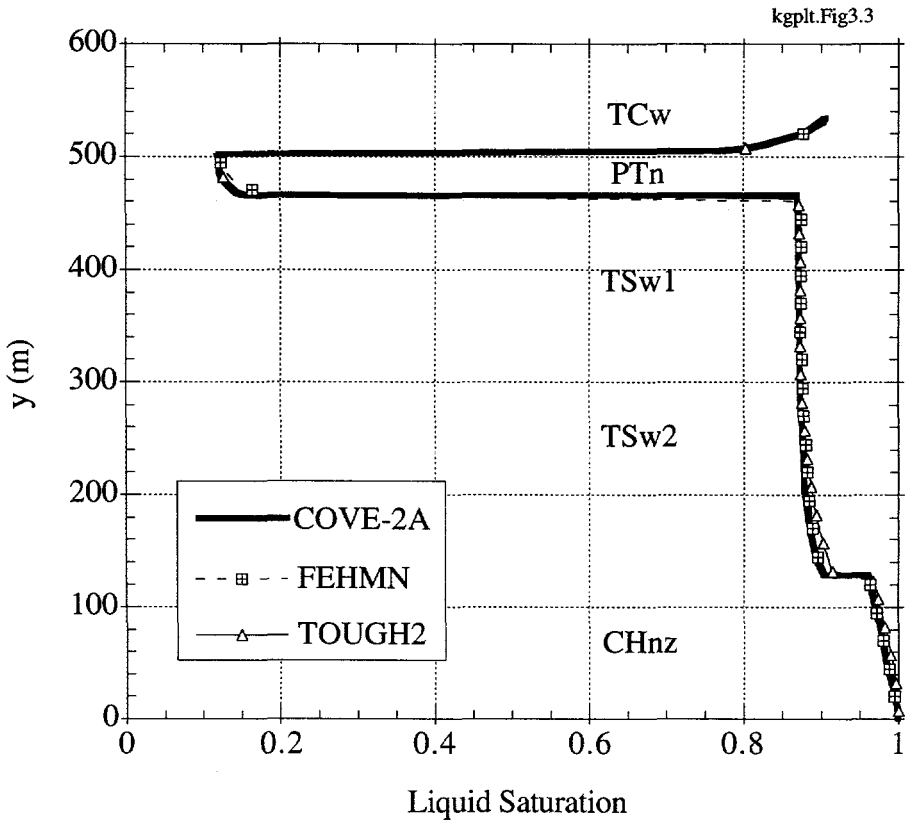

Figure 3.3. Steady-state ECM matrix saturations for Benchmark 2 comparing results from FEHMN and TOUGH2 to COVE-2A (Dykhuizen and Barnard, 1992). The upper boundary has an infiltration rate of 0.1 mm/year, and the bottom boundary is saturated.

in slightly lower saturations near the bottom of the domain in Benchmark 1 (Figure 2.4b). Although the two-phase model in FEHMN is also used here, the differences between the single- and two-phase results are considerably less as evidenced by the results in Benchmark 1 (Figure 2.4a).

3.3 ECM vs. DK Models for Benchmark 2

In this section, the codes FEHMN and TOUGH2 are used to assess alternative conceptual models of fracture flow. Chapter one introduced the two types of models that are investigated here—the equivalent continuum model (ECM) and the dual permeability (DK) model. Saturations and velocities resulting from the two models are compared, and parameters such as the infiltration rate and the conductance between the fractures and matrix are varied to determine the importance of specific variables.

The same one-dimensional problem shown in Figure 3.1 is used to compare the two models with slight modifications. The Calico Hills unit is assumed to be vitric instead of zeolitic, and the TSw1 and TSw2 units are combined into a single unit. Also, the material parameters for this analysis are taken from TSPA-93 (Wilson et al., 1994) and are listed in Table 3.2. The properties in Table 3.2 are the expected values from entropy fits used to match the sampled data in TSPA-93. Geometric means (from the $\log_{10}$ expected values) are used for all the parameters except for the fracture intrinsic permeability, which uses an arithmetic mean of the sampled data (the arithmetic mean produced a larger, and hence more conservative, fracture permeability than the geometric mean). The single-phase (Richards equation) models in FEHMN and TOUGH2 are used for this analysis. It should also be noted that the initial saturation is set to 0.85.†

3.3.1 Dual Permeability Formulation in TOUGH2 and FEHMN

The formulation for the DK used in TOUGH2 is taken from Pruess (1983) and Pruess and Narasimhan (1985). A table of parameters for the dual permeability formulation in TOUGH2 is given in Table 3.3. Of particular interest in this table are the calculations for the connection area and distance between the fractures and matrix. The connection area is derived from geometry based on fracture spacing, aperture, and volume of the grid block (or computational cell). The

† The initial saturation should not affect the results since steady-state solutions are obtained. However, smaller values of the initial saturation (~0.3) resulted in much smaller time steps and longer simulation times. In fact, in some of the DK simulations, steady-state solutions could not be achieved in a reasonable time frame unless the initial saturation was increased to 0.85.

Table 3.2. TSPA93 (Wilson et al., 1994) parameters used in the ECM vs. DK comparisons for Benchmark 2.

	TCw	PTn†	TSw1-2	CHnv	CHnz$^{\Omega}$
Matrix					
porosity	0.087	0.421	0.139	0.331	0.306
permeability (m^2)	2.04e-18	2.51e-14	2.09e-18	1.10e-16	1.59e-18
α (1/Pa)	7.91e-7	3.78e-5	1.36e-6	2.79e-6	5.94e-7
$\lambda=1-1/\beta$	0.383	0.578	0.444	0.594	0.414
S_r	0.0212	0.154	0.0453	0.0968	0.121
S_s	1.0	1.0	1.0	1.0	1.0
Fracture					
porosity††	2.93e-4	9.27e-5	2.43e-4	1.11e-4	5.25e-5
intrinsic perm. (m^2)	4.06e-9	7.14e-9	4.57e-9	6.53e-9	1.91e-0
fracture spacing (m)	0.618	2.22	0.74	1.62	2.06
fracture aperture (m)	1.81e-4	2.06e-4	1.80e-4	1.79e-4	1.08e-4
scaled perm. (m^2)	1.19e-12	6.62e-13	1.11e-12	7.23e-13	1.00e-13
α (1/Pa)	1.23e-3	1.4e-3	1.22e-3	1.22e-3	7.30e-4
$\lambda=1-1/\beta$	0.667	0.667	0.667	0.667	0.667
S_r†††	0.0 or 0.03	0.0 or 0.03	0.0 or 0.03	0.0 or 0.03	0.03
S_s	1.0	1.0	1.0	1.0	1.0
Composite					
porosity	0.0873	0.421	0.139	0.331	0.306
permeability (m^2)	1.19e-12	6.87e-13	1.11e-12	7.23e-13	1.00e-13

†The matrix permeability and α of the PTn are bi-modal, so the area weighted average is used for those parameters.

††The fracture porosity is calculated as the fracture aperture divided by the fracture spacing.

†††A residual fracture saturation of 0.03 is used in the 0.1 mm/year infiltration cases, while 0.0 is used in the 4.0 mm/year cases. The TOUGH2 DK model could not reach steady-state within 4000 time steps using S_r=0 at 0.1 mm/year, so S_r=0.03 was used.

$^{\Omega}$The CHnz parameters are used in the UZ-16 analysis in Chapter 6.

distances between the fractures and matrix are derived to yield the best estimate for a quasi-steady flux between the fractures and matrix (Pruess, 1983).

The DK formulation for FEHMN is provided in Zyvoloski et al. (1995b). In this model, the conductance between the fractures and matrix is defined by a geometric transfer term that can be interpreted as the area between the fractures and matrix divided by the distance between the fractures and matrix. These parameters are defined in terms of the fracture porosity and a length scale. To compare dual permeability simulations between FEHMN and TOUGH2, the length scale should be defined so that the conductance terms between the fractures and matrix are equivalent in FEHMN and TOUGH2. The details of this calculation are given in Appendix B and can be summarized as follows: the length scale (APUV1) in FEHMN should be set equal to the fracture spacing divided by $\sqrt{12}$ to yield a conductance between the fractures and matrix that is equivalent to the conductance used in TOUGH2 for a dual permeability system (see Table 3.3).

Table 3.4 provides some code-specific parameters that are used in FEHMN. RP5 is defined as a "multiple of cutoff capillary pressure assigned as the maximum capillary pressure." where $RP5 \cdot P_{cap}(S_{cutoff})$ is forced at S=0 for the matrix (Zyvoloski et al., 1995). RP6 is defined as the cutoff saturation (S_{cutoff}) for the matrix. Both RP5 and RP6 are used to fit the lower end of the moisture retention curve. RP11 and RP12 are equivalent to RP5 and RP6, but they are used for the fracture instead of the matrix. APUV1 is a length scale that is discussed in Appendix B. It is set equal to the fracture spacing divided by $\sqrt{12}$.

3.3.2 Saturation Comparisons

Steady-state saturations resulting from FEHMN and TOUGH2 using the ECM and DK models are shown in Figures 3.4–3.6 for infiltration rates of 0.1 and 4.0 mm/year. It should be noted that for the DK simulations, the top infiltration boundary was applied to the fracture domain of the TCw unit. An additional simulation is also shown in those plots for each code in which the fracture-matrix geometric conductance terms (shown in Table 3.3) are reduced by two orders of magnitude in the DK simulations for each unit. The reduction in the conductance between the fractures and matrix can be used to account for small-scale processes such as fingering and channeling that may reduce the wetted area of the fractures. Appendix B contains a more complete description of this assertion.

In Figure 3.4, both FEHMN and TOUGH2 show similar results in the steady-state matrix saturations for the ECM and DK model at an infiltration rate of 0.1 mm/year. At an infiltration rate of 0.1 mm/year, the matrix elements are capable of conducting the entire flow. As a result, the

Table 3.3. Parameters for a 1-D dual permeability TOUGH2 model with two interacting continua (1 fracture and 1 matrix continuum)†.

	TCw	PTn	TSw1-2	CHnv
Aperture, b (m)	1.81e-4	2.06e-4	1.80e-4	1.79e-4
Fracture spacing, D (m)	0.62	2.2	0.74	1.6
Volume of grid block, V (m^3)	50	50	50	50
Fracture porosity, ϕ_f (b/D)	2.93e-4	9.27e-5	2.43e-4	1.11e-4
Fracture volume in grid block ($V*\phi_f$) (m^3)	1.46e-2	4.68e-3	1.22e-2	5.59e-3
Matrix volume in grid block ($V*(1-\phi_f)$) (m^3)	49.9854	49.9953	49.9878	49.9944
Distance between fracture and matrix, d=(D-b)/6 (m)	0.1033	0.3667	0.1233	0.2667
No. of matrix blocks per grid block, σ (V/D^3)	210	4.70	123	12.2
Fracture-matrix connection area on matrix block scale, $A'_{f-m}=2*(D-b)^2$ (m^2)	0.768	0.968	1.09	5.12
Fracture-matrix connection area on grid block scale, $A_{f-m}=A'_{f-m}*\sigma$ (m^2)	161	45.5	135	62.5
Fracture-matrix geometric conductance term, A_{f-m}/d (m)	1.56e3	1.24e2	1.09e3	2.34e2

† The formulation for the fracture volume, matrix volume, and connection area and distance between fracture and matrix elements in this table is also used in the 2-D benchmarks using the dual permeability model. In those cases, one-dimensional fracture sets are assumed for the purposes of calculating fracture-matrix parameters. Note, however, that the volume of the grid blocks, V, used in each benchmark varies.

Table 3.4. Parameters used in FEHMN (see text for explanations of parameters).

	TCw	PTn	TSw1-2	CHnv
RP5	2.0	2.0	2.0	2.0
RP6	0.0312	0.164	0.0553	0.1068
RP11	20.0	20.0	20.0	20.0
RP12	1e-4	1e-4	1e-4	1e-4
APUV1	0.178	0.641	0.214	0.467

saturations are less than one everywhere, and the saturations decrease in the non-welded units where the porosity is greater as shown in Figure 3.4. The DK models that use the fracture-matrix conductance values shown in Table 3.3 produce saturations that are nearly identical to the saturations of the ECM model. This implies that the conductance between the fractures and matrix elements in the DK model is sufficient to allow most of the liquid to be imbibed into the matrix where it is conducted through the matrix continuum. However, when the fracture-matrix conductance is reduced by two orders of magnitude, the matrix saturations of the modified DK model are lower than the saturations of the other models, primarily in the welded Topopah Spring unit. The reduced conductance between the fractures and matrix reduces the steady-state flow through the matrix elements, thereby reducing the matrix saturations as shown in Figure 3.4.

Figure 3.5 shows the steady-state matrix saturations for FEHMN and TOUGH2 using the ECM and DK models at an infiltration rate of 4.0 mm/year. At this infiltration rate, the saturated conductivities of the welded units (TCw and TSw1-2) are exceeded. As a result, Figure 3.5 shows that the steady-state matrix saturations of the welded units are nearly saturated for all the models. In the non-welded units (PTn and CHnv), the modified DK model (in which the fracture-matrix conductance term was reduced by two orders of magnitude) shows a decrease in the saturations relative to the other models. The reduced fracture-matrix conductance allows the flow through the fractures of the welded units to remain in the fractures upon entering the non-welded units. As a result, the matrix saturations in the non-welded units are lower. In addition, even the unmodified DK model produced discrepancies from the ECM saturations at the top of the CHnv (y ~ 130 m). Because the flow is predominantly in the fractures through the welded TSw1-2 unit, the flow in the DK model continued through the fractures into the non-welded CHnv unit a finite distance before being imbibed into the matrix. In contrast, the ECM model assumes equilibrium between the fractures and matrix, so flow is immediately imbibed into the matrix upon entering the CHnv unit.

Figure 3.6 shows the steady-state fracture saturations for FEHMN and TOUGH2 using the unmodified DK model at infiltration rates of 0.1 and 4.0 mm/year. The results are similar for both codes. For 0.1 mm/year, the fracture saturation is near the specified residual saturation of 0.03. It is interesting to note that the fracture saturation in FEHMN is slightly below the specified residual saturation. At 4.0 mm/year, the fracture saturations are significantly higher than the specified residual saturation of 0.0, especially in the welded units (TCw and TSw1-2). This results from a larger flux through the fractures since the matrix units in the welded units are saturated at an infiltration rate of 4.0 mm/year.

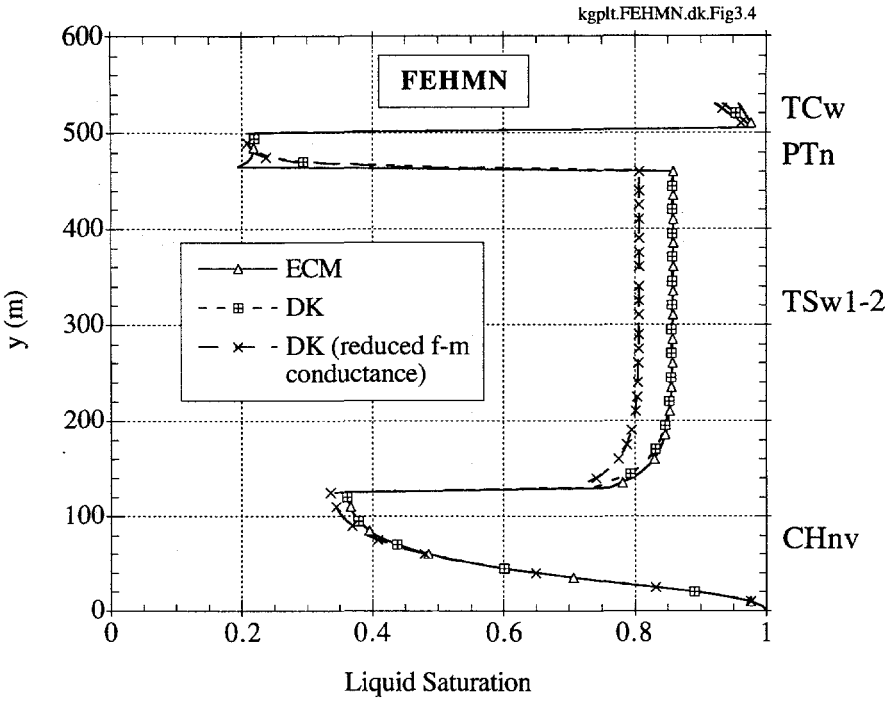

(a)

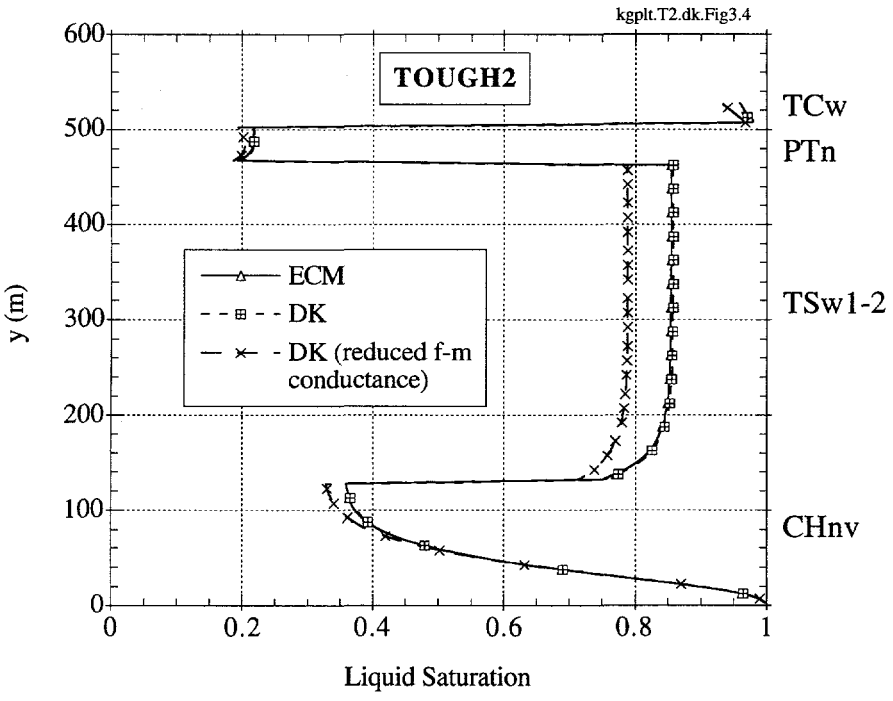

(b)

Figure 3.4. Steady-state matrix saturations for Benchmark 2 comparing ECM and DK models in a) FEHMN and b) TOUGH2. The infiltration rate at the upper boundary was 0.1 mm/year and the bottom boundary was saturated. Appendix B gives a detailed explanation of the reduced f-m conductance DK model.

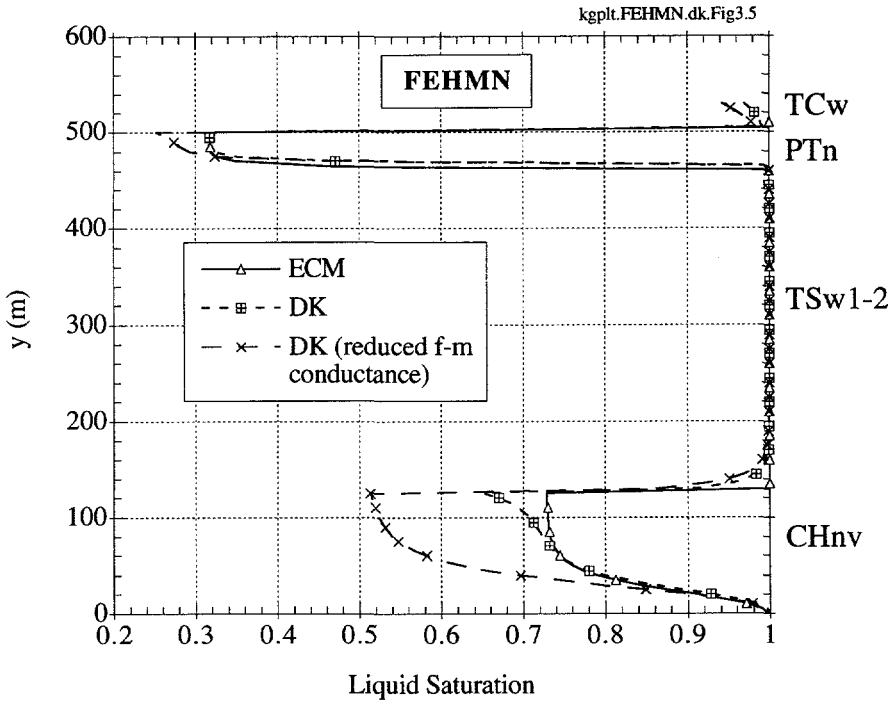

Figure 3.5. Steady-state matrix saturations for Benchmark 2 comparing ECM and DK models in a) FEHMN and b) TOUGH2. The infiltration rate at the upper boundary was 4.0 mm/year and the bottom boundary was saturated. Appendix B gives a detailed explanation of the reduced f-m conductance DK model.

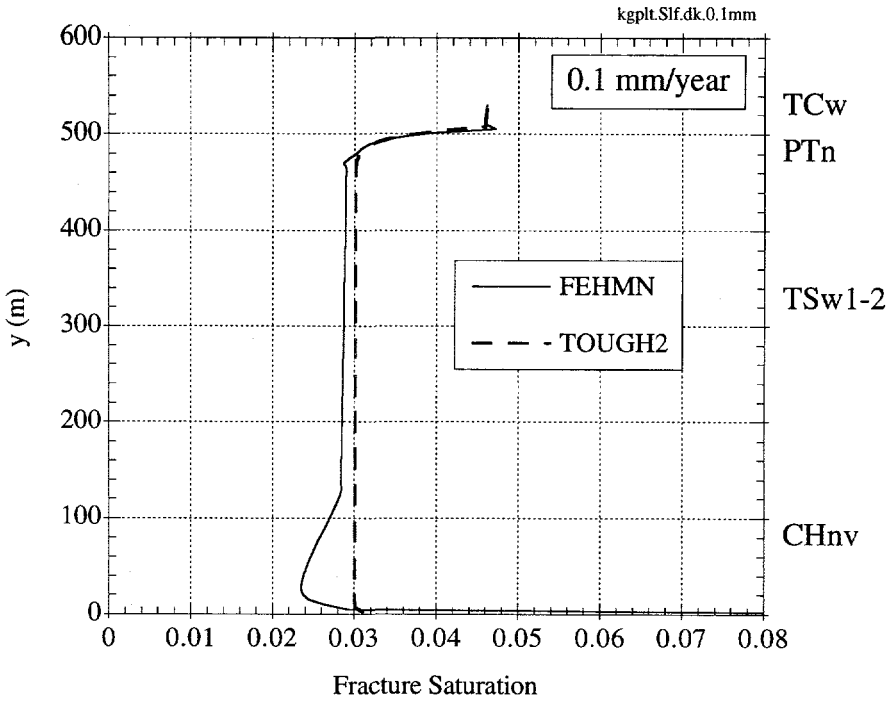

(a)

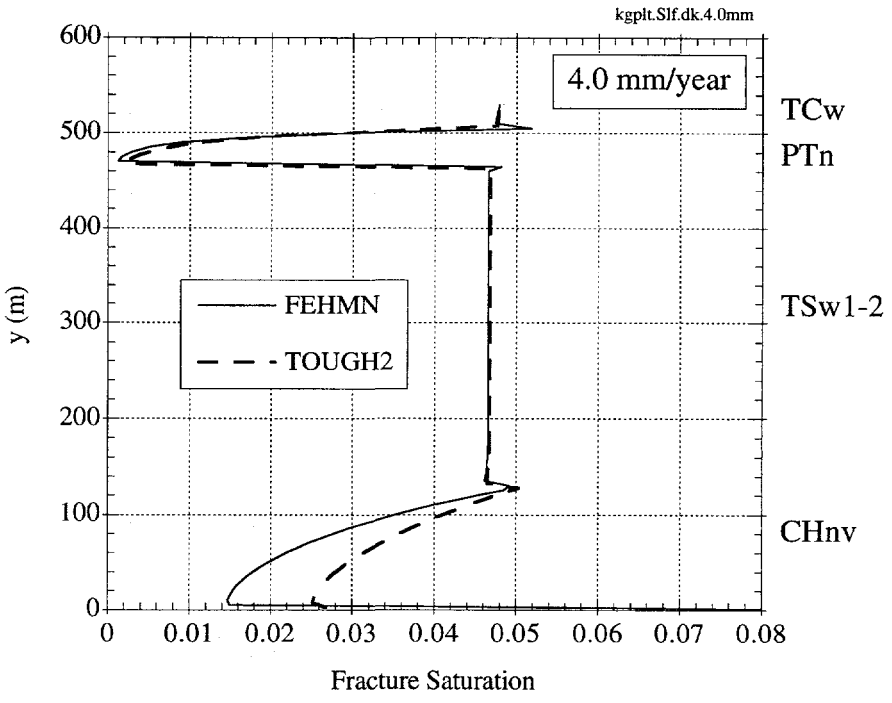

(b)

Figure 3.6. Steady-state fracture saturations for Benchmark 2 using the unmodified DK models in FEHMN and TOUGH2 at infiltration rates of a) 0.1 mm/year and b) 4.0 mm/year. The bottom boundary was saturated. The residual fracture saturations at 0.1 mm/year and 4.0 mm/year were 0.03 and 0.0, respectively.

3.3.3 Velocity and Mass Flow Comparisons

Figures 3.7 and 3.8 show the steady-state pore velocities in the fractures and matrix resulting from the TOUGH2 simulations described above. The composite pore velocity of the ECM is also shown for reference. In Figure 3.7, the pore velocities resulting from an infiltration rate of 0.1 mm/year are shown. As discussed above, the flow is carried entirely through the matrix in the ECM and DK (unmodified) model at this infiltration rate. As a result, Figure 3.7a shows that the matrix velocity is over six orders of magnitude larger than the fracture velocity in the unmodified DK model. However, Figure 3.7b shows that when the fracture-matrix conductance is reduced by two orders of magnitude, the larger flux through the fractures causes the pore velocities in the fractures to exceed the matrix pore velocities.

Figure 3.8 shows the fracture and matrix pore velocities for the DK models used in TOUGH2 at an infiltration rate of 4.0 mm/year. The composite pore velocity of the ECM is also shown for reference. Since the matrix in the welded units is saturated at this infiltration rate, the fracture pore velocities are higher in the welded units in all cases. In the non-welded PTn unit, the unmodified DK model shown in Figure 3.8a yields higher matrix velocities as a result of significant flow from the fractures to the matrix in that region. However, when the fracture-matrix conductance is reduced by two orders of magnitude, Figure 3.8b shows that the velocities in the fractures dominate everywhere, even in the non-welded PTn. It should be noted that although the fracture-matrix conductance was reduced by two orders of magnitude in all the units in this problem, arguments can be made to justify the reduction of the conductance in only the welded units. Recall that the justification for reducing the conductance between the fractures and matrix is based on small-scale process such as fingering and channeling, which is often evidenced in the welded tuffaceous rocks. However, physical observations of flow through samples of the non-welded tuffs reveal behavior similar to that of a sponge—rapid imbibition of infiltrating flow. This seems to indicate high conductance should exist between the fractures and matrix in the non-welded units, and no reductions should be made.

Figure 3.9 shows the mass flow rates between the fractures and matrix in the TOUGH2 simulations at infiltration rates of 0.1 and 4.0 mm/year. Positive mass flow rates denote flow from the fractures to the matrix, and negative mass flow rates denote flow from the matrix to the fractures. Figure 3.9a shows that at an infiltration rate of 0.1 mm/year, flow is everywhere from the fractures to the matrix. Recall that this infiltration rate is lower than the saturated conductivity of all the matrix units, so flow can be sustained entirely in the matrix. In addition, the modified DK model in which the fracture-matrix conductance is reduced by two orders of magnitude shows a lower mass flow from the fractures to the matrix in the upper TCw unit than the unmodified DK

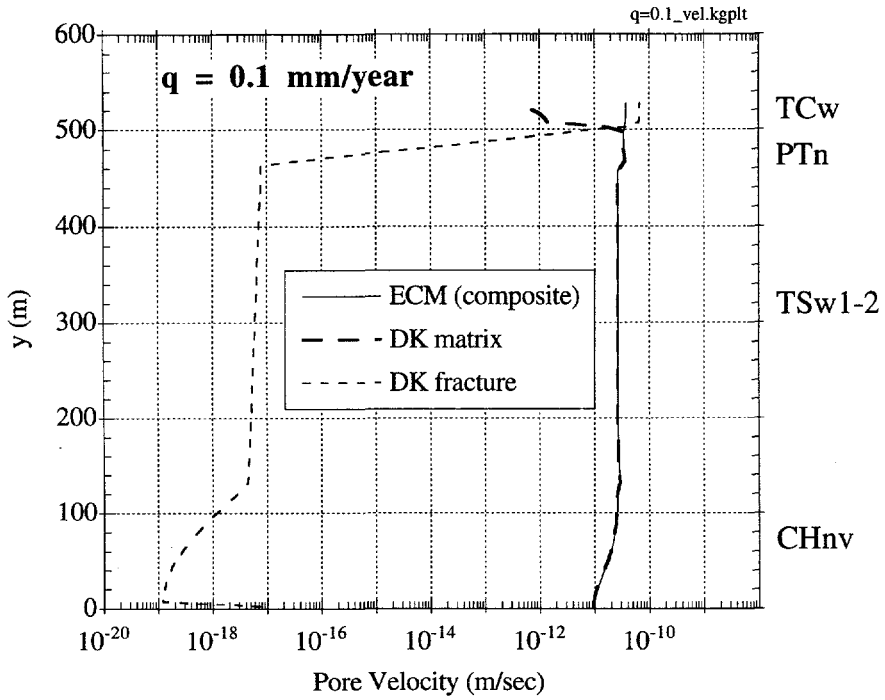

(a)

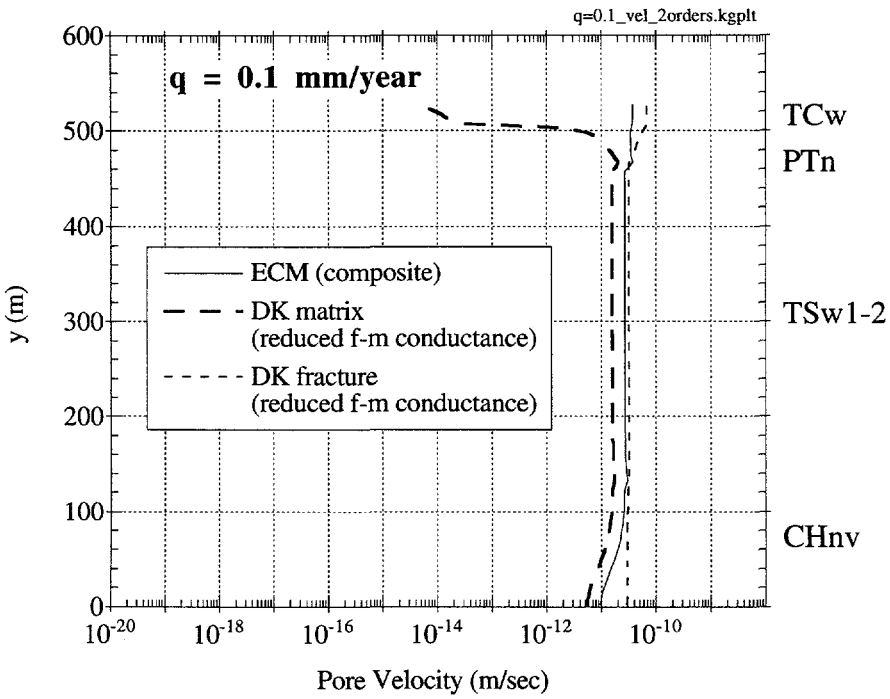

(b)

Figure 3.7. Steady-state TOUGH2 pore velocities in the fractures and matrix: a) unmodified DK model; b) modified DK model with fracture-matrix conductance reduced by two orders of magnitude (see Appendix B). The composite ECM velocity is shown for reference. The infiltration rate is 0.1 mm/year.

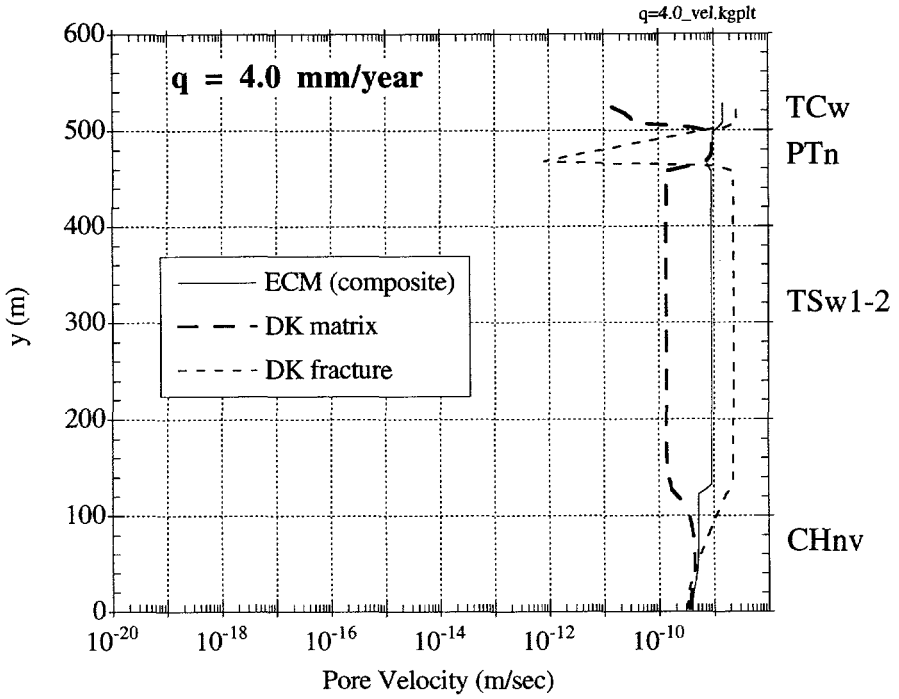

(a)

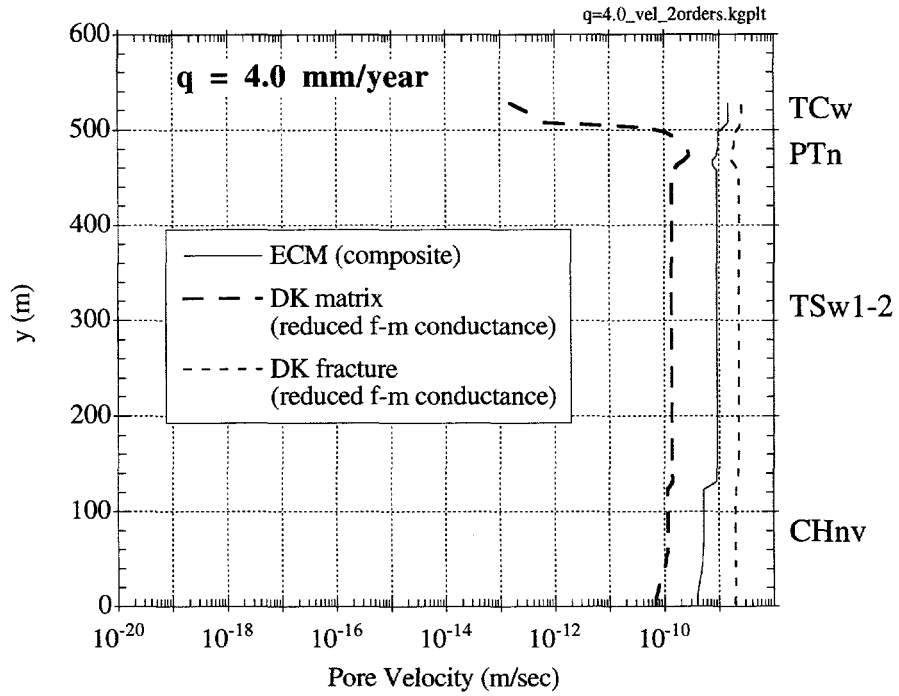

(b)

Figure 3.8. Steady-state TOUGH2 pore velocities in the fractures and matrix: a) unmodified DK model; b) modified DK model with fracture-matrix conductance reduced by two orders of magnitude (see Appendix B). The composite ECM velocity is shown for reference. The infiltration rate is 4.0 mm/year.

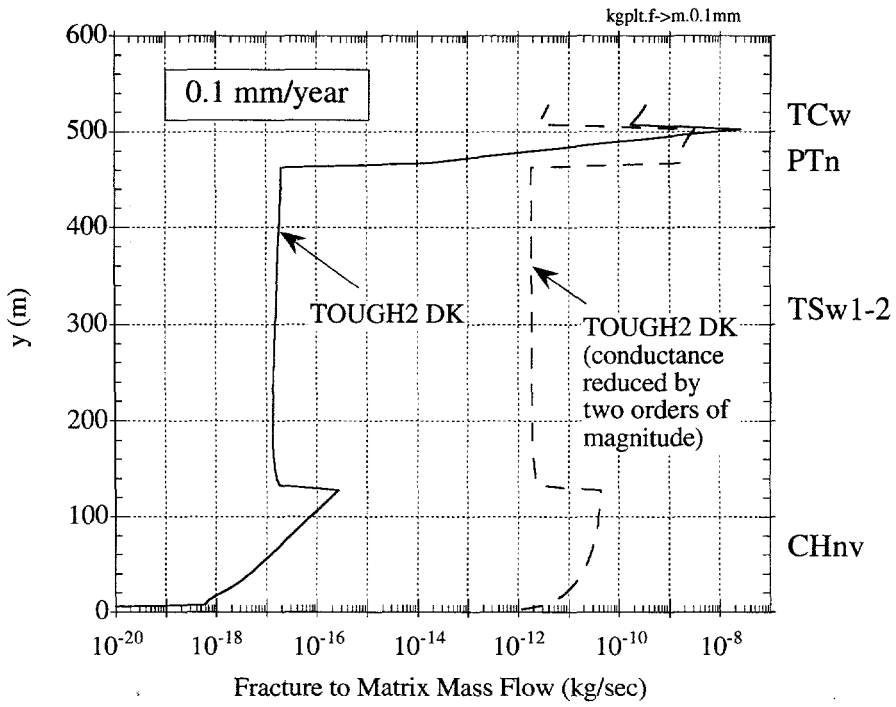

(a)

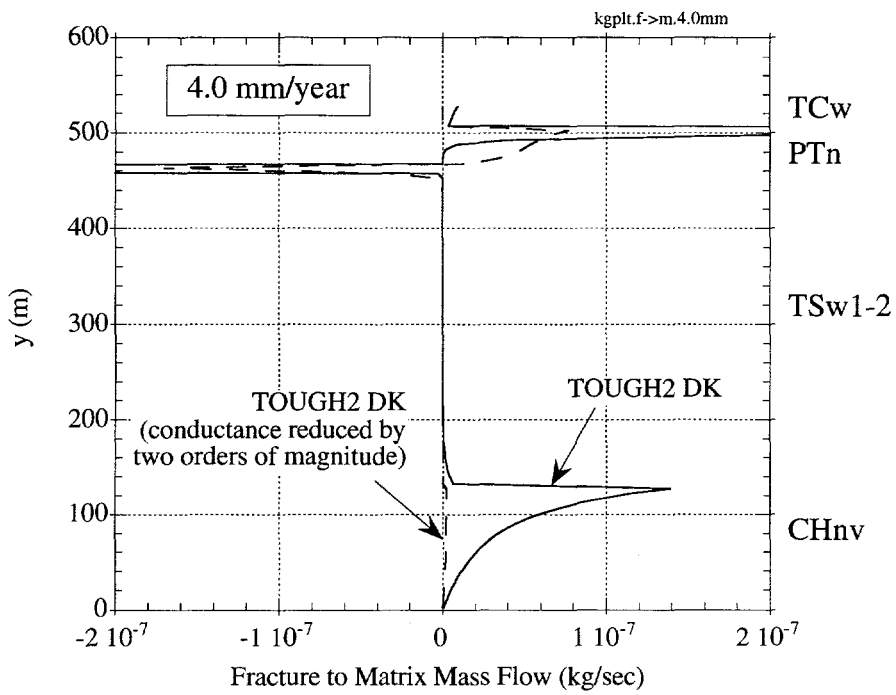

(b)

Figure 3.9. Steady-state TOUGH2 DK mass flow rates between the fracture and matrix elements at a) 0.1 mm/year and b) 4.0 mm/year. Positive values denote flow from the fractures to the matrix, and negative values denote flow from the matrix to the fractures. The bottom boundary is saturated.

model. This results in a larger overall flux through the fractures and, subsequently, more flow from the fractures to the matrix in the lower units. At 4.0 mm/year, Figure 3.9b shows that the mass flow between the fractures and matrix changes direction at the interface of the PTn and TSw1-2 units. The saturated matrix of the welded TSw1-2 cannot sustain the entire flow coming from the non-welded PTn matrix above, so excess liquid flows from the matrix to the fractures at the top of the TSw1-2 unit. Below this unit, flow once again returns into the matrix in the non-welded CHnv unit. However, when the fracture-matrix conductance is reduced by two orders of magnitude, the mass flow exchanges between the fractures and matrix at the unit interfaces is dampened out significantly as shown in Figure 3.9b.

3.3.4 Remarks

In these steady-state simulations, the DK model is seen to produce similar results to the ECM when the conductance between the fractures and matrix is sufficiently large. The calculated fracture-matrix conductances in Table 3.3 assume that the entire fracture-matrix connection area is available to flow, but due to small scale processes such as fingering and channeling (Glass and Tidwell, 1991) or mechanical aspects such as fracture coatings (Thoma et al., 1990), the effective fracture-matrix conductance can be much smaller. When the conductance is reduced by two orders of magnitude, the DK model shows differences in the fracture and matrix velocities—even at steady-state. Intuitively, it makes sense that transient responses to an infiltration event would be different if the fracture-matrix conductance is altered, but the behavior of DK systems under steady-state conditions is perhaps not so intuitive. Figure 3.10 shows a few elements from the one-dimensional DK model used in this problem. Figure 3.10 also shows Darcy's law as applied to the flow between a fracture and a matrix element. At steady-state, the mass flow into any element must equal the mass flow out of that element. If the fracture-matrix conductance is reduced, the overall mass flow rate through the matrix is also lowered, thereby reducing the matrix saturation. The result is a larger mass flow rate through the fractures.

In addition to the geometric conductance term listed in Table 3.3 (see Appendix B for derivation), the capillary pressure gradient also contributes to the mass flow between the fracture and matrix elements as shown in the equation in Figure 3.10. These gradients are influenced by the infiltration rate and the subsequent saturation distributions in the fractures and in the matrix. This explains why the 4.0 mm/year infiltration cases did not result in a change in the matrix saturations or velocities in the welded units for the different models. At this infiltration rate, the matrix in the welded units becomes saturated and minimal flow occurs between the fractures and matrix as shown in Figure 3.9b. In this case, flow in the fractures dominates in the welded units regardless of the fracture-matrix geometric conductance term.

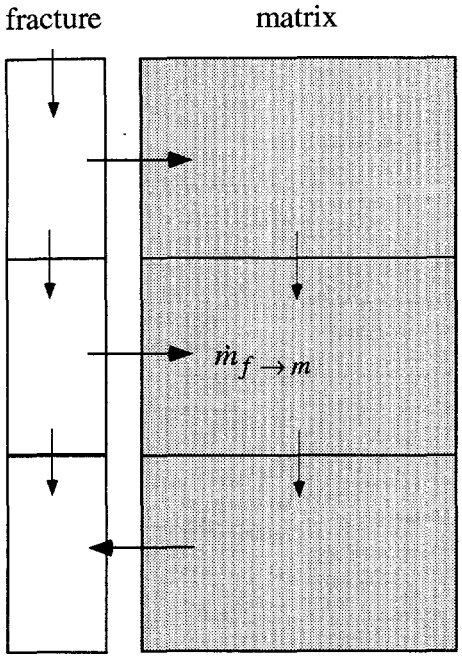

$$\dot{m}_{f \to m} = \rho A_{f-m} \frac{k_m k_{rm}}{\mu} \frac{P_{l,f} - P_{l,m}}{d}$$

Since $P_c = P_g - P_l$, and for P_g constant:

$$\dot{m}_{f \to m} = \rho T \frac{k_m k_{rm}}{\mu} \left(P_{c,m} - P_{c,f} \right)$$

where $T \equiv$ geometric conductance term

$$= \frac{A_{f-m}}{d}$$

Figure 3.10. Mass flow between fracture and matrix elements in a one-dimensional dual permeability model. The mass flow is expressed as a function of the geometric conductance term described in Appendix B.

3.4 Single-Phase vs. Two-Phase Simulations

The purpose of this section is to compare the single-phase and two-phase models in TOUGH2 and FEHMN using the Benchmark 2 problem. The parameters in Tables 3.2 and 3.4 are used along with the ECM in all cases.

Figure 3.11 shows the steady-state ECM saturations of the single- and two-phase simulations using FEHMN and TOUGH2 for infiltration rates of 0.1 mm/year and 4.0 mm/year. The single- and two-phase results of FEHMN are nearly identical at both infiltration rates. The FEHMN results are also very similar to the single-phase TOUGH2 results for both infiltration rates. However, the two-phase TOUGH2 results show slightly higher saturations in the CHnv unit in both cases. Overall, the saturations are quite similar between the single- and two-phase models for both FEHMN and TOUGH2. Table 3.5 gives the elapsed simulation times for these runs. As expected, the single-phase version of TOUGH2 produced significantly faster run times—nearly 20 times faster than the corresponding two-phase simulation. Recall that in the single-phase simulation, the balance laws for energy and the air component are eliminated. Therefore, fewer equations need to be solved for each element. However, the simulation times for FEHMN were similar for the single- and two-phase simulations. In fact, the single-phase simulations took *longer* to run than the corresponding two-phase simulations for FEHMN. Attempts to investigate this seemingly peculiar behavior have not been made.

Table 3.5. Calculation times using single- and two-phase versions of FEHMN and TOUGH2 for Benchmark 2. (Note: Final simulation time was 10^9 years)

	Elapsed Time (sec)			
	TOUGH2		FEHMN (5-95 version)	
	single-phase	two-phase	single-phase	two-phase
0.1 mm/year	89.12	1,690	1,959	1,671
4.0 mm/year	87.09	1,727	1,848	1,655

3.5 Summary

In this chapter, comparisons of the codes DUAL, FEHMN, and TOUGH2 have been made for steady infiltration into a layered one-dimensional domain. The comparison of the codes revealed that FEHMN and TOUGH2 yielded very similar saturation profiles for infiltration rates ranging from 0.1 mm/year to 4.0 mm/year. Further comparisons of these codes with previous

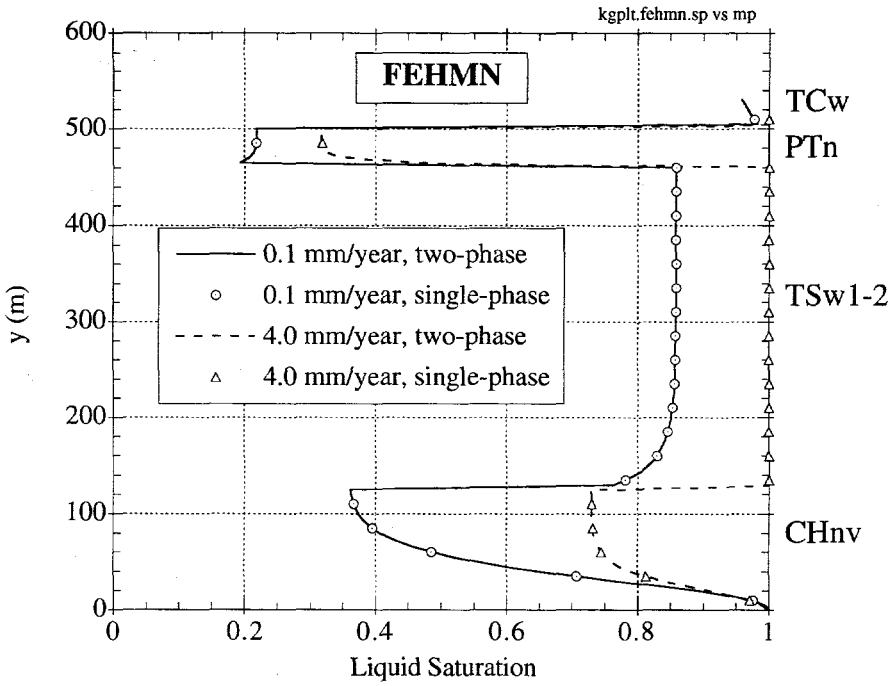

(a)

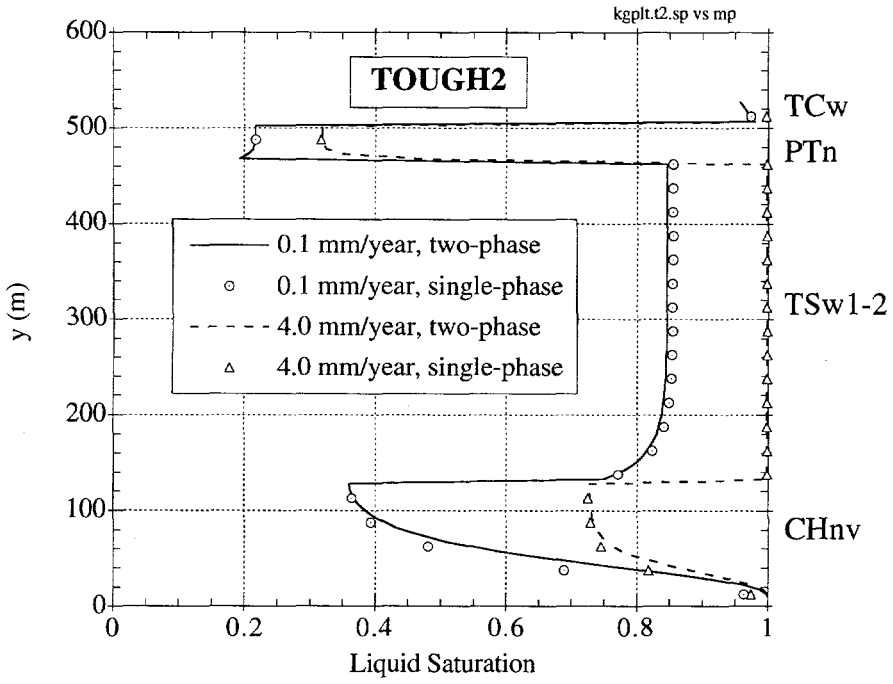

(b)

Figure 3.11. Steady-state ECM matrix saturations in a one-dimensional layered column using single- and two-phase versions of a) FEHMN and b) TOUGH2. The infiltration rate at the top is either 0.1 or 4.0 mm/year, and the bottom boundary is saturated.

analysis by Dykhuizen and Barnard (1992) showed that the results were consistent with other codes. The DUAL code, however, had troubles simulating infiltration rates other than 0.2 mm/year. At this infiltration rate, the resulting saturation profiles from DUAL were lower than the saturations of either FEHMN or TOUGH2. This discrepancy was consistent with the results of Benchmark 1, which showed that DUAL produced lower saturations for infiltration into a homogeneous one-dimensional domain.

The ECM and DK models were also compared using FEHMN and TOUGH2. The formulation of the DK models in FEHMN and TOUGH2 were discussed, and it was concluded that the geometric conductance term between the fractures and matrix could be made equivalent between the two codes through the appropriate specification of a length scale parameter in FEHMN. The parameter, APUV1, in FEHMN should be set equal to the fracture spacing divided by $\sqrt{12}$ (see Appendix B). In addition, a discussion of the appropriateness of reducing this conductance term based on small-scale processes that reduce the wetted area of a fracture was presented. Results showed that the two codes produced similar saturation profiles for both the ECM and DK models at infiltration rates of 0.1 and 4.0 mm/year. The ECM and DK models produced nearly identical results for 0.1 mm/year (nearly all matrix flow), but at 4.0 mm/year, discrepancies were observed. At this higher infiltration rate, significant fracture flow existed, and the DK model showed evidence of further propagation of flow in the fractures than the ECM. Reducing the conductance between the fractures and matrix by two orders of magnitude had a noticeable effect on the saturation profiles at 0.1 and 4.0 mm/year. A more pronounced effect was seen in the fracture flow velocity profile before and after reducing the conductance. At 0.1 mm/year, reducing the conductance resulted in fracture velocities that were six orders of magnitude greater than the fracture flow velocity before reducing the conductance. At a higher infiltration rate of 4.0 mm/year, significant fracture flow already existed in the welded units, so changes in those units were minimal when the fracture-matrix conductance was reduced. Because the conductance between the fractures plays such an important role in transient *and* steady-state velocity and saturation profiles, it would be desirable to quantify the fracture-matrix conductance term through field studies or laboratory experiments.

Comparisons of the single- and two-phase models in FEHMN and TOUGH2 were assessed using the ECM model of infiltration into the layered one-dimensional domain. Results showed that the single- and two-phase results were identical for FEHMN. On the other hand, the two-phase steady-state saturations resulting from TOUGH2 were slightly higher in the CHnv unit than the saturations resulting from the single-phase models in TOUGH2 and FEHMN. The simulation time was significantly reduced when the single-phase version of TOUGH2 was used. Calculation times

using the single-phase version of TOUGH2 were nearly 20 times faster than the two-phase version. FEHMN, however yielded similar simulation times for both the single- and two-phase models.

Chapter

FOUR

Benchmark 3: Layered 2-D Infiltration

This chapter continues the analysis of alternative conceptual models and codes using a two-dimensional domain. The use of a two-dimensional domain with dipping layers can allow lateral diversion of flow to occur at unit interfaces. In addition, the effects of using a localized, rather than uniform, source of infiltration along the top boundary is studied. Finally, alternative conceptual models of fracture flow are assessed for this two-dimensional domain with dipping layers.

The progression of this chapter is as follows. First, a description of the domain used in this third benchmark is given. Then, results of TOUGH2 numerical simulations using the ECM are provided. The existence and effects of capillary barriers using different infiltration rates are discussed for this problem. A comparison between the equivalent continuum model (ECM) and the dual permeability (DK) model of this two-dimensional infiltration problem are then presented, and the effects of reducing the fracture-matrix conductance in the DK model (see Appendix B) are examined. The effects of using a localized source of infiltration are then presented using TOUGH2. Finally, comparisons are made between TOUGH2 and FEHMN for ECM simulations of Benchmark 3.

4.1 Description of Benchmark 3

The two-dimensional domain considered here consists of three homogeneous layers: 1) TCw 2) PTn and 3) TSw (see Figure 4.1). The domain extends 1000 meters in the horizontal direction and 500 meters in the vertical direction[†] . Each element is 50 meters wide by 10 meters high;

[†] These dimensions correspond to the unrotated domain shown in Figure 3.1. The true x and y dimensions can be obtained by using the following rotation transformation: $x_{rotated}=x\cdot\cos(6.7^\circ)+y\cdot\sin(6.7^\circ)$, $y_{rotated}=y\cdot\cos(6.7^\circ)-x\cdot\sin(6.7^\circ)$. The unrotated dimensions are used to facilitate easier interpretation of the post-processed results using TOUGH2.

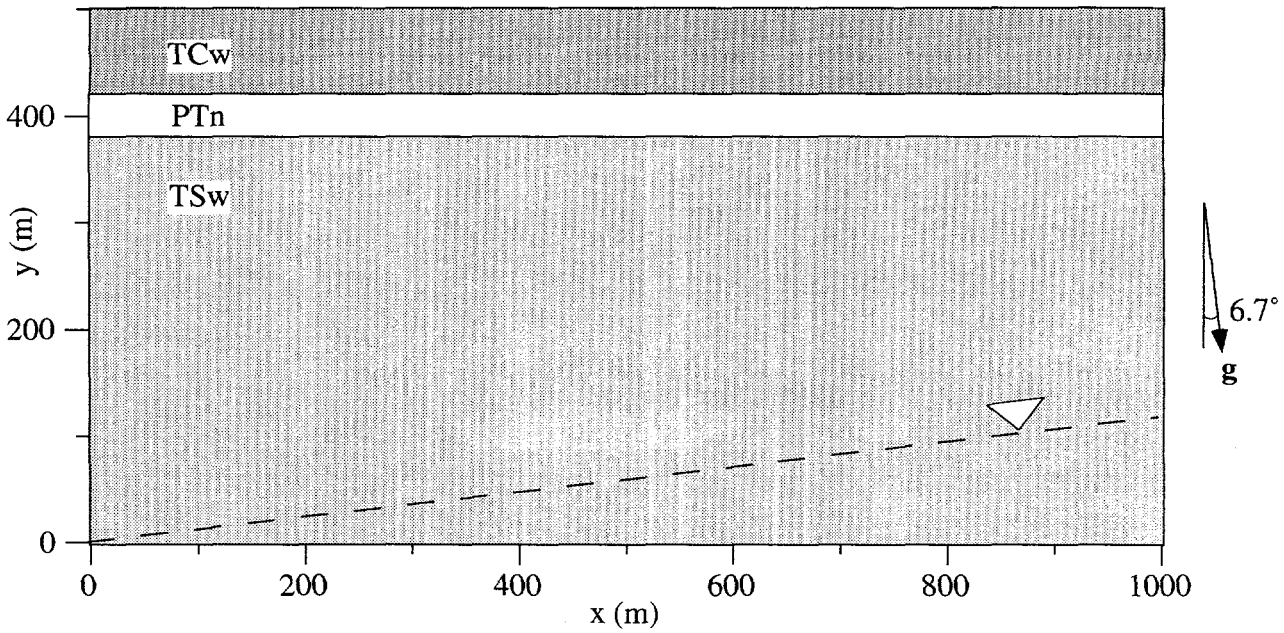

Figure 4.1. Two-dimensional layered domain used in Benchmark 3 for TOUGH2. Each layer is homogeneous. The thicknesses of the TCw, PTn, and TSw units are 80 m, 40 m, and 380 m, respectively. The material properties are given in Table 3.2. The gravity vector is rotated 6.7° to simulate dipping units.

vertical direction for a total of 1000 elements. The layers are dipping at an angle of 6.7°, and this is represented in Figure 4.1 by the tilted gravity vector. The thicknesses of the TCw, PTn, and TSw units are 80 m, 40 m, and 380 meters, respectively. The material properties are taken from TSPA-93 using expected values from entropy fits of sampled data (see Table 3.2 of the previous chapter).

Boundary conditions are applied along the top and bottom of the domain, while no flux is allowed through the sides. Various infiltration rates are applied along the top row of elements (in the DK models, the infiltration is applied to the fracture elements only), and later in the chapter the effects of using a localized source of infiltration at only one element are presented. The bottom boundary is specified such that a water table is level with the bottom left corner of the domain (see Figure 4.1). In the single-phase version of TOUGH2, this is accomplished by specifying the pressure along the bottom boundary to be equal to the reference (ambient) pressure plus the appropriate hydrostatic pressure. This produces the desired hydrostatic saturation distribution (with no infiltration) as shown in Figure 4.2. Although this distribution seems to be the natural starting point for subsequent infiltration analyses, an initial uniform saturation of 0.85 is specified in these analyses to expedite the steady-state solution as described in the previous chapter.

The original intent of this benchmark was to compare DUAL, FEHMN, and TOUGH2 using a two-dimensional layered domain. However, initial attempts to simulate this problem with DUAL have been unsuccessful. As a result, this report presents results for Benchmark 3 from TOUGH2 and FEHMN only. The single-phase version of TOUGH2 discussed in Chapters 2 and 3 is used for the analyses in section 4.2, and the most recent version of FEHMN (FEHMN 95-05-01p-sun4) is used in the analyses in section 4.3.

4.2 TOUGH2 Results for Benchmark 3

4.2.1 Capillary Barrier Effects

Due to the layering of different geologic units in this problem, infiltrating water can be laterally diverted at the interfaces of the units. Capillary pressure differences between different geologic units can create capillary barriers depending on the saturations of the units. Under unsaturated conditions (infiltration rates ≤ 0.1 mm/year), the higher porosity PTn unit can act as a capillary barrier to flow coming from the lower porosity TCw unit above. For higher infiltration rates ≥ 1.0 mm/year, the saturated TSw unit can act as a capillary barrier to flow coming from the unsaturated PTn unit above. These hypotheses are tested in this section with TOUGH2

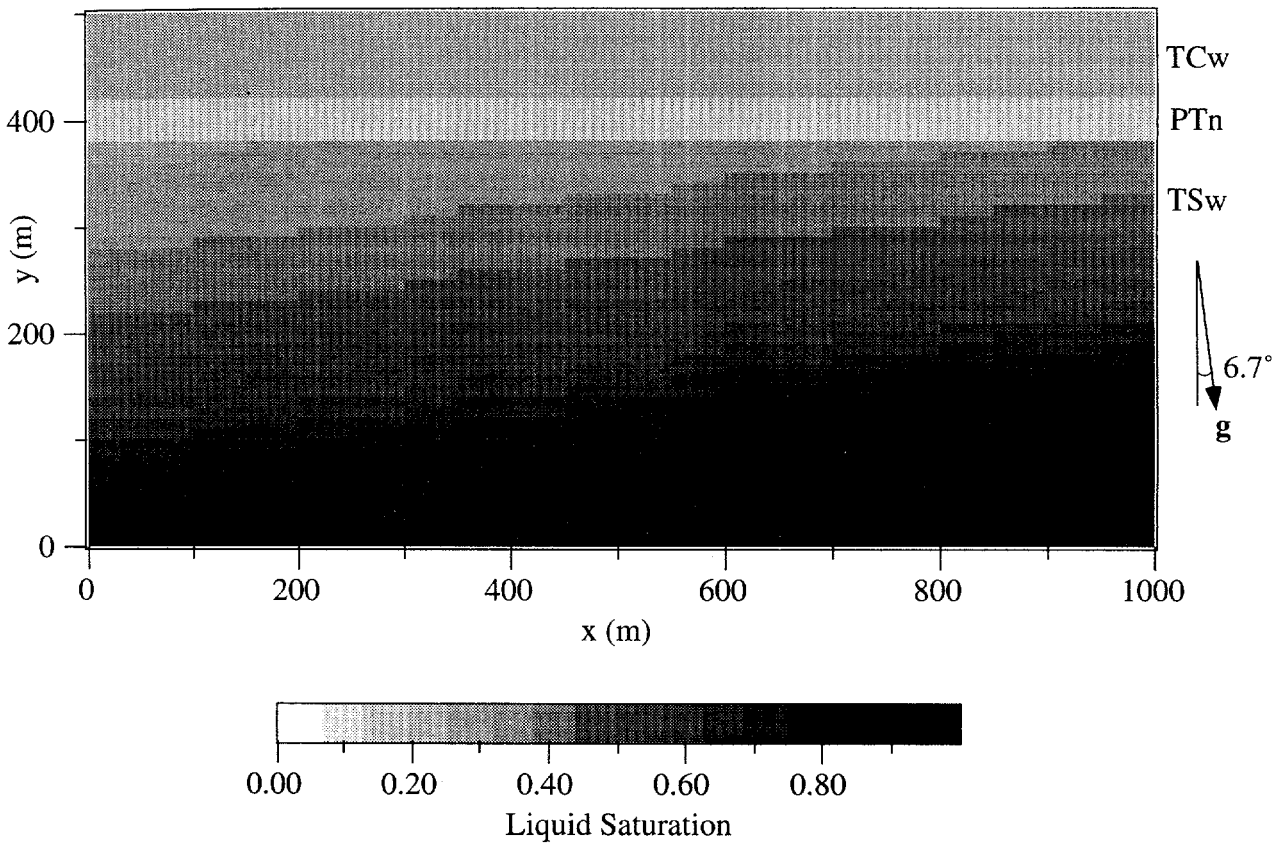

Figure 4.2. Hydrostatic saturation distribution for TOUGH2 model of Benchmark 3 with rotated gravity vector.

simulations using the ECM at infiltration rates above and below the saturated conductivities of the welded units.

Infiltration Rate = 0.1 mm/year

Figure 4.3 shows the steady-state matrix saturations and pore velocities for a uniform infiltration rate of 0.1 mm/year. This infiltration rate is below the saturated conductivities of the welded units, so the steady-state saturations are less than one everywhere above the water table and flow is entirely governed by matrix properties. The saturations are greater toward the down-dip (right) side of the domain as a result of the no-flow vertical boundaries. A better quantification of the range of saturations throughout the entire domain can be observed in Figure 4.4, where the saturation of each element has been plotted as a small horizontal line. This yields a nearly continuous horizontal line spanning the range of saturations for each row of elements. The lower saturations plotted in Figure 4.4 correspond to the left side of the domain, and the higher saturations correspond to the right side where water accumulates. The average values of the saturations are seen to correspond closely with the corresponding saturations resulting from the one-dimensional problem in Benchmark 2 (Figure 3.4).

The velocities in Figure 4.3 reveal that the majority of flow is in the vertical direction. A slight diversion of flow at the top of the PTn can be seen in Figure 4.3, but further evidence can be seen in Figure 4.5. Figure 4.5 shows the x-component of the velocity parallel to the dipping layers for several different rows of elements in and around the PTn. The hollow triangles pointing downward represent elements directly above the TCw-PTn interface, while the hollow triangles pointing upward represent elements directly beneath the interface. Figure 4.5 shows that the elements above the TCw-PTn interface have a much stronger x-component of the velocity than elements in the PTn or below. This indicates that flow is being laterally diverted at the TCw-PTn interface because of capillary pressure differences as discussed earlier.

Infiltration Rate = 4.0 mm/year

Figure 4.6 shows the steady-state matrix saturations and pore velocities for a uniform infiltration rate of 4.0 mm/year. This infiltration exceeds the saturated conductivities of the welded units, so saturated conditions exist everywhere except for the non-welded PTn unit. Figure 4.7 shows the range of saturations for this case. Flow in the fractures plays an important role in the welded units at this high infiltration rate as discussed in section 3.3.3 of the previous chapter. Flow in the matrix appears to be uniformly downward in this case, but Figure 4.8 shows that the x-component of velocity parallel to the dipping layers varies greatly in and near the PTn. The x-component of the velocity directly above the PTn-TSw interface (shown by solid triangles pointing

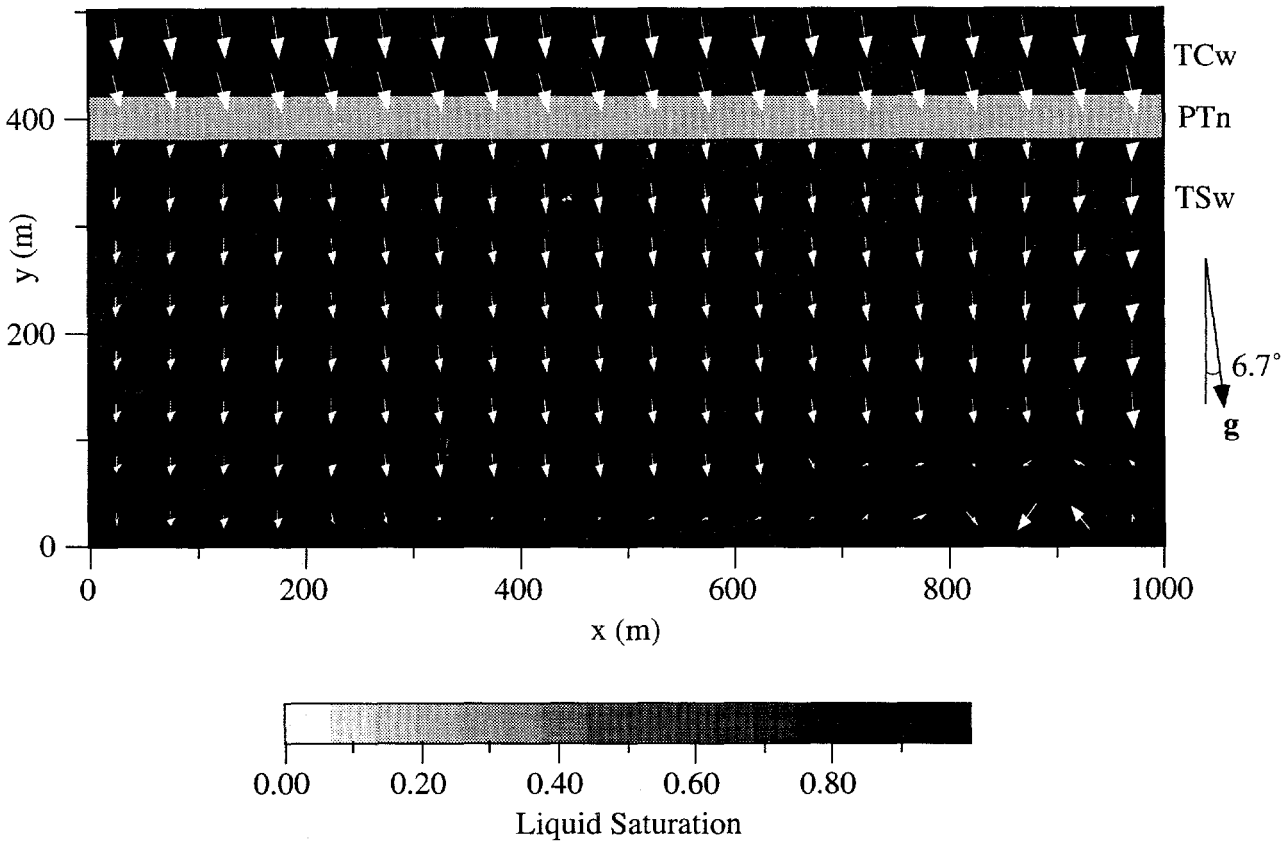

Figure 4.3. Steady-state TOUGH2 ECM matrix saturations and pore velocities at a uniform infiltration rate of 0.1 mm/year (Darcy velocity). The vectors are scaled to a maximum pore velocity of 1.5 mm/year.

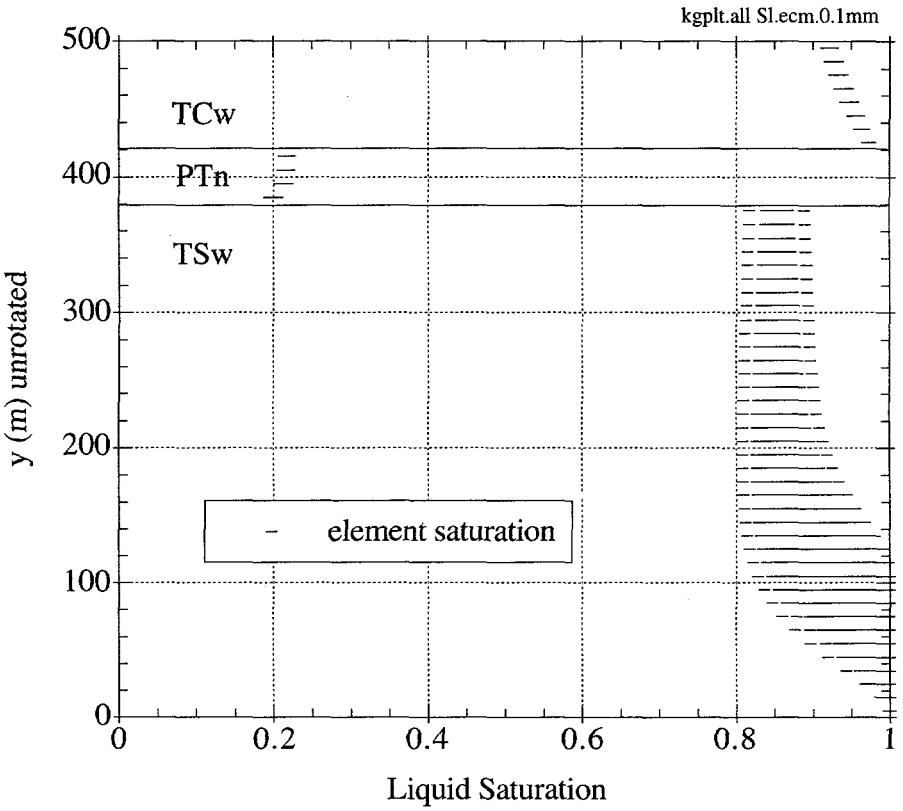

Figure 4.4. Range of matrix saturations simulated by TOUGH2 using the ECM at an infiltration rate of 0.1 mm/year for Benchmark 3. Each element's saturation is plotted as a small horizontal line so that a nearly continuous line spans the range of saturations for each row of elements.

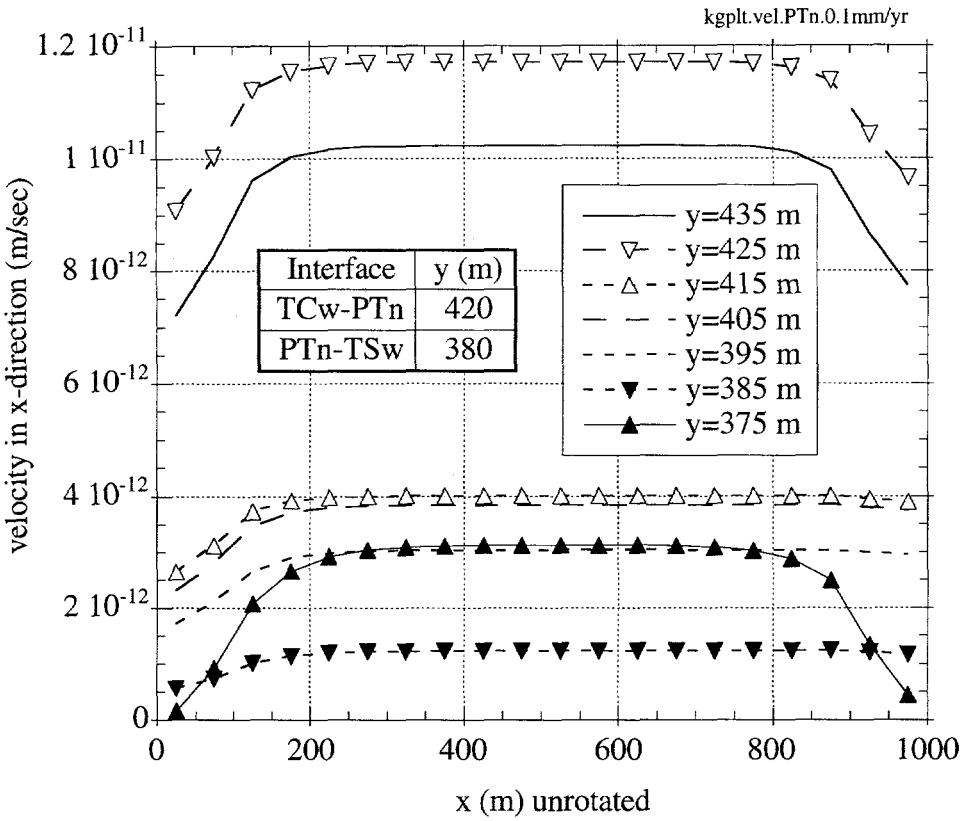

Figure 4.5. TOUGH2 ECM matrix velocites in the x-direction (parallel to the units) along seven horizontal transects in and around the PTn unit at an infiltration rate of 0.1 mm/year. The triangles denote locations at unit interfaces. Higher velocites in the x-direction above the PTn in this case indicate capillary diversion at the TCw-PTn interface.

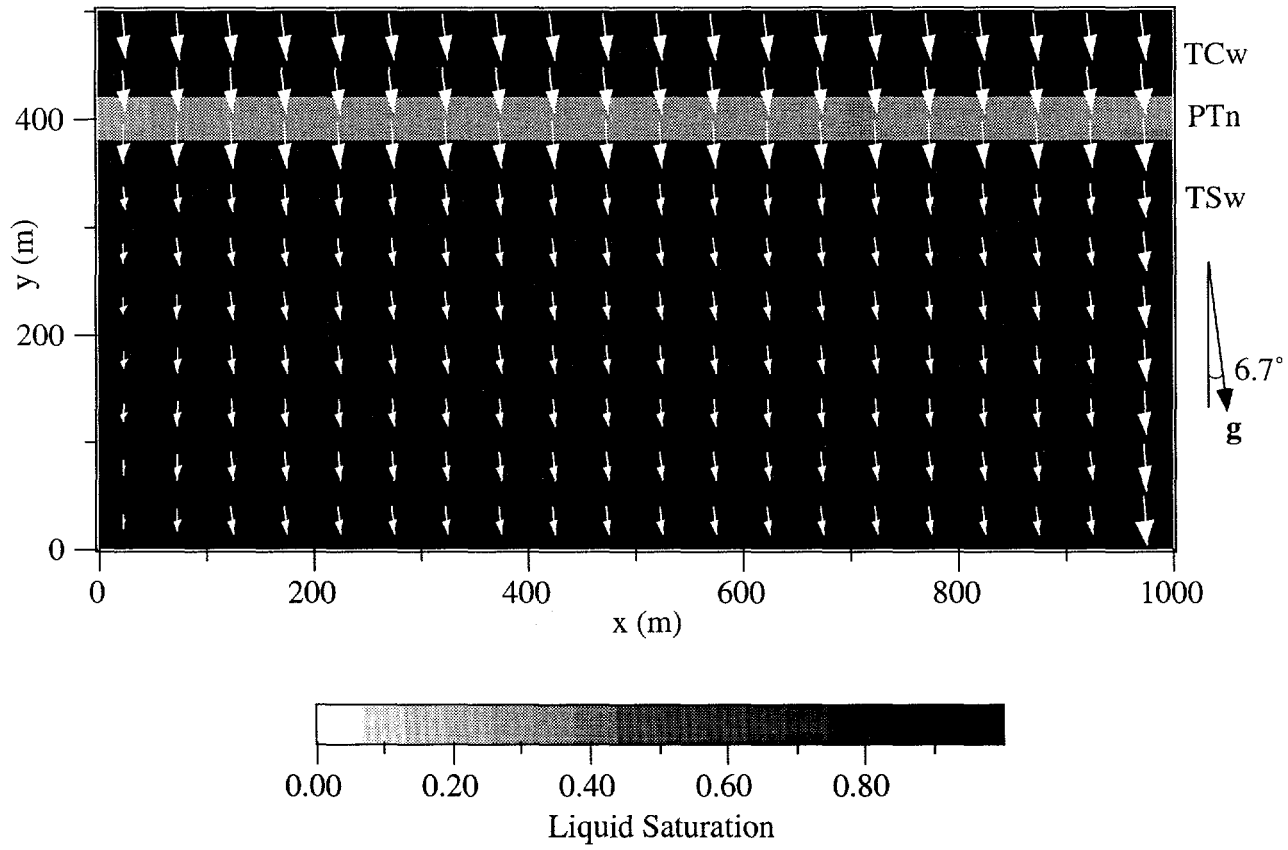

Figure 4.6. Steady-state TOUGH2 ECM matrix saturations and pore velocities at a uniform infiltration rate of 4.0 mm/year (Darcy velocity). The vectors are scaled to a maximum pore velocity of 54 mm/year.

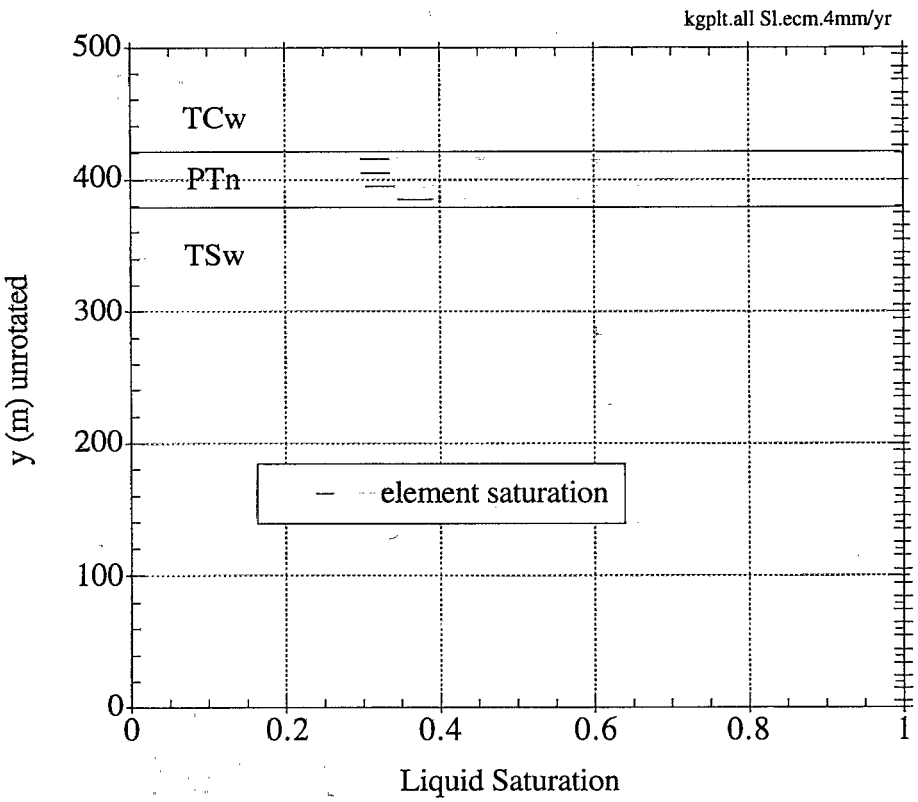

Figure 4.7. Range of matrix saturations simulated by TOUGH2 using the ECM at an infiltration rate of 4.0 mm/year for Benchmark 3. Each element's saturation is plotted as a small horizontal line so that a nearly continuous line spans the range of saturations for each row of elements.

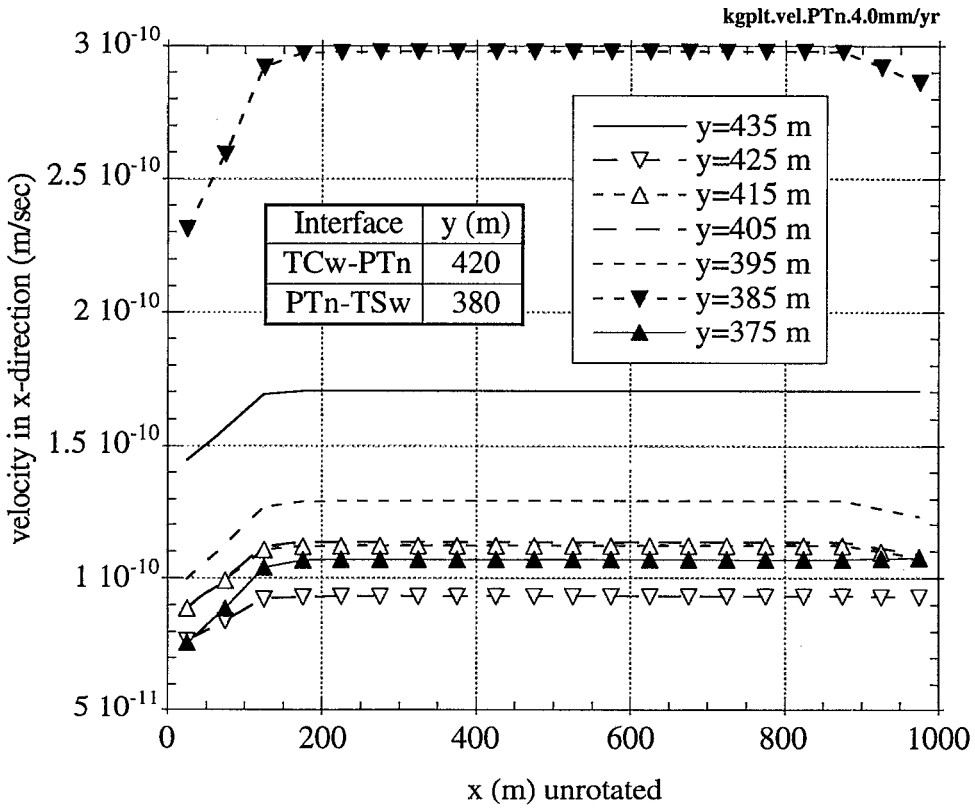

Figure 4.8. TOUGH2 ECM matrix velocites in the x-direction (parallel to the units) along seven horizontal transects in and around the PTn unit at an infiltration rate of 4.0 mm/year. The triangles denote locations at unit interfaces. Higher velocites in the x-direction just above the bottom boundary of the PTn in this case indicate capillary diversion at the PTn-TSw interface.

component of the velocity directly above the PTn-TSw interface (shown by solid triangles pointing downward) is much greater than the x-component of the velocity directly beneath that interface (shown by solid triangles pointing upward) or anywhere else in or around the PTn. This indicates that flow is being laterally diverted at the PTn-TSw interface as a result of capillary pressure and conductivity differences between the saturated TSw and the unsaturated PTn. This is in contrast to the lower infiltration case where the capillary barrier† effect was observed at the *top* of the PTn at the TCw-PTn interface.

These results show that depending on the saturations of various layers, capillary barriers can exist in different locations. For the unsaturated conditions prevalent at Yucca Mountain near the PTn, lateral diversion of flow will most likely occur at locations where the material having a higher capillary suction overlies a material with lower capillary suction. This can occur if the underlying material has a much higher porosity than the material above (e.g. at the interface of the TCw and PTn units). In addition, capillary barriers can occur if poor contact exists between two materials, providing local regions of high porosity (and hence low capillary suction) between the materials.

Remarks

Previous studies by Prindle and Hopkins (1990) have investigated the behavior of lateral diversion using a similar domain. Their results show much greater lateral diversion in the PTn, especially for higher infiltration rates. It is hypothesized that the discrepancies result from the different material properties that were used. In Prindle and Hopkins (1990), the parameters were obtained from Klavetter and Peters (1986) as shown in Table 3.1, whereas in the current study, the parameters were taken from TSPA-93 (Wilson et al., 1994) as shown in Table 3.2. The parameters governing the two-phase characteristic curves for the PTn unit are significantly different between the two data sets. In particular, the air entry parameter for the PTn matrix, α (1/Pa), is an order of magnitude smaller in Klavetter and Peters (1986). This smaller air entry parameter increases the overall moisture retention potential in the PTn, which may contribute to the greater lateral diversion observed in Prindle and Hopkins (1990). To verify this hypothesis, the 4 mm/year infiltration case is simulated using parameters from Klavetter and Peters (1986) for the PTn unit only. All other parameters for the TCw and TSw units are taken from TSPA-93 (Wilson et al., 1993). Figure 4.9 shows that the change in PTn parameters yields significantly more lateral diversion in the PTn unit, consistent with the results of Prindle and Hopkins (1990). Local velocities are also higher in this case as a result of the focused flow through the PTn to the right edge of the domain boundary. These results indicate that the choice of two-phase parameters for

† A more appropriate term describing the behavior observed here is "capillary diversion" since flow is still occurring across the interface of the units.

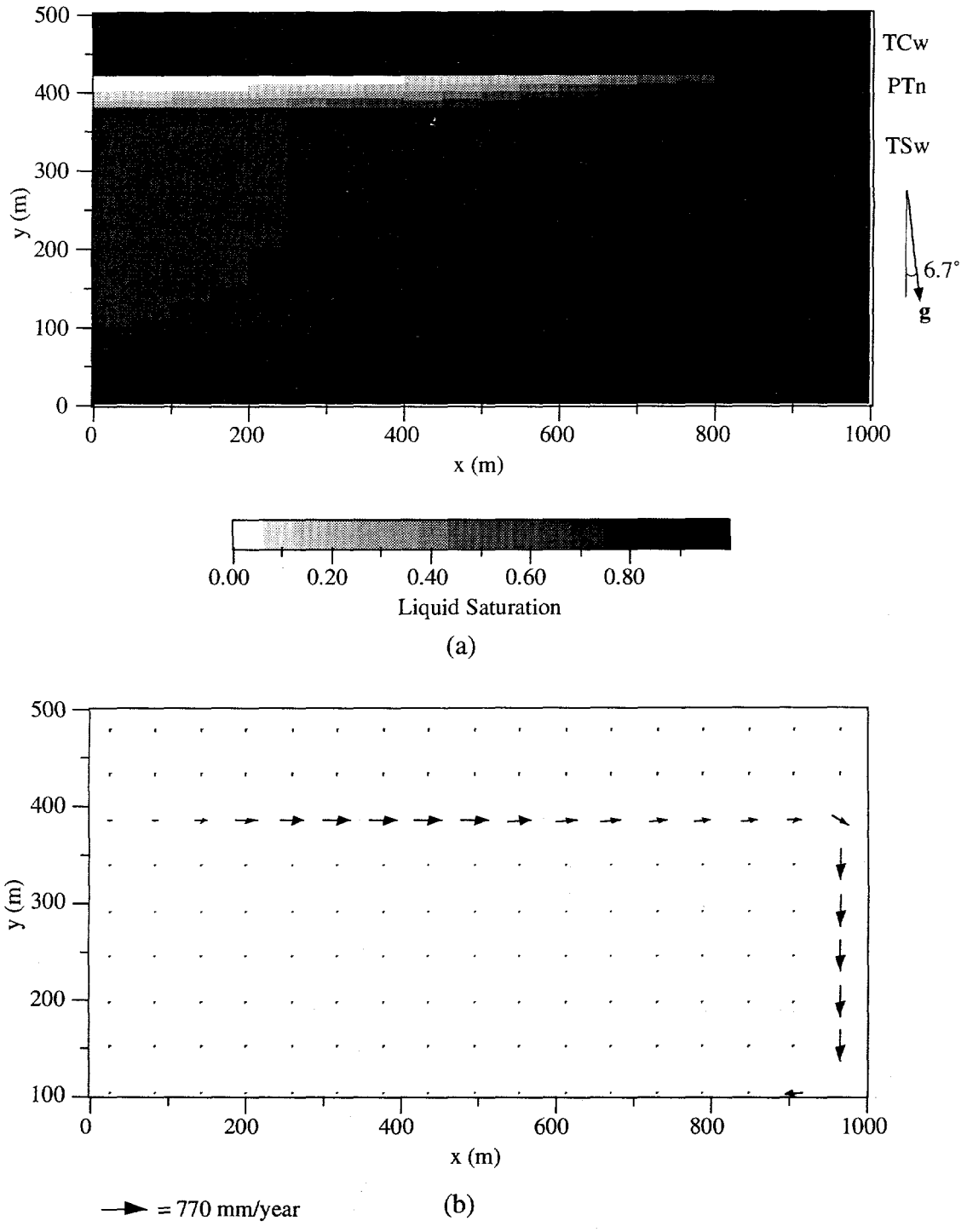

Figure 4.9. Steady-state ECM (a) saturations and (b) pore velocities as predicted by TOUGH2 for Benchmark 3 using PTn parameters from Klavetter and Peters (1986). All other parameters for TCw and TSw are taken from TSPA-93 (Wilson et al., 1994). The infiltration rate is uniform at 4.0 mm/year (Darcy velocity). Note that in order to resolve the velocity vectors in the PTn, the y-coordinate for the velocity plot starts at 100 m to eliminate the larger velocity vectors near the water table.

the PTn unit can play a significant role in the behavior of flow and lateral diversion through the PTn unit.

4.2.2 Dual Permeability Models of Benchmark 3

The previous analysis of Benchmark 2 provides insight into the behavior of the ECM and DK models for a layered one-dimensional system. In this section, a DK model of a two-dimensional layered problem (parameters given in Table 3.3) is simulated and compared to the results of the ECM presented in section 4.2.1. Only one infiltration rate (0.1 mm/year) is discussed since the results of higher infiltration rates yield results similar to those observed in the one-dimensional system. Infiltration is introduced in the fracture elements along the upper boundary.

Figure 4.10 shows the steady-state matrix saturations and pore velocities for a TOUGH2 DK simulation at an infiltration rate of 0.1 mm/year. The results are similar to the results of the ECM shown in Figure 4.3 except that more flow appears to be diverted laterally above the PTn. This phenomenon can be explained by the plot in Figure 4.11, which shows the range of saturations throughout the entire domain. The saturations appear to be similar to the ECM saturations presented in Figure 4.4, but the DK model produces lower saturations in the TCw unit. In the DK model, infiltration into the fractures along the top boundary allows flow to propagate through the fractures a finite distance before being imbibed into the matrix. This results in lower matrix saturations in the TCw, causing larger capillary pressures. The larger capillary pressures in the TCw unit in the DK model causes a greater capillary barrier effect at the top of the PTn, which diverts more flow laterally than in the ECM.

As described in Appendix B, the conductance between the fractures and matrix is uncertain due to small scale processes such as fingering and channeling that may reduce the wetted area of individual fractures and portions of fracture networks. This reduction in wetted area between the fractures and matrix may effectively reduce the conductance between fracture and matrix elements. Therefore, the fracture-matrix geometric conductance (defined here as the fracture-matrix connection area divided by the distance between the fracture and matrix elements) is reduced by two orders of magnitude. Figure 4.12 shows the steady-state matrix saturations and pore velocities for this case at an infiltration rate of 0.1 mm/year. The most pronounced effect of lowering the fracture-matrix conductance is seen in the matrix velocities above the PTn. The flow is being diverted along the top of the PTn toward the right side of the domain. Minimal downward flow occurs in the matrix of the TCw in this case. The cause is the reduced saturations in the TCw resulting from the reduced fracture-matrix conductance as shown in Figure 4.13. The flow in the TCw occurs primarily in the fractures, allowing the TCw matrix elements to sustain lower

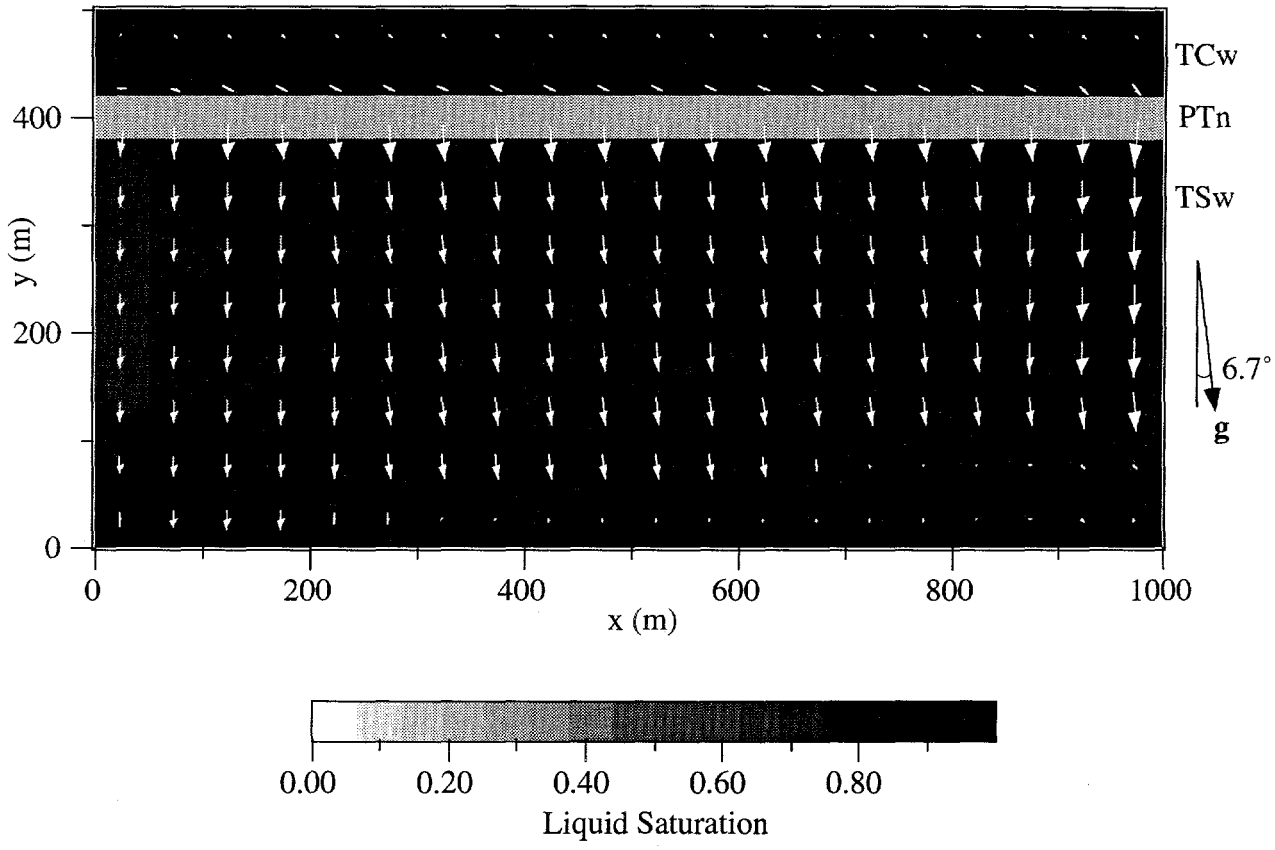

Figure 4.10. Steady-state TOUGH2 DK matrix saturations and pore velocities at a uniform infiltration rate of 0.1 mm/year (Darcy velocity). The vectors are scaled to a maximum pore velocity of 1.5 mm/year.

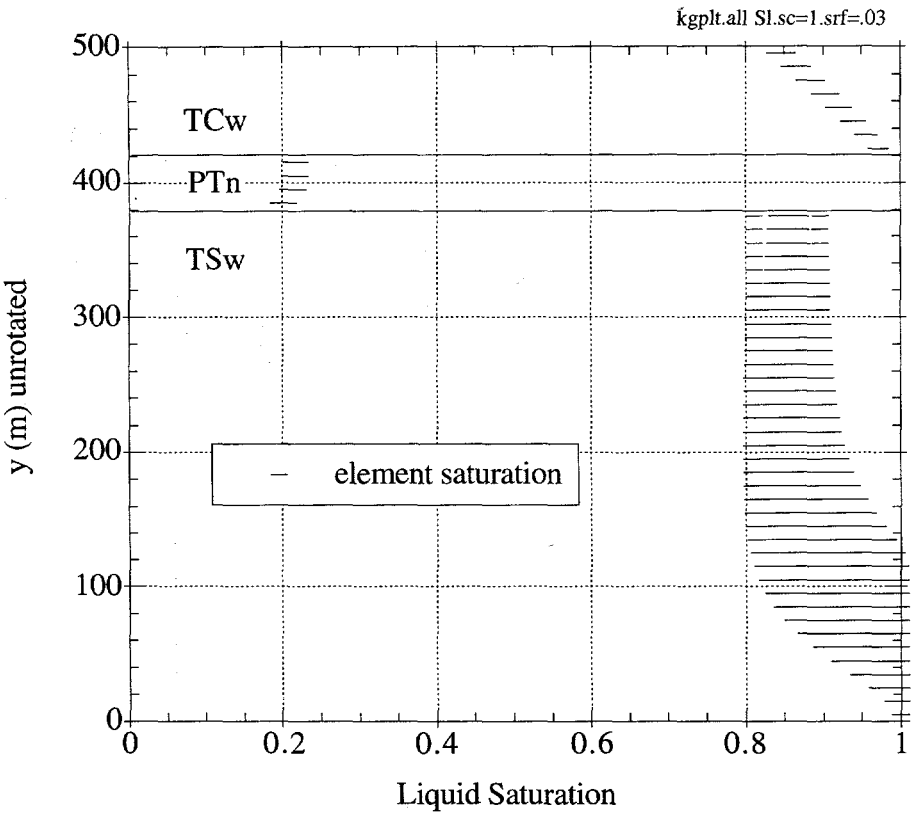

Figure 4.11. Range of matrix saturations simulated by TOUGH2 using the DK model at an infiltration rate of 0.1 mm/year for Benchmark 3. Each element's saturation is plotted as a small horizontal line so that a nearly continuous line spans the range of saturations for each row of elements.

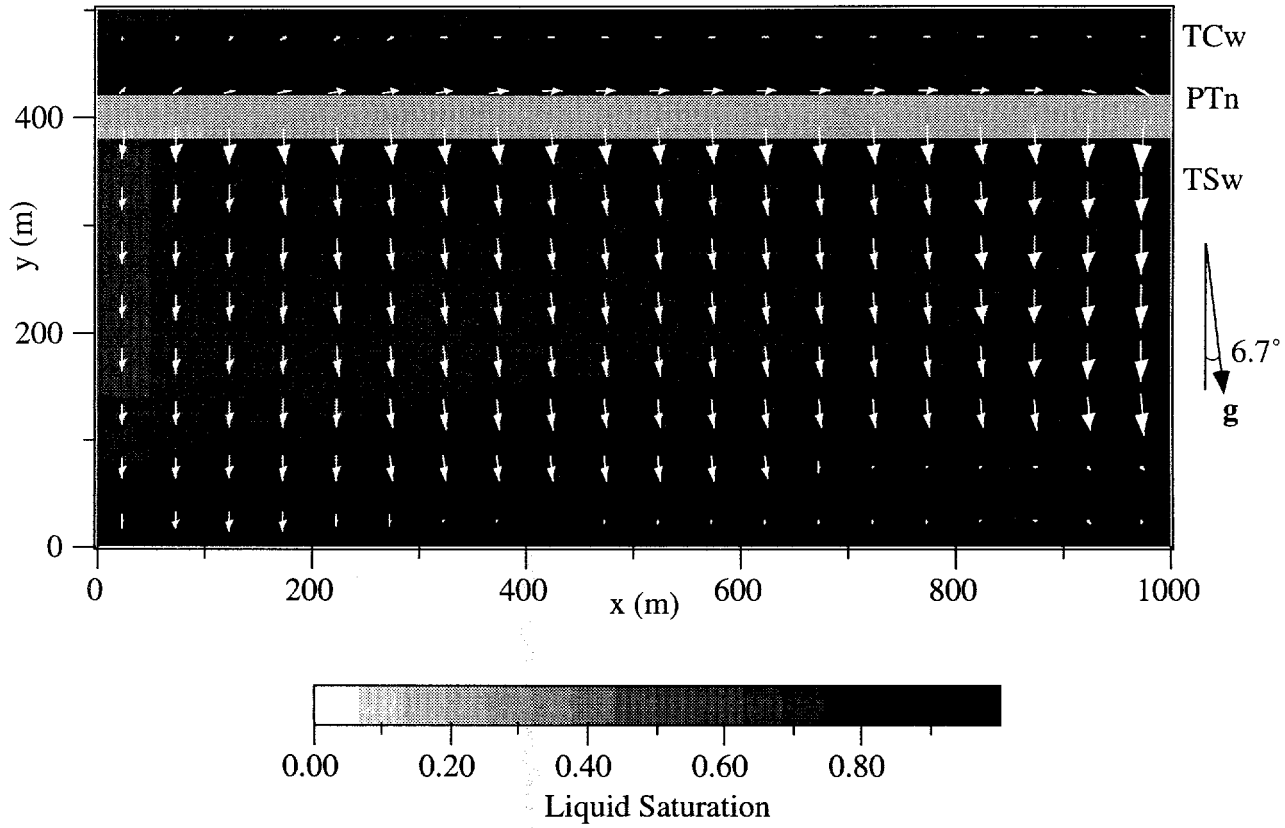

Figure 4.12. Steady-state TOUGH2 DK matrix saturations and pore velocities at a uniform infiltration rate of 0.1 mm/year (Darcy velocity). The fracture-matrix conductance has been reduced by two orders of magnitude. The vectors are scaled to a maximum pore velocity of 0.83 mm/year.

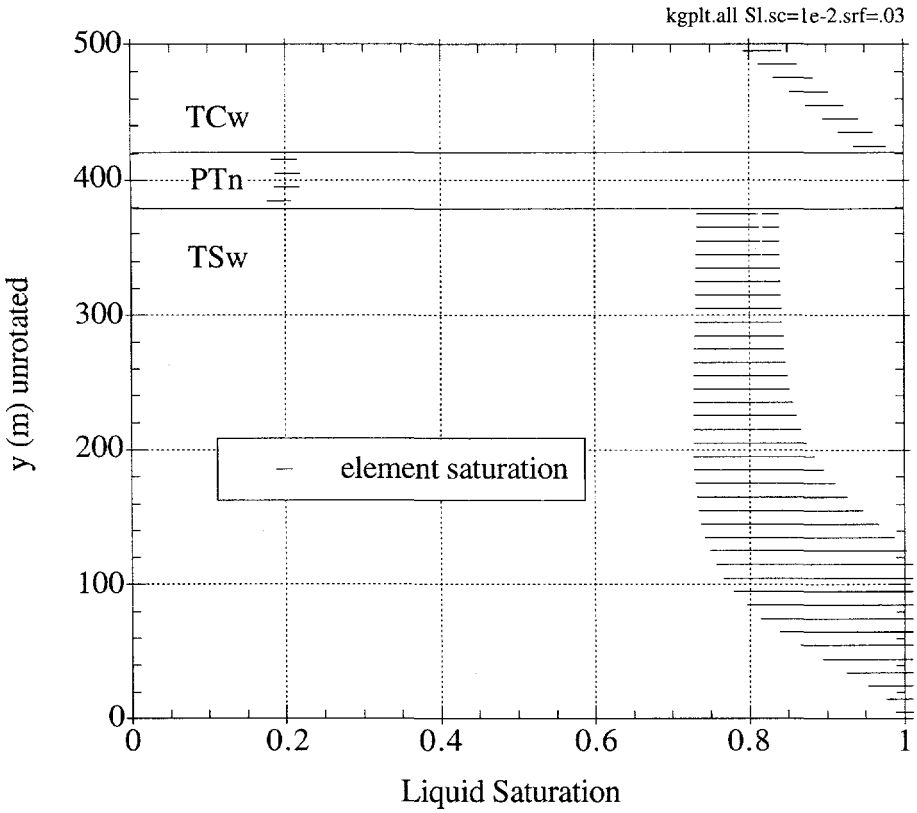

Figure 4.13. Range of matrix saturations simulated by TOUGH2 using the DK model at an infiltration rate of 0.1 mm/year for Benchmark 3. The fracture-matrix conductance was reduced by two orders of magnitude in this simulation. Each element's saturation is plotted as a small horizontal line so that a nearly continuous line spans the range of saturations for each row of elements.

saturations and flow. This creates larger capillary pressures in the TCw matrix elements and a greater capillary barrier effect at the TCw-PTn interface. Once flow reaches the PTn, much of it is imbibed into the matrix as evidenced by the larger velocities in the PTn matrix shown in Figure 4.12. However, similar to the results presented for Benchmark 2, the flow velocities in the fractures have increased to the same order of magnitude as the matrix velocities throughout the entire domain at this reduced fracture-matrix conductance.

4.2.3 Effects of Local Infiltration

In the previous analyses, a uniform infiltration has been applied along the entire length of the top boundary. This section investigates the effects of applying a localized source of infiltration along just one element of the top boundary. The TOUGH2 single-phase DK model is used with a localized infiltration rate of 2.0 mm/year applied to a single element located at x=175 meters along the top boundary. Because the domain consists of 20 elements in the x-direction, this local infiltration rate is equivalent to an infiltration rate of 0.1 mm/year applied uniformly to all the elements along the top boundary.

Figure 4.14 shows the steady-state matrix saturations and pore velocities for the local infiltration case. A considerable amount of downward flow occurs just beneath the source of infiltration at x=175 meters. Further away from the infiltration source, a considerable amount of lateral diversion occurs in the matrix of the TCw as a result of lower matrix saturations. The lowest saturations appear to exist near x=700 meters, which is sufficiently far from both the infiltration source towards the left and the no-flow boundary at the right where laterally diverted flow accumulates. Figure 4.15 shows the matrix saturation of each element in the domain, providing a complete range of steady-state matrix saturations. In the local infiltration case, the range of saturations is much larger than in the uniform infiltration case. Saturations just below the PTn range from a low of 0.5 (x≈700 m) to a high of 1.0 (underneath the source at x=175 m). This contrasts with the much narrower range (0.8–0.9) shown in Figure 4.11 for a uniform infiltration along the top boundary.

4.3 FEHMN Results for Benchmark 3

In the previous analysis using TOUGH2, the dipping layers were simulated by rotating the gravity vector within the uniform, orthogonal domain shown in Figure 4.1. The gravity vector cannot be rotated in FEHMN, so the dipping layers are simulated explicitly as shown in Figure 4.16. The dimensions of the domain are the same as those used in the TOUGH2 analyses, but the

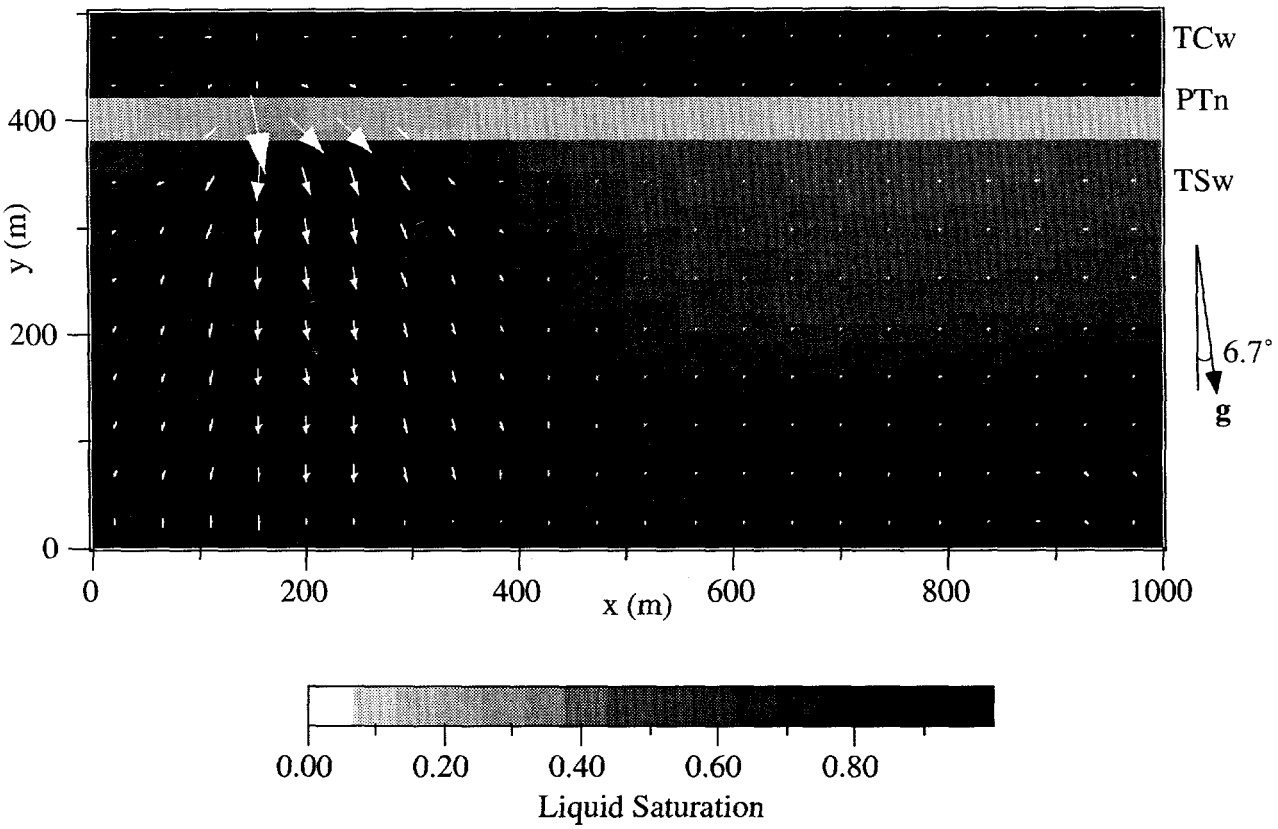

Figure 4.14. Steady-state TOUGH2 DK matrix saturations and pore velocities using a local infiltration rate of 2.0 mm/year (Darcy velocity) at one element (x=175 m). The vectors are scaled to a maximum pore velocity of 11.5 mm/year.

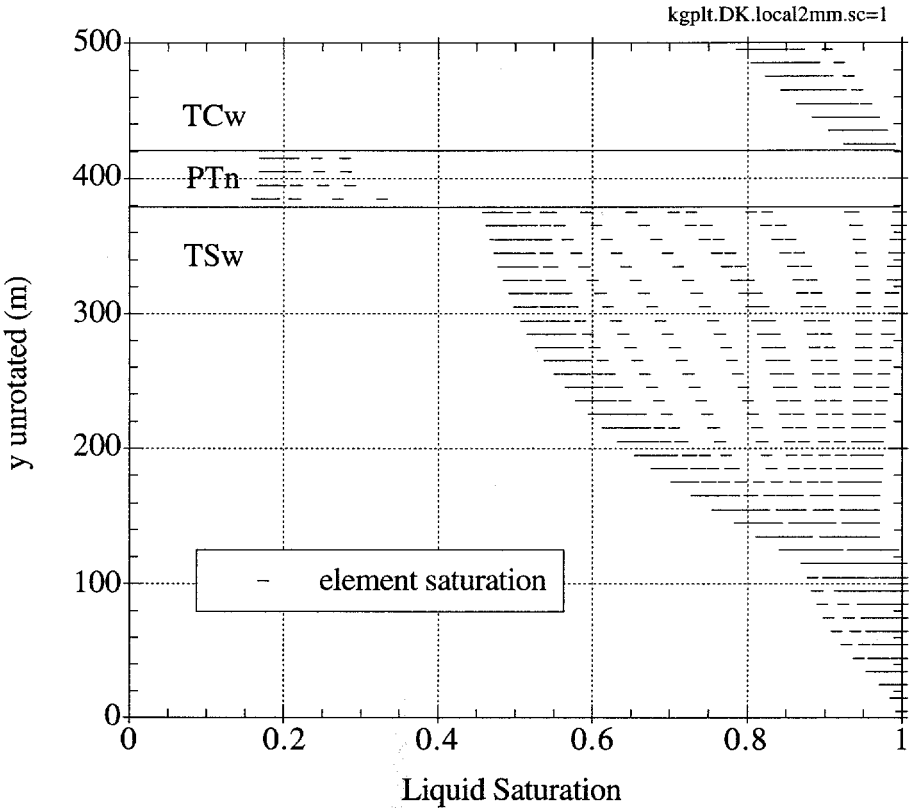

Figure 4.15. Range of matrix saturations simulated by TOUGH2 using the DK model at a localized infiltration rate of 2.0 mm/year at one element (x=175 m) for Benchmark 3. Each element's saturation is plotted as a small horizontal line to span the entire range of saturations for each row of elements.

elements are not orthogonal to the dipping layers. Each node of each element is assigned material properties (Table 3.2) corresponding to one of the three layers depending on the location of the node. As a result, the interfaces of the three units are simulated by a 'stair-stepped' property distribution. A steady-infiltration rate of 0.1 mm/year is applied to the top boundary, and the bottom boundary is saturated.

Figure 4.17 shows the steady-state saturation and velocity distributions for an infiltration rate of 0.1 mm/year using the ECM in FEHMN. The saturations are seen to be lower in the non-welded PTn unit and higher in the welded TCw and TSw units. The saturations also appear to be slightly higher towards the left and right sides of the domain. Figure 4.18 shows a plot of the liquid saturations along horizontal transects through the TCw and TSw units which confirms that the saturations are indeed higher on the left and right sides of the domain. Lateral diversion of flow would explain the higher saturation on the right (down-dip) side of the domain, but the cause of the higher saturations along the left side is unclear. The velocities shown in Figure 4.17 are directed predominantly in the direction of gravity, which is consistent with the results of TOUGH2.

Figure 4.19 shows a plot of the entire range of steady-state saturations at each location above the water table. By plotting all the saturations of each node as a function of location above the water table, a range of saturations can be observed for each unit. The results of the TOUGH2 ECM simulation described in the previous section are also shown.† The range of saturations in the PTn unit are nearly identical for both FEHMN and TOUGH2. The average saturation in the welded TCw and TSw are also similar. The range of saturations in the welded units are different in the FEHMN and TOUGH2 simulations, but this can be attributed to the different spatial discretizations used in FEHMN (Figure 4.16) and TOUGH2 (Figure 4.1). A wider range of saturations would be expected in the TOUGH2 simulations since the gravity vector is not parallel to the lateral boundaries.

4.4 Summary

Benchmark 3 has investigated infiltration into a two-dimensional layered domain with a 6.7° dip. Results have shown that capillary diversion of flow can occur at the interfaces of different materials. Under unsaturated conditions (≤ 0.1 mm/year), the capillary diversion occurred at the top of the PTn. The saturations in the TCw were low enough to create a significantly large

† The y-coordinates for TOUGH2 in Figure 4.18 have been derived from a rotation transformation of 6.7° to obtain a consistent coordinate system with FEHMN.

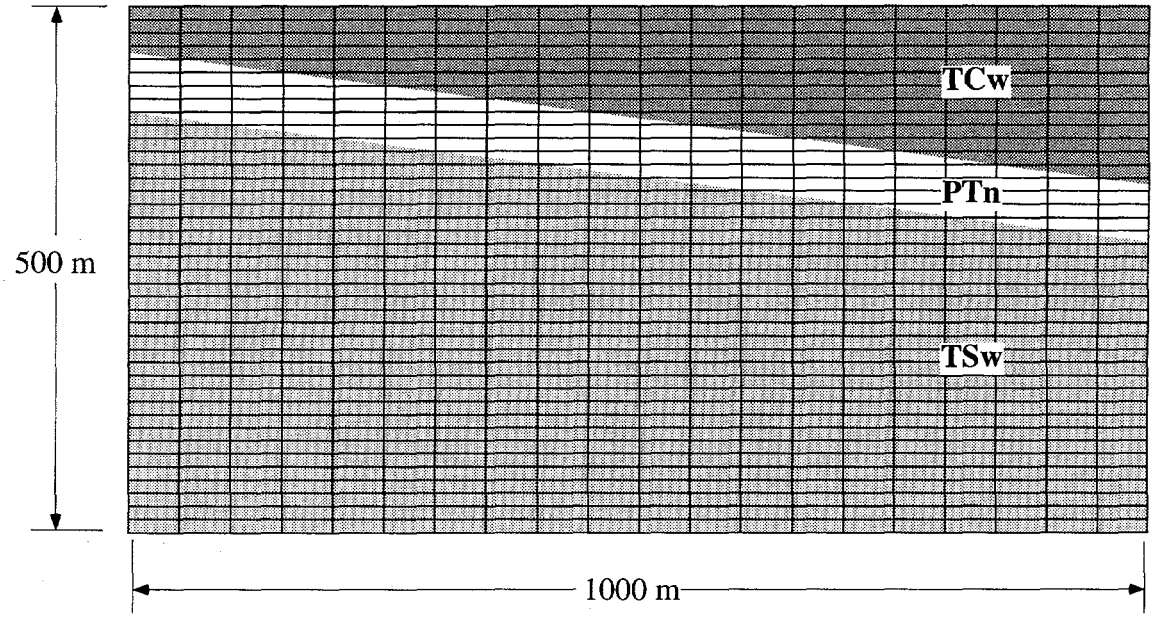

Figure 4.16. Benchmark 3 domain for FEHMN numerical simulations. The nodes of each quadrilateral element are assigned properties corresponding to one of the three layers depending on the location of the node. This results in a stair-stepped property distribution at the unit interfaces. The bottom boundary is saturated and infiltration is applied along the top boundary. No-flux conditions exist at the lateral boundaries.

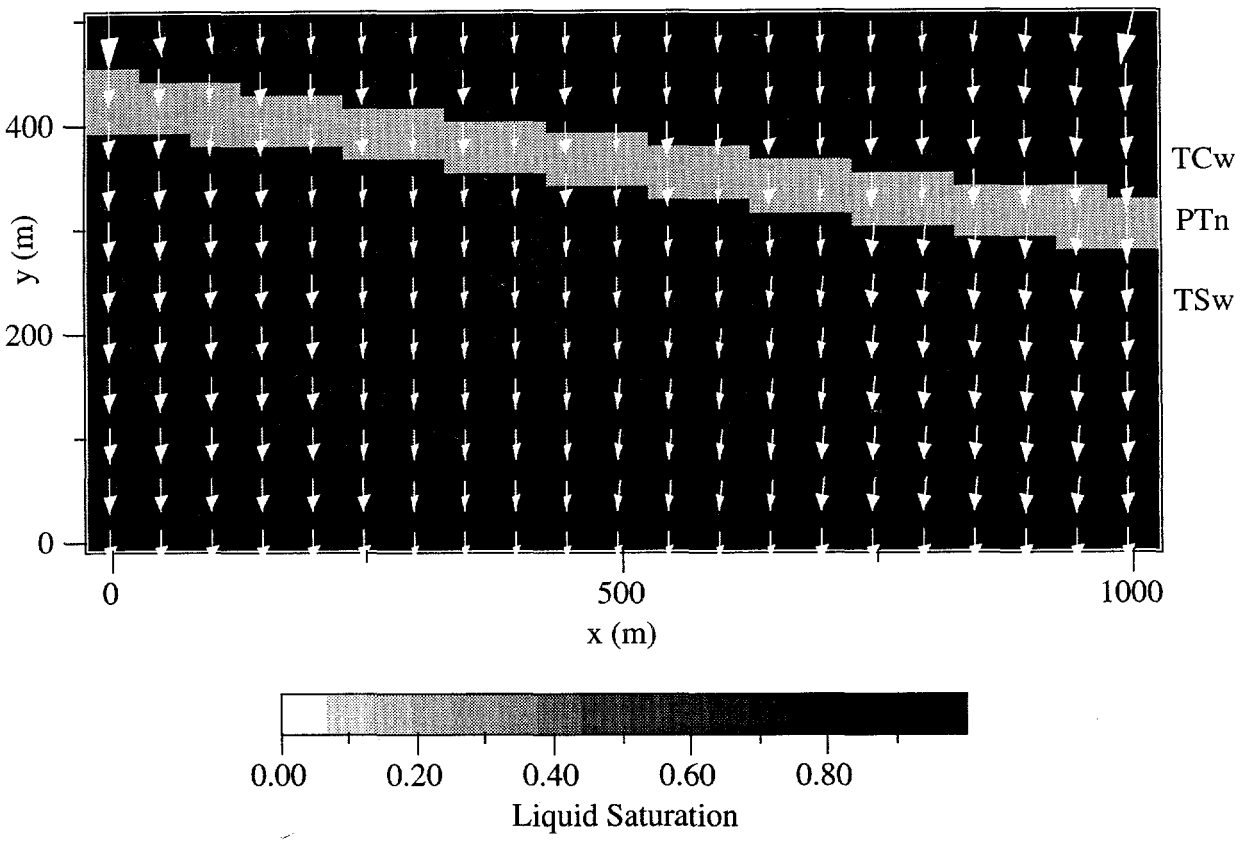

Figure 4.17. Steady-state ECM saturations and pore velocities predicted by FEHMN for Benchmark 3. The infiltration rate is uniform at 0.1 mm/year, and the bottom boundary is saturated. The velocity vectors are scaled to a maximum pore velocity of 0.2 mm/year.

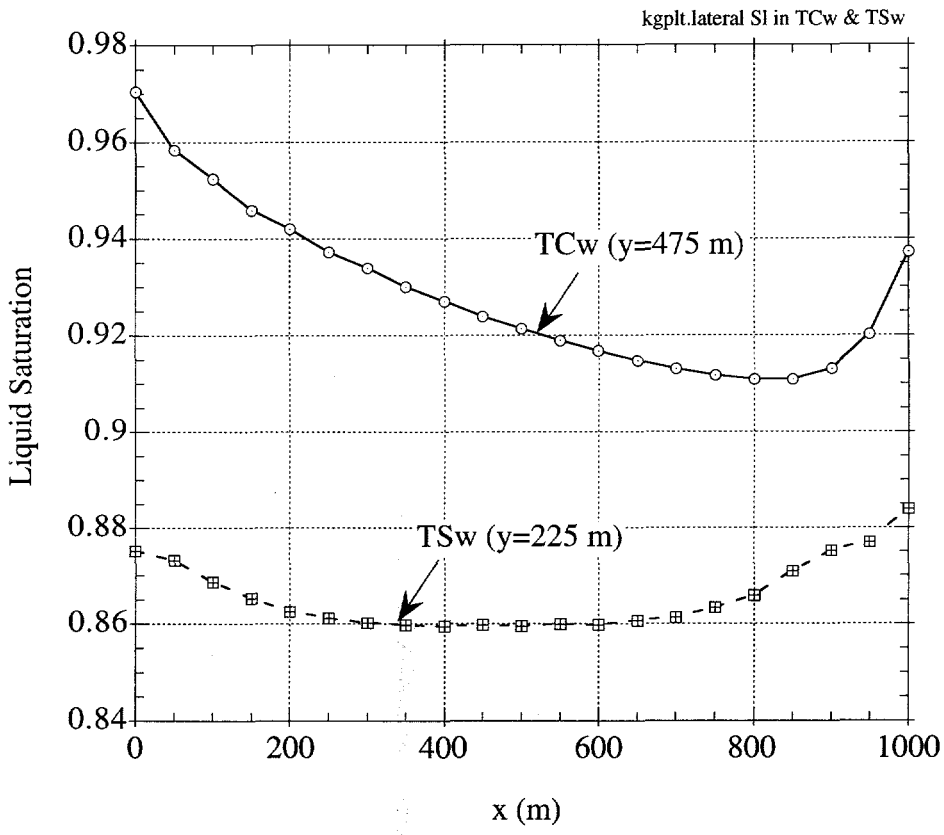

Figure 4.18. Steady-state ECM saturations along horizontal transects through the TCw (y=475 m) and TSw (y=225 m) units as predicted by FEHMN. The infiltration rate was uniform at 0.1 mm/year and the bottom boundary was saturated.

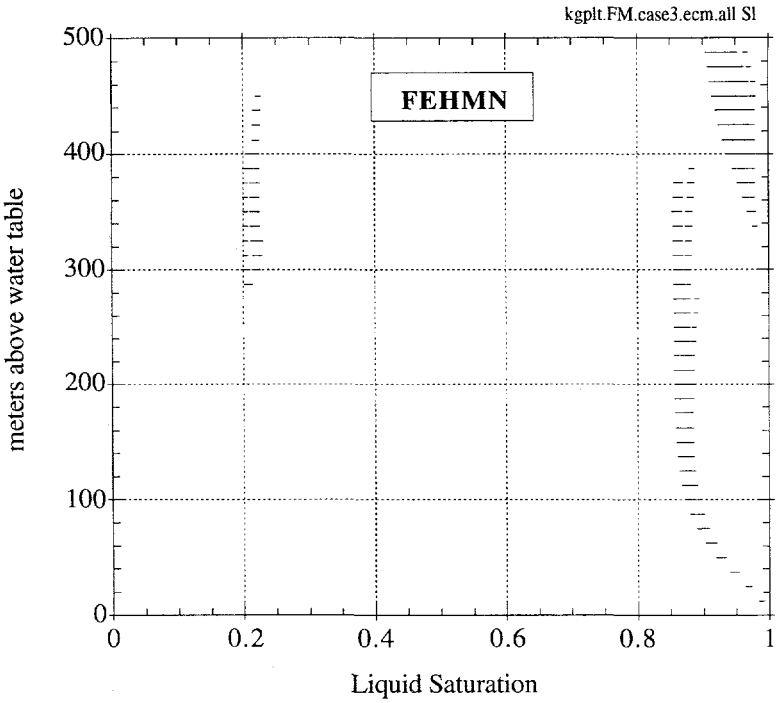

(a)

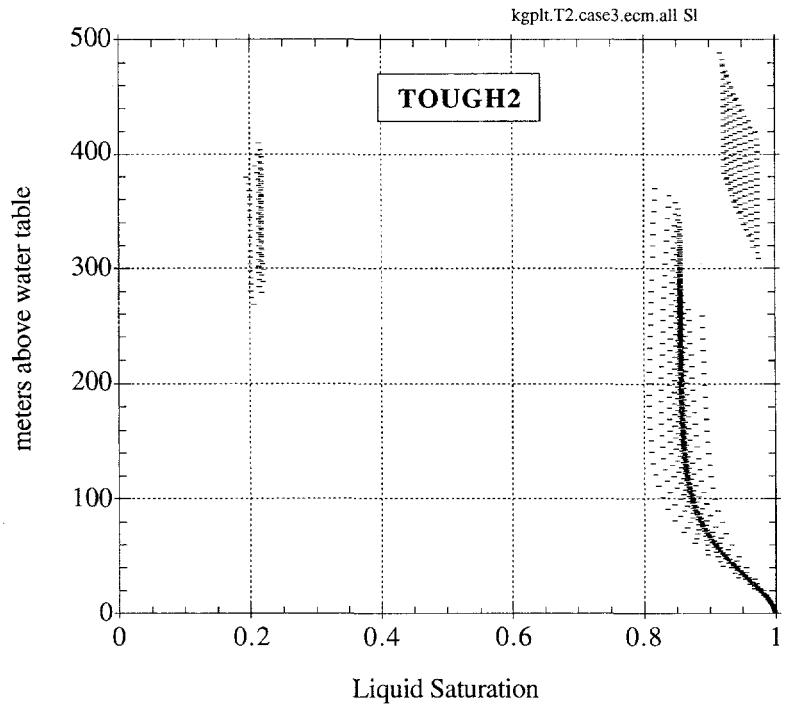

(b)

Figure 4.19. Range of steady-state ECM saturations for Benchmark 3 using a) FEHMN and b) TOUGH2. The infiltration rate is uniform at 0.1 mm/year and the saturations are referenced to elevation above the water table. Each element's saturation is plotted as a small horizontal line to span the range of saturations at a given elevation.

capillary pressure difference between the elements in the TCw and the elements below in the PTn. For higher infiltration rates (≥1.0 mm/year), the welded TCw and TSw units were nearly saturated and maintained low capillary pressures as opposed to the unsaturated PTn unit, which maintained higher capillary pressures. As a result, flow through the unsaturated PTn experienced a capillary diversion at the PTn-TSw interface. For the unsaturated conditions similar to Yucca Mountain, capillary barriers and diversions are likely to occur when a lower porosity material overlies a higher porosity material (such as the base of the TCw), creating a capillary pressure difference described above for the low infiltration rate. Poor contacts and fractures may also contribute to capillary diversions in unsaturated flows.

Results also show that the two-phase parameters used for the PTn matrix can play a significant role in the behavior of flow and lateral diversion in the PTn unit. Using PTn parameters obtained from Klavetter and Peters (1986) given in Table 3.1, significantly more lateral diversion through the PTn unit was observed at an infiltration rate of 4 mm/year than the same simulation using TSPA-93 parameters given in Table 3.2. The discrepancies are suspected to depend strongly on the different van Genuchten matrix parameters used in each data set.

The use of the DK model produced results similar to those presented for the one-dimensional system in Benchmark 2. Propagation of flow through the fractures in the TCw unit caused lower matrix saturations in the TCw and, hence, greater capillary diversions above the PTn. When the fracture-matrix geometric conductance was reduced by two orders of magnitude, the matrix saturations were reduced everywhere as a result of greater fracture flow throughout the entire domain.

The use of a localized source of infiltration produced a greater range of saturations throughout the two-dimensional domain. Matrix saturations were higher directly beneath the infiltration source, but further away from the infiltration source, the matrix saturations were greatly reduced. As a result, flow was primarily directed downwards beneath the infiltration source, but a significant amount of lateral diversion occurred in the TCw away from the source.

Finally, comparisons between FEHMN and TOUGH2 using the ECM showed that similar results were obtained. Although the domains were modeled differently in the two codes, the overall saturation and velocity distributions were comparable.

Chapter

FIVE

Benchmark 4: Heterogeneous 2-D Infiltration

This chapter examines the capabilities of DUAL and TOUGH2 to model infiltration into a completely heterogeneous, unsaturated field using the equivalent continuum model (ECM) and the dual permeability (DK) model. Matrix porosities are stochastically simulated over a two-dimensional domain representing the welded TSw unit of Yucca Mountain. All other fracture and matrix hydrologic properties are derived from the simulated porosities, resulting in a completely heterogeneous domain represented by hundreds of different materials in the numerical model†. The heterogeneities are included as a possible means to focus flow and create fast flow paths through a fractured tuffaceous rock.

The first part of this chapter focuses on the problem domain—the stochastically simulated matrix porosity distribution and the subsequent averaging of all hydrologic properties on the computational flow scale. Comparisons are then made between the steady-state results of DUAL and TOUGH2 for constant infiltration rates. TOUGH2 is then used to compare and assess the ECM and DK models for a ponded boundary condition at the top of the domain.

5.1 Description of Benchmark 4

A heterogeneous matrix porosity field representative of the TSw hydrostratigraphic unit is generated using a geostatistical simulation method for Benchmark 4. The heterogeneous field is produced by unconditional sequential Gaussian simulation with a range of 100 m in the horizontal direction and a horizontal to vertical anisotropy of spatial correlation of 4:1. The standard normal distribution generated by the sequential Gaussian method is then transformed to a beta distribution

† The material dimensions in TOUGH2 were increased from 27 to 2007 for this problem. Due to the authors' unfamiliarity with the structure of the material arrays in FEHMN, FEHMN was not used in this problem.

with a mean porosity of 0.132 as defined by the beta distribution parameters for the TSw unit given in Arnold et al. (1995). The individual values of matrix porosity are simulated at the geostatistical scale with elements that are 1 m high x 8.5 m wide as shown in Figure 5.1. Since nearly 60,000 geostatistical elements are used to represent the 500 m high x 1000 m wide problem domain, the geostatistical matrix porosities are averaged into larger elements that are then used in the flow simulations. A total of 20 elements in the horizontal direction and 40 elements in the vertical direction is used in the flow simulations using DUAL and TOUGH2. Different methodologies are used to assign hydrologic parameters to each of the 800 elements in DUAL and TOUGH2 because specific pre-processing and upscaling methods previously designed for DUAL's finite element formulation (Arnold et al. (1995) were not readily compatible with TOUGH2. The different methods that are used are discussed in the next two sections.

5.1.1 Hydrologic Parameter Derivation in DUAL

Hydraulic parameters used in DUAL are derived from matrix porosity as described in Arnold et al. (1995). Saturated matrix hydraulic conductivity is calculated by linear regression of ln K_{sat} with porosity, including a random error term to account for uncertainty in the regression relationship. Matrix moisture retention relationships are modeled using the incomplete gamma function and the relative permeability curves are based on the Brooks-Corey model (1966). Saturated hydraulic conductivity and porosity of fractures are determined from regression relationships with matrix porosity. Constant values of the incomplete gamma function parameters and the Brooks-Corey constant are used for the fracture continuum.

An adaptive gridding procedure is applied to generate the finite-element mesh used in the groundwater flow simulation. Adaptation of the mesh is based on minimizing the variance of matrix porosity within each quadrilateral element. Adaptation is accomplished by adjusting the nodal locations in the mesh using an automated method. Following adaptation of the grid, effective hydraulic properties for each element are determined by upscaling the properties from the underlying geostatistical scale. Arithmetic averaging is used to upscale porosity, and saturated hydraulic conductivity is geometrically averaged. A more complete discussion of adaptive gridding and upscaling is presented in Arnold et al. (1995). The adapted grid is shown superimposed on top of the averaged porosities in Figure 5.2.

5.1.2 Hydrologic Parameter Derivation in TOUGH2

The hydrologic matrix parameters used in TOUGH2 are obtained using regressions based on TSPA-93 (Wilson et al., 1994). The regressions use the expected parameter values from entropy

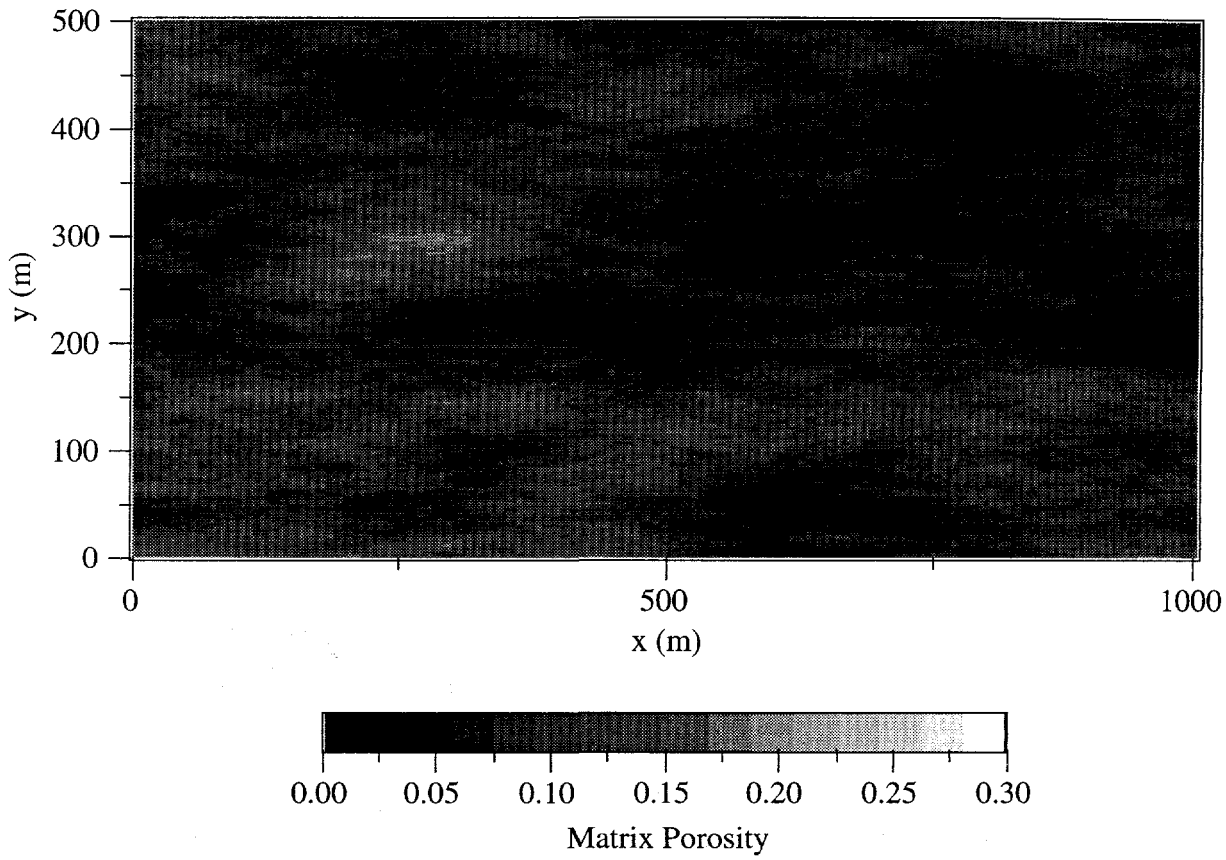

Figure 5.1. Geostatistical simulation of matrix porosities used in Benchmark 4.

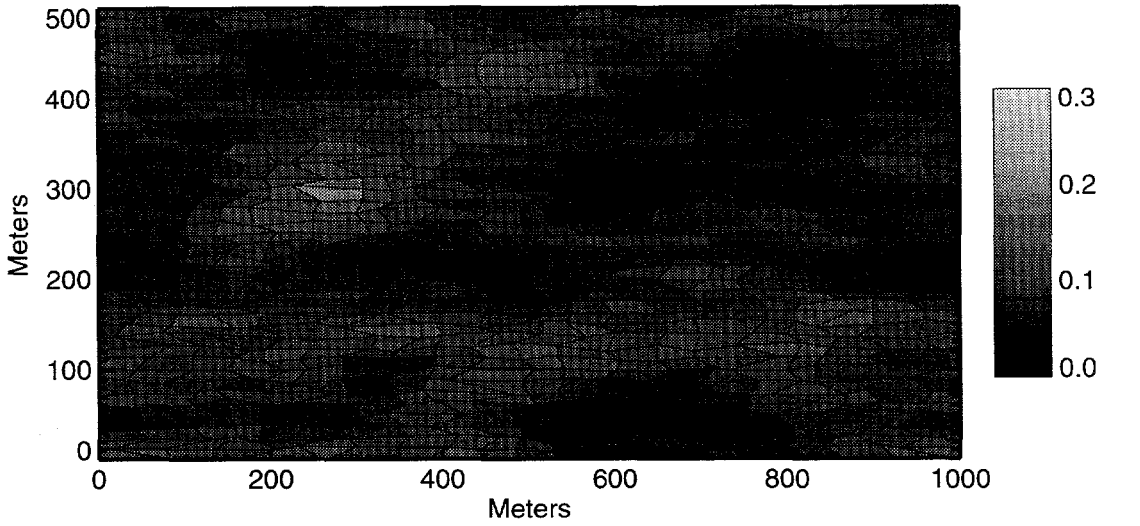

(a) DUAL

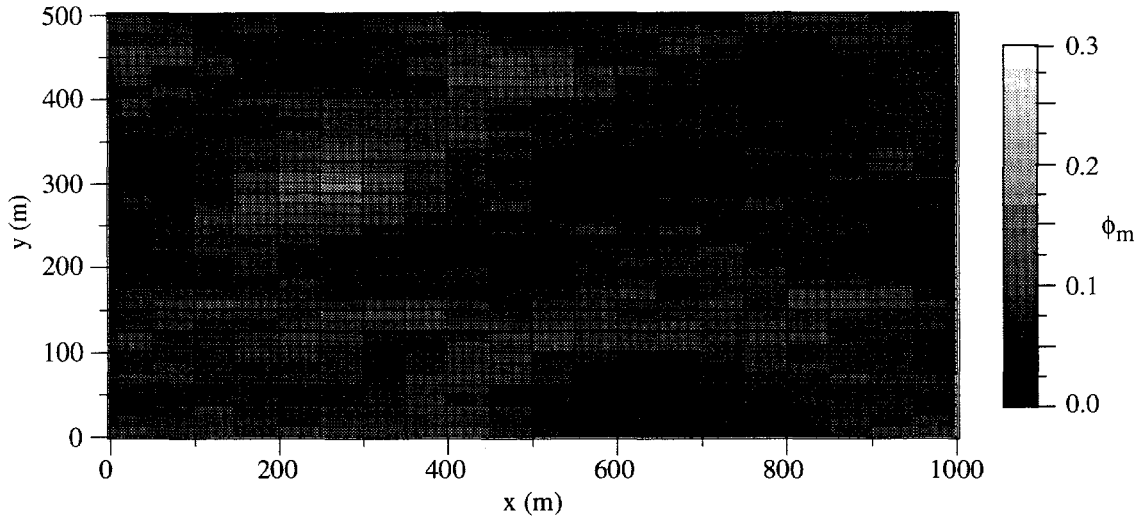

(b) TOUGH2

Figure 5.2. Computational grids and averaged matrix porosities used in a) DUAL and b) TOUGH2 for Benchmark 4.

fits of data collected for each unit and are shown in Figure 5.3. The saturated matrix conductivity, K_{sat}, is correlated to the matrix porosity, and $\log(\alpha)$ is correlated to $\log(K_{sat})$. The van Genuchten β parameter is assumed constant for the matrix elements as a result of the relatively small variance associated with the expected porosities of each unit as shown in Figure 5.3. The fracture porosity (calculated as the expected fracture aperture divided by the fracture spacing for each unit) is obtained through a regression with the matrix porosity as shown in Figure 5.4. The physical basis for the fracture porosity regression is the general trend that highly welded matrix units that have low porosities are more highly fractured and, hence, contain higher fracture porosities. The fracture spacing and van Genuchten β parameter are assumed constant and taken from Table 3.2 for the TSw unit. The van Genuchten α parameter is derived from the Young-Laplace equation (Bear, 1972) assuming planar fractures as shown in Figure 5.4. Finally, the intrinsic fracture permeability is assumed to be equal to the square of the aperture divided by 12 (derived from Poiseuille flow between parallel planes). The continuum fracture permeability is calculated as the intrinsic permeability multiplied by the fracture porosity (aperture/spacing).

An orthogonal grid comprised of 40 elements in the vertical direction and 20 elements in the horizontal direction is used in TOUGH2 for the flow simulations. The matrix and fracture porosities on the geostatistical scale are arithmetically averaged to generate a porosity corresponding to each element on the flow simulation scale. The fracture α parameter was also upscaled arithmetically from the geostatistical scale[†] . The permeabilities for both the matrix and fractures were geometrically averaged to the flow scale. The mesh, superimposed on the averaged matrix porosities, is shown in Figure 5.2 with the corresponding DUAL mesh. It should be noted that the original dimension specification for the number of different materials in TOUGH2 was 27. This dimension was increased to 2007 for this problem.

5.2 Comparison Between DUAL and TOUGH2

Both models were tested against Benchmark 4 using the equivalent continuum model formulation. The original intent was to specify a constant infiltration of 0.1 mm/year along the top boundary and obtain steady-state saturation profiles for comparison. However, the DUAL code was unable to converge to a steady-state solution using the specified flux upper boundary condition. Instead, the capillary pressure was specified along the top boundary of the DUAL model. Because each element consisted of a different moisture retention curve, the specified capillary pressures resulted in different specified saturations, which caused non-uniform infiltration

[†] It may have been more appropriate to calculate the fracture α parameter after the fracture porosities had already been upscaled.

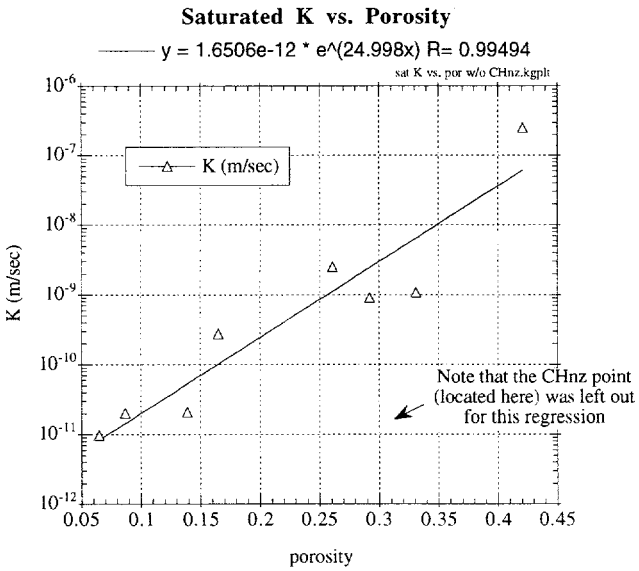

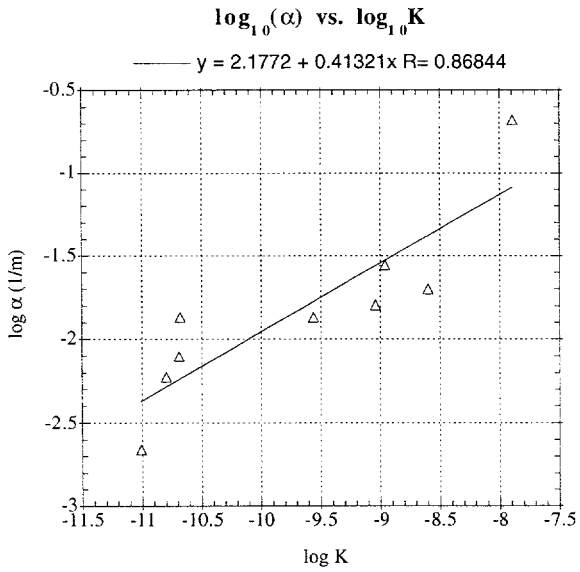

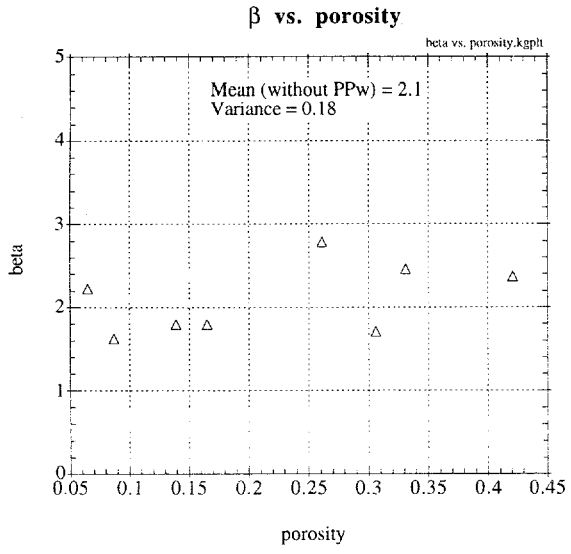

Figure 5.3. Correlation of unsaturated matrix parameters. Each point in the figures represents the expected value from an entropy curve fit of multiple samples taken from a particular unit. These values were given in TSPA-93 (Wilson et al., 1994).

Fig 5.3 unsat matx correlations

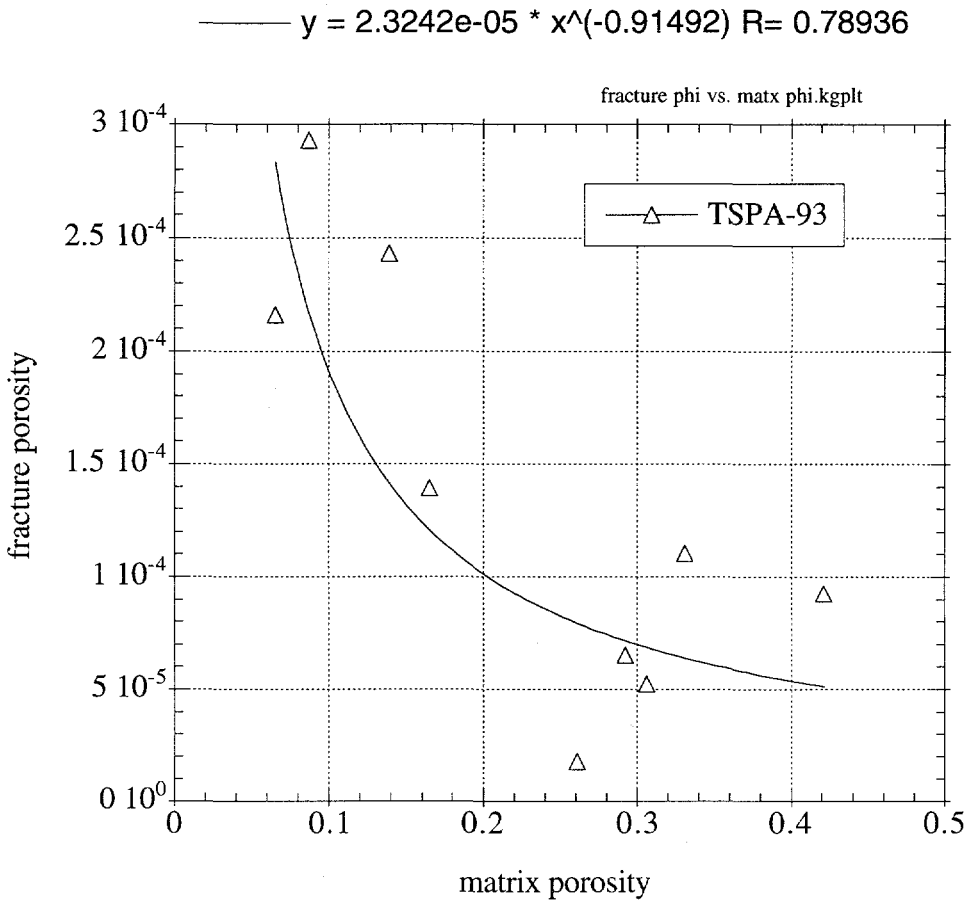

(a)

$$\alpha_f = \frac{1}{P_c} = \frac{1}{\sigma\left(\frac{1}{r_1} + \frac{1}{r_2}\right)}$$

$r_1 = \frac{b}{2}$ *and* $r_2 \to \infty$ (*plane fracture*)

$$\Rightarrow \alpha_f = \frac{b}{2\sigma}$$

where $\sigma \equiv$ *surface tension of water*

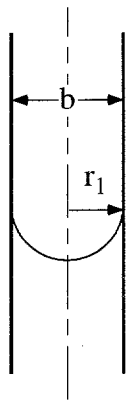

(b)

Figure 5.4. a) Correlation between fracture and matrix porosities. The fracture porosities were calculated as the fracture aperture divided by the fracture spacing given in TSPA-93 (Wilson et al., 1994). b) Derivation of the van Genuchten α parameter for a fracture plane using the Young-Laplace equation (Bear, 1972).

along the top boundary. Nevertheless, the specified capillary pressure at the top boundary resulted in a steady-state global infiltration of 0.065 mm/year in DUAL. This infiltration rate was used in TOUGH2 for comparison.

Figure 5.5 shows the steady-state matrix saturations resulting from DUAL and TOUGH2 for an average infiltration rate of 0.065 mm/year (constant pressure boundaries were specified in DUAL which resulted in an average infiltration rate of 0.065 mm/year). Both codes show similar trends in the saturation field—regions of lower saturation correspond to regions of higher porosity as shown in Figure 5.2. However, the saturations resulting from DUAL are generally lower than those resulting from TOUGH2. Although this discrepancy is consistent with results from the previous benchmarks in this report, the hydrologic parameters used in DUAL and TOUGH2 are not identical as a result of the different regressions that are used to derive effective hydraulic properties of individual elements for the two codes. Therefore, identical results are not expected to occur. Overall, both codes appear capable of handling flow through very heterogeneous systems. A note should be made regarding the role of the fractures in this problem. Since the infiltration rate was well below the saturated conductivity of the matrix unit, nearly all of the flow was contained in the matrix, and the fractures played a minimal role in the steady-state results. In the next section, a ponded condition is applied to several elements along the top boundary to examine the possibility of fast flow through the fractures and the effects of heterogeneity on the results.

5.3 ECM vs. DK Models Using Benchmark 4

In this section, the ECM and DK single-phase models are assessed using Benchmark 4 and a high infiltration condition. Table 3.3 gives the formulation used to calculate DK parameters such as fracture-matrix connection area. All other parameters remain the same, but instead of a constant infiltration along the top boundary, a ponded condition is applied to several elements. Six elements along the top rows of both the fracture and matrix domains between x=350 m and x=650 m are connected to a saturated upper boundary after hydrostatic conditions are established. The hydrostatic saturation distribution for the fracture and matrix domain resulting from a specified water table along the bottom boundary is shown in Figure 5.6. The fractures are essentially dry, and the matrix saturations range from near one at the bottom to near 0.4 at the top.

The matrix and fracture saturations resulting from one day of ponding in the ECM model are shown in Figure 5.7[†] . Increases in the saturations over the hydrostatic conditions are only evident locally near the saturated top boundary. This behavior is a result of the ECM model, which

[†] The matrix and fracture saturations can be back-calculated from the composite capillary pressure distribution in the ECM model using separate characteristic curves for the matrix and fractures.

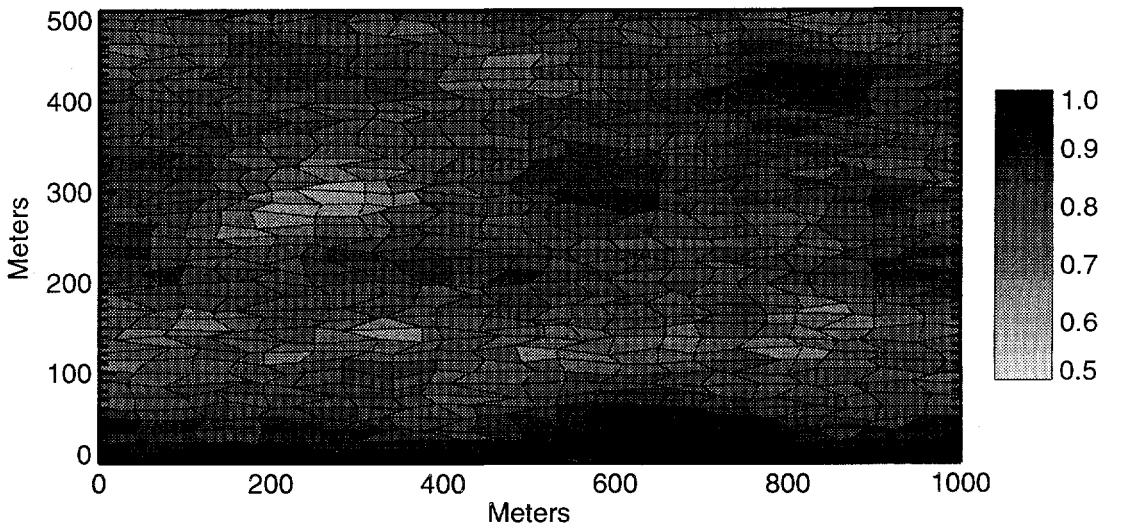

(a) DUAL

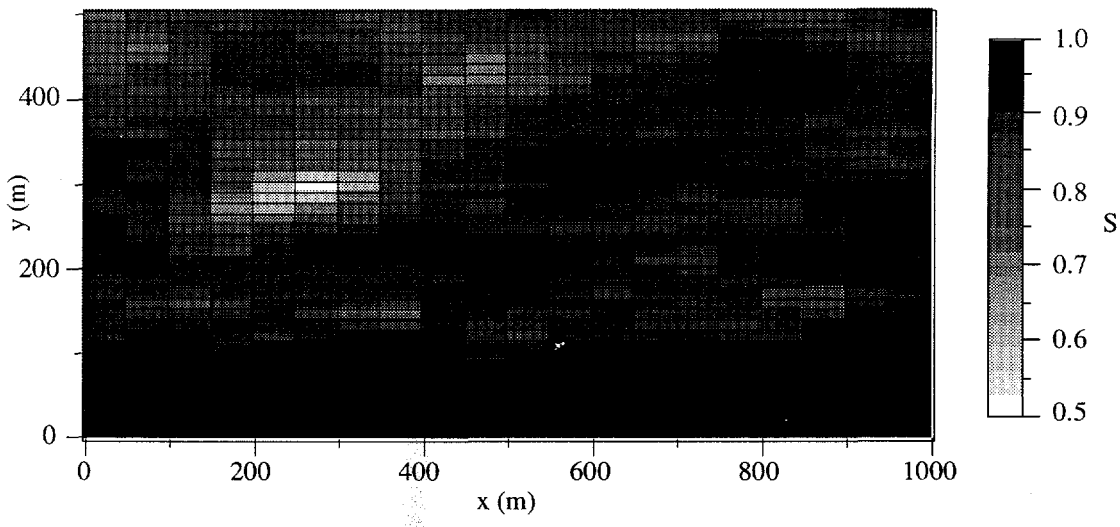

(b) TOUGH2

Figure 5.5. Steady-state ECM matrix saturations using an infiltration rate of 0.065 mm/year for a) DUAL and b) TOUGH2 in Benchmark 4. Note that the saturation scales are slightly different for the two simulations.

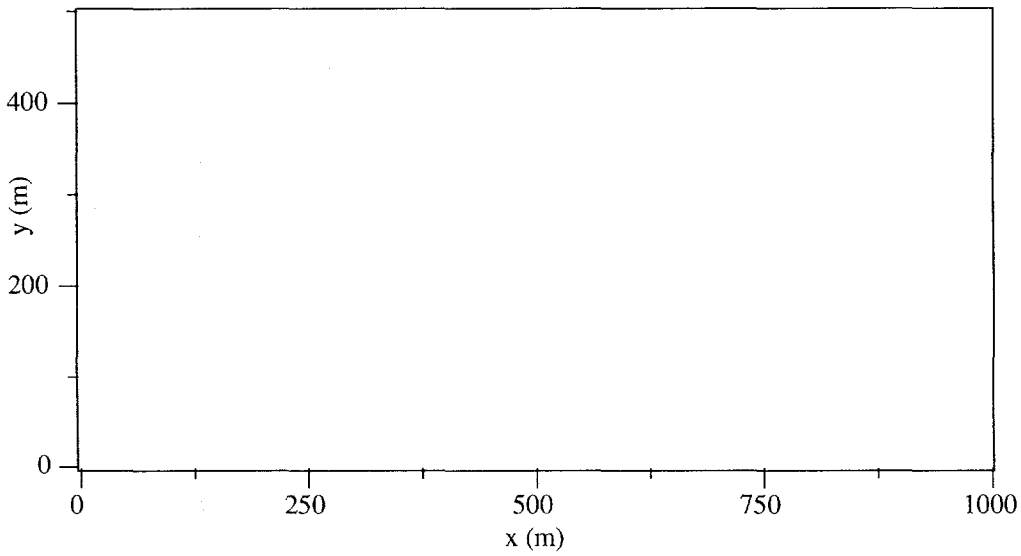

(a) fracture saturation

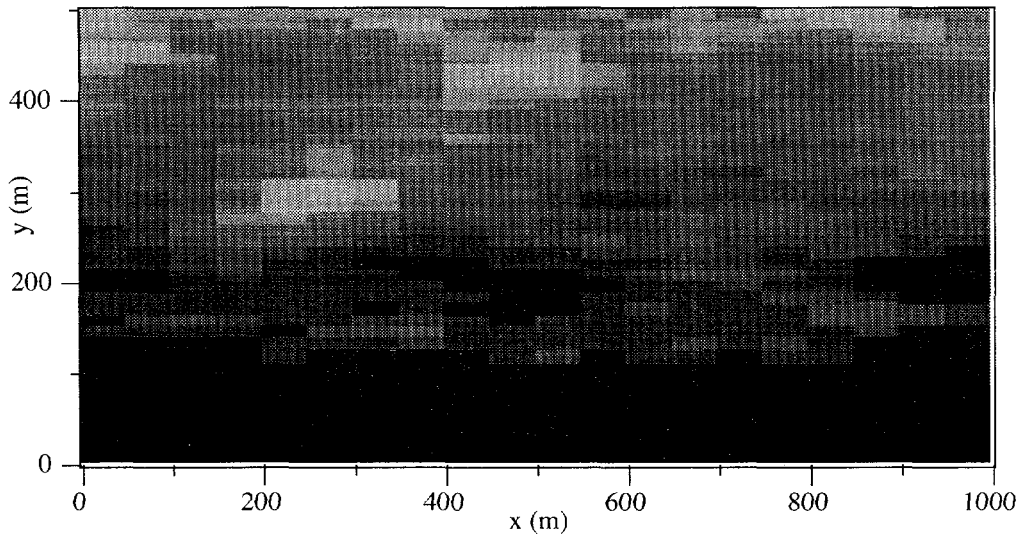

(b) matrix saturation

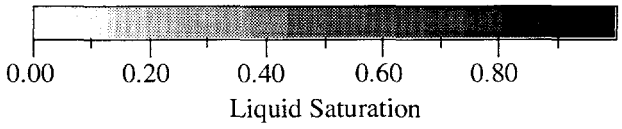

Figure 5.6. Hydrostatic saturation distribution for TOUGH2 model of Benchmark 4: a) fracture saturation b) matrix saturation

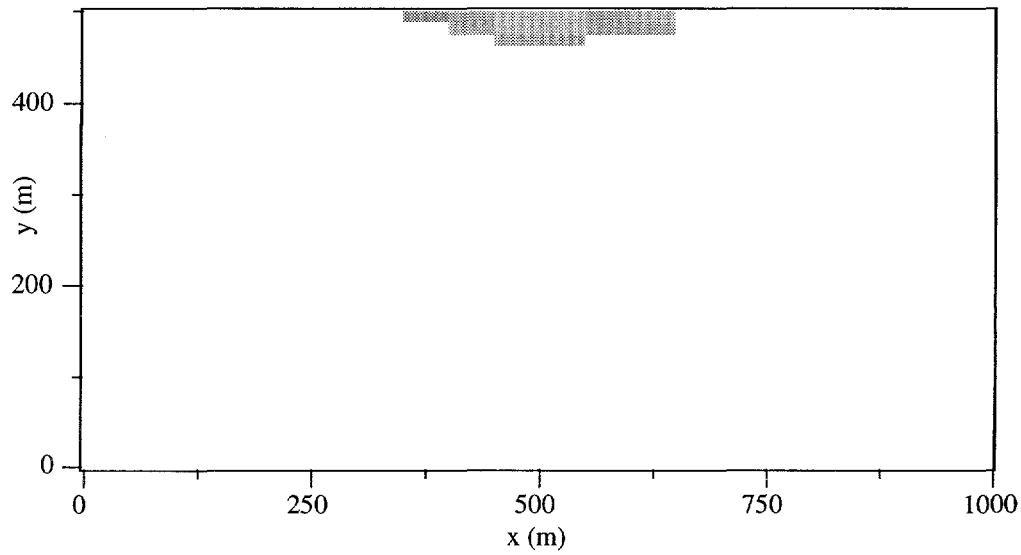

(a) fracture saturation

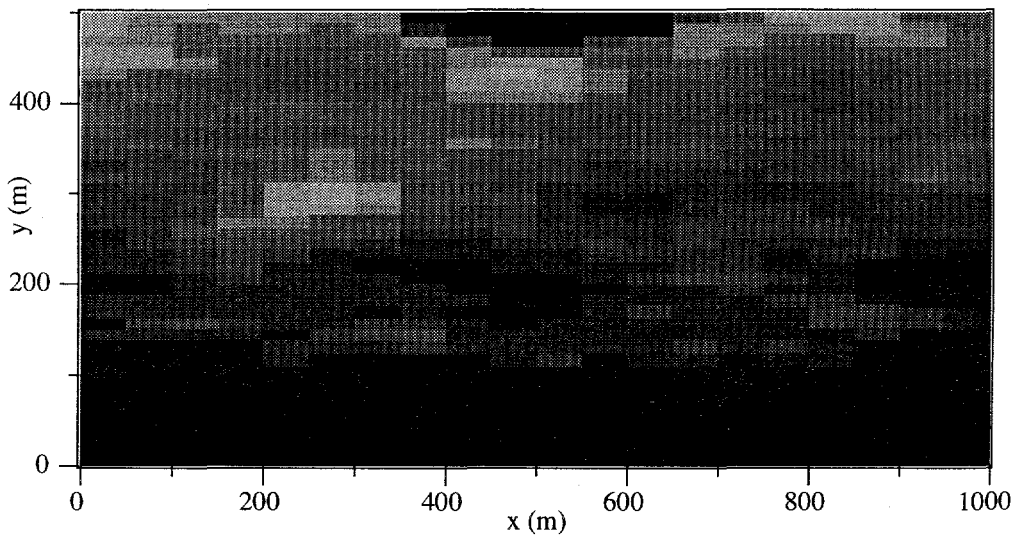

(b) matrix saturation

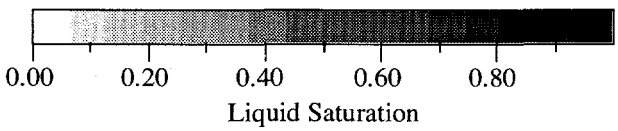

Figure 5.7. ECM saturation distributions for TOUGH2 model of Benchmark 4 after one day of ponding along the top row between x=350 m and x=650 m: a) fracture saturation b) matrix saturation

assumes pressure equilibrium between the fractures and matrix. Because the domain is comprised of composite fracture and material properties, water flows into the domain at a flux commensurate with that of flow through saturated fractures. However, the water is immediately imbibed into the matrix. Thus, for the ECM model, a ponded boundary results in high infiltration rates (due to the fracture properties) and large storage capacities (due to the matrix properties) near the saturated boundary. A significant amount of water enters the domain (3.83e5 kg) as listed in the output file of TOUGH2, but it remains localized near the source.

Figure 5.8 shows the matrix and fracture saturations for the DK model after one day of ponding. The matrix saturations are nearly identical to the hydrostatic saturation distribution. Very little water enters the matrix within one day as a result of the extremely low permeability of the matrix elements. On the other hand, the fracture saturations shown in Figure 5.8 indicate a significant amount of infiltration and deep penetration in the fracture continuum. Unlike the ECM model, flow can be sustained through the fractures in the DK model. Flux also occurs between the fractures and matrix in this case, but since the amount of liquid in the fractures and the hydraulic conductivity of the matrix are relatively small, no noticeable changes occur in the matrix saturations. In fact, the total amount of water entering the system in this case (2.29e5 kg) is less than the amount entering the ECM domain. This discrepancy may be due to the increased channeling of flow in the DK model which may reduce the overall conductivity of the wetted region when compared to the conductivity of the wetted region in the ECM model. The large size of the elements along with numerical dispersion may also contribute to the discrepancy.

Figure 5.8a shows that the flow through the fracture domain shows evidence of channeling as a result of the heterogeneities. Preferential high permeability paths and capillary barriers resulting from the heterogeneous fracture properties both act to cause flow patterns that are analogous to the fingering patterns observed in laboratory studies (Glass and Tidwell, 1991). Obviously, the processes are being simulated on significantly larger scales (tens of meters) than the processes observed in the laboratory (tens of millimeters). This may still be representative of the actual large-scale flow processes if the small-scale processes are self-similar in nature.

One way to account for processes that occur on a scale smaller than the computational grid block is through manipulation of the fracture-matrix conductance term. As discussed in Appendix B, small-scale processes such as fingering and capillary diversion may effectively reduce the conductance term between the fracture and matrix continua. Figure 5.9 shows the matrix and fracture saturations after one day of ponding when the fracture-matrix conductance is reduced by two orders of magnitude. Again, the matrix saturations are not affected in this short time period. However, the fracture domain shows significantly higher saturations and deeper penetration.

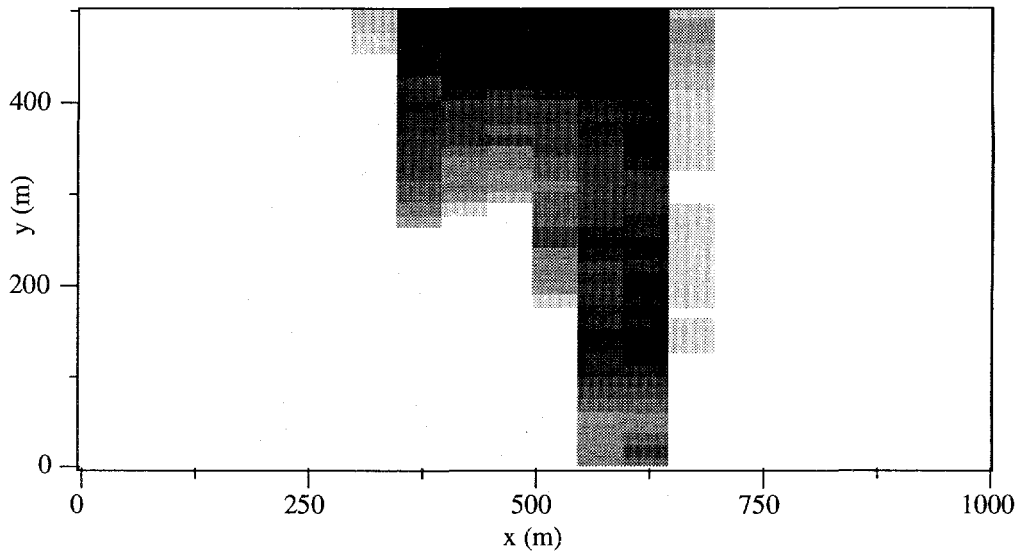

(a) fracture saturation

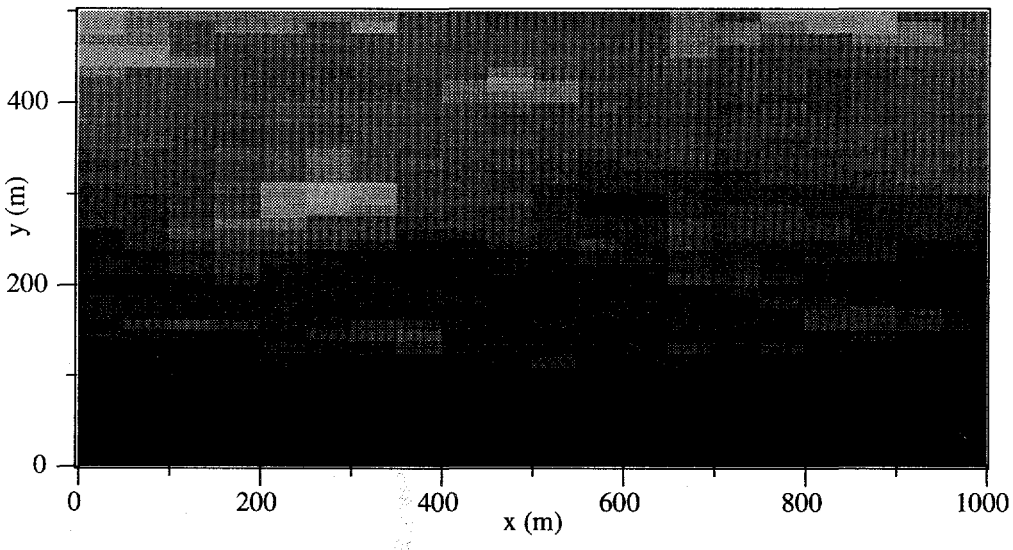

(b) matrix saturation

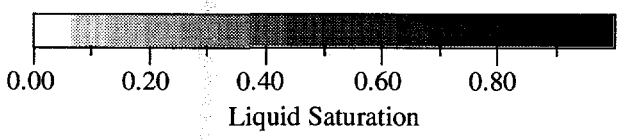

Figure 5.8. DK saturation distributions for TOUGH2 model of Benchmark 4 after one day of ponding along the top row between x=350 m and x=650 m: a) fracture saturation b) matrix saturation

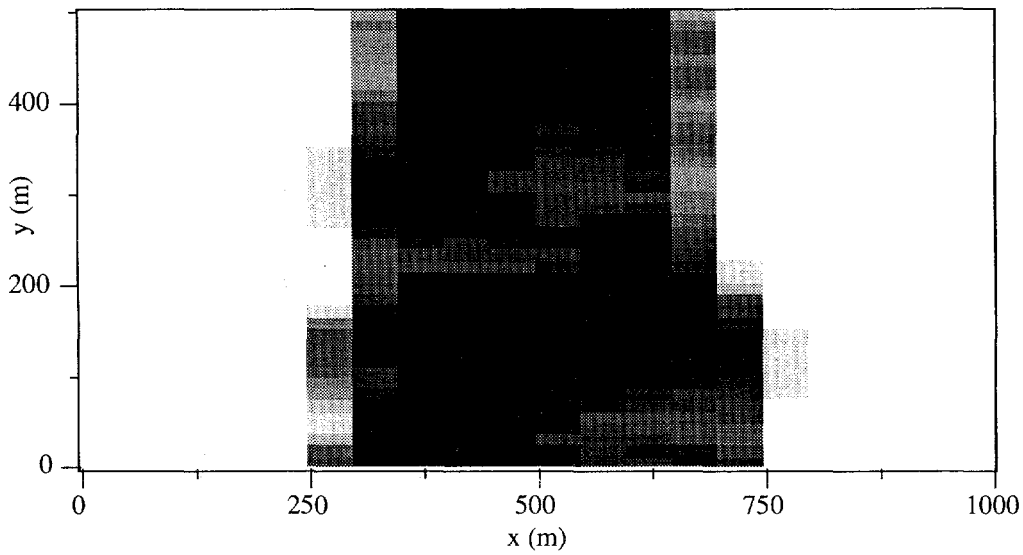

(a) fracture saturation

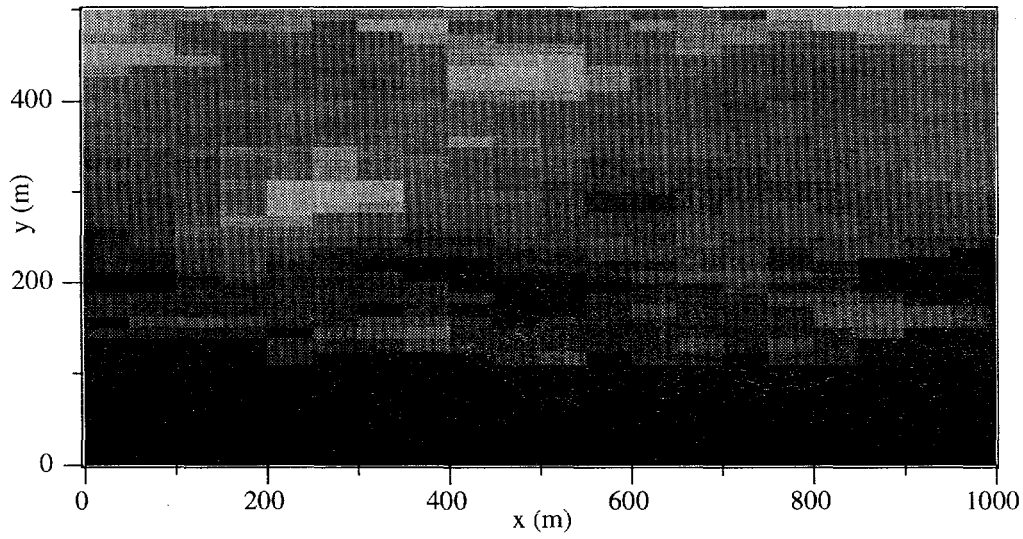

(b) matrix saturation

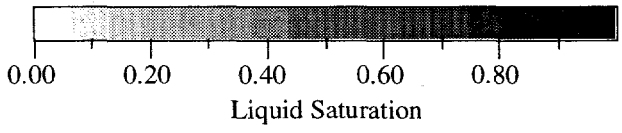

Figure 5.9. DK saturation distributions for modified TOUGH2 model of Benchmark 4 after one day of ponding along the top row between x=350 m and x=650 m: a) fracture saturation b) matrix saturation. The fracture-matrix conductance was reduced by two-orders of magnitude.

Because the fracture-matrix conductance has been reduced, less water is imbibed into the matrix and flow can propagate further through the fracture continuum. Overall, less water enters the system (5.6e4 kg) as compared to the larger quantities entering the ECM and DK models with larger fracture-matrix conductances.

A valid question is whether the previous scenarios predicted by the DK models are realistic, given that flow appears to have propagated several hundred meters through fractured welded tuff over the course of a day. One qualification that must be made in regards to the DK models is that only one matrix element per fracture element was used to represent the matrix continuum. In transient flow scenarios, the initial matrix imbibition can be significantly underestimated if only one element is used to represent the matrix at a given location. If the matrix blocks corresponding to each fracture had been discretized, or if a semi-analytical solution had been used to describe the imbibition into the matrix (as in some dual-porosity models (Zimmerman et al., 1993)), the flow through the fractures may have been significantly retarded. Nevertheless, evidence exists that support the existence of fast flow paths through fractured tuffaceous rock. The elevated distribution of Chlorine-36 (bomb pulse) in the PTn unit indicates that rapid flow of water through fractures in the Tiva Canyon welded unit may have occurred in the past several decades (Fabryka-Martin et al., 1993). Recent field tests also support the possibility that water can flow rapidly through the fractures to great depths over short periods of time in welded tuffs (Nicholl and Glass, 1995).

5.4 Summary

Benchmark 4 examined infiltration into a completely heterogeneous domain representing the TSw unit. Simulations using DUAL and TOUGH2 showed that both codes were capable of simulating flow in the heterogeneous domain with a large number of material parameters. Common trends were observed in the steady-state saturation distribution for a constant infiltration rate of 0.065 mm/year. Regions of high saturation corresponded to regions of low porosity, while low saturations were found in regions of high porosity. In general, the saturations simulated by DUAL were lower than the saturations predicted by TOUGH2, which was consistent with discrepancies found in previous analyses in this report.

An assessment of alternative conceptual models of fracture flow using a ponded boundary condition for Benchmark 4 was also performed. Results showed that the ECM model predicted large amounts of water entering the system, but very little propagation. The high infiltration near the saturated boundary was influenced by the fracture properties of the composite domain, while

the restricted movement resulted from the high capillary suction and storage of the matrix properties. The DK model resulted in significantly more flow and higher saturations through the fracture continuum, but less water entered the system. Channeling, capillary diversions, and preferential flow patterns were observed as a result of the heterogeneities in the fracture and matrix hydrologic (including unsaturated) parameters. Reduction of the fracture-matrix conductance term (see Appendix B) caused even more extensive flow and higher saturations to occur through the fractures. More tortuous flow paths were also observed as a result of the reduced retardation from matrix imbibition.

Chapter
SIX

Reality Check: Comparison to UZ-16 Data

The previous benchmarks were designed to examine the capabilities, strengths, and weaknesses of the three numerical codes being considered for use in GWTT calculations. The hypothetical problems investigated important issues such as layering, capillary barriers, heterogeneous material properties, and boundary conditions. In this chapter, these aspects are combined and applied in the analysis of field data containing porosity and saturation distributions from drillhole UZ-16 at Yucca Mountain, Nevada. Starting with measured values of matrix porosities at UZ-16, all other hydrologic parameters are derived and used in TOUGH2 models to simulate steady-state saturation distributions. These saturations are then compared to the measured saturations at UZ-16 to place a "reality check" on the methods, processes, and parameters being used. Both the equivalent continuum model (ECM) and the dual permeability (DK) model are used in the analyses, and the effects of reducing the fracture-matrix conductance term in the DK model is investigated. Variations in the infiltration boundary condition are also examined to determine the effects of local vs. uniform infiltration sources.

This chapter begins with an introduction to the UZ-16 data set, the models and codes being investigated, and the hydraulic parameter regressions. One-dimensional simulations are then presented which assess the ECM and DK models of fracture flow. The domain is extended to two-dimensions and comparisons are made to the one-dimensional saturation distributions. Variations in the location of the infiltration source are also investigated in the two-dimensional case to determine possible spatial variations in saturations resulting from non-uniform infiltration sources.

6.1 Description of the UZ-16 Study

This section provides a brief description of the UZ-16 data set, the models that are used in the analyses, and the regressions that are used to determine hydrologic parameters from the measured values of matrix porosity. The location of the UZ-16 drillhole is shown in Figure 6.1 in relation to the outline of the potential repository location at Yucca Mountain. The UZ-16 data set used in this analysis was obtained by the U.S. Geological Survey (DTN: GS940508312231.006). It contains, among other properties, the matrix porosity and saturation distributions shown in Figure 6.2. The depth intervals of each unit are presented in Table 6.1. The measured matrix porosities and saturations used in this analysis were calculated in a controlled relative humidity (65%) and temperature (60°C) environment. The purpose of this analysis is to replicate the measured saturations using the measured matrix porosities and derived hydrologic parameters.

Table 6.1. Geologic depth intervals at UZ-16.

unit	TCw	PTn	TSw1	TSw2	TSw3	CHnz	PPnw
depth (m)	12-47	47-70	70-165	165-339	339-355	355-453	453-?

The domain for the one-dimensional model used in the single-phase version of the TOUGH2 code is shown in Figure 6.3. There are 85 elements (each 6 m high x 10 m wide x 1 m thick) in the vertical direction spanning a height of 510 meters. A water table is specified at the bottom boundary, and a constant infiltration source is used at the top boundary. Based on results from Benchmarks 2 and 3, the initial saturation is assumed to be uniform at 0.85 to expedite the steady-state solution. The matrix porosity that is assigned to each element is interpolated from the measured matrix porosities shown in Figure 6.2. The porosities assigned to each element are shown in Figure 6.4 along with the actual data. The matrix porosity of each element is then used to obtain the matrix permeability of each element through the correlation shown in Figure 5.3.[†] Recall that this regression does not account for the anomalous behavior of samples taken from the zeolitized Calico Hills unit—namely, the high porosities of the CHnz unit yield very low permeabilities that do not fit the regression shown in Figure 5.3. Thus, predictions of the saturations in the Calico Hills unit are expected to be poor if the Calico Hills unit in the vicinity of UZ-16 is predominantly zeolitized. Alternative correlations of permeability and porosity in the CHnz unit are examined in subsequent sections.

[†] The permeability is obtained by multiplying the saturated conductivity in the regression by 10^{-7}.

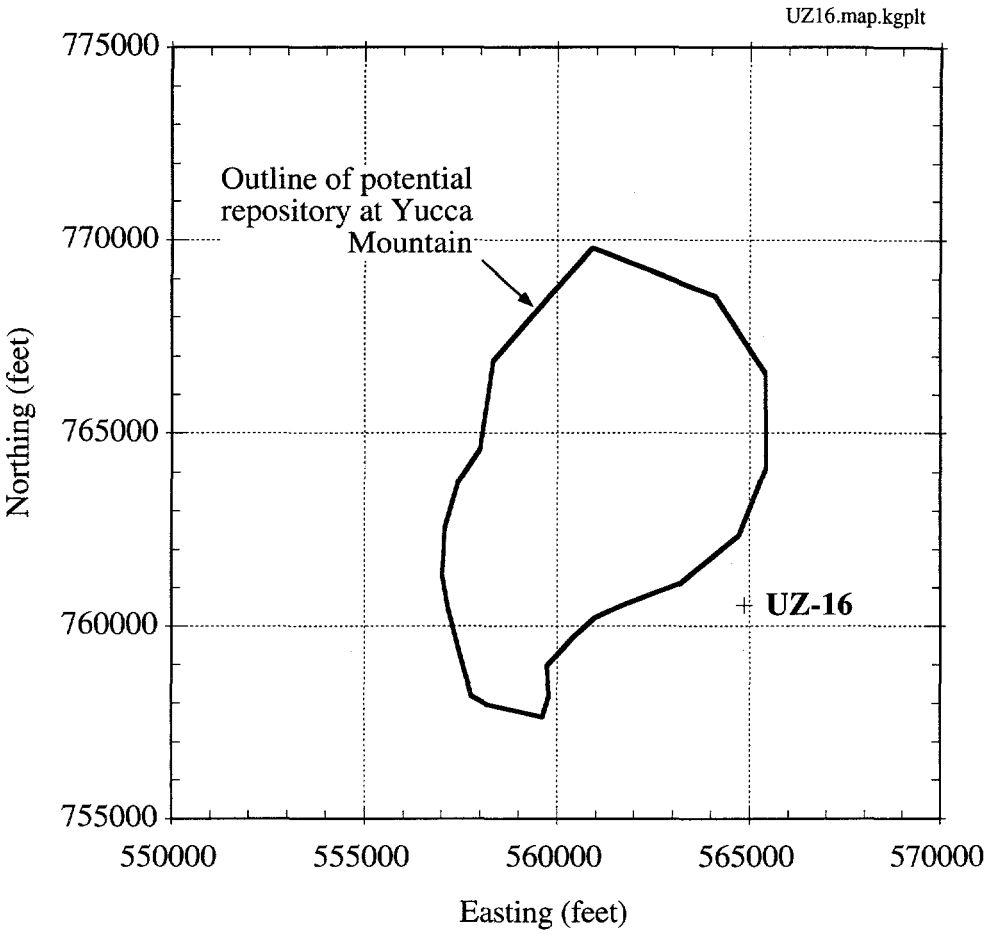

Figure 6.1. Map of the potential repository location at Yucca Mountain showing the location of drillhole UZ-16. Nevada state plane coordinates have been used.

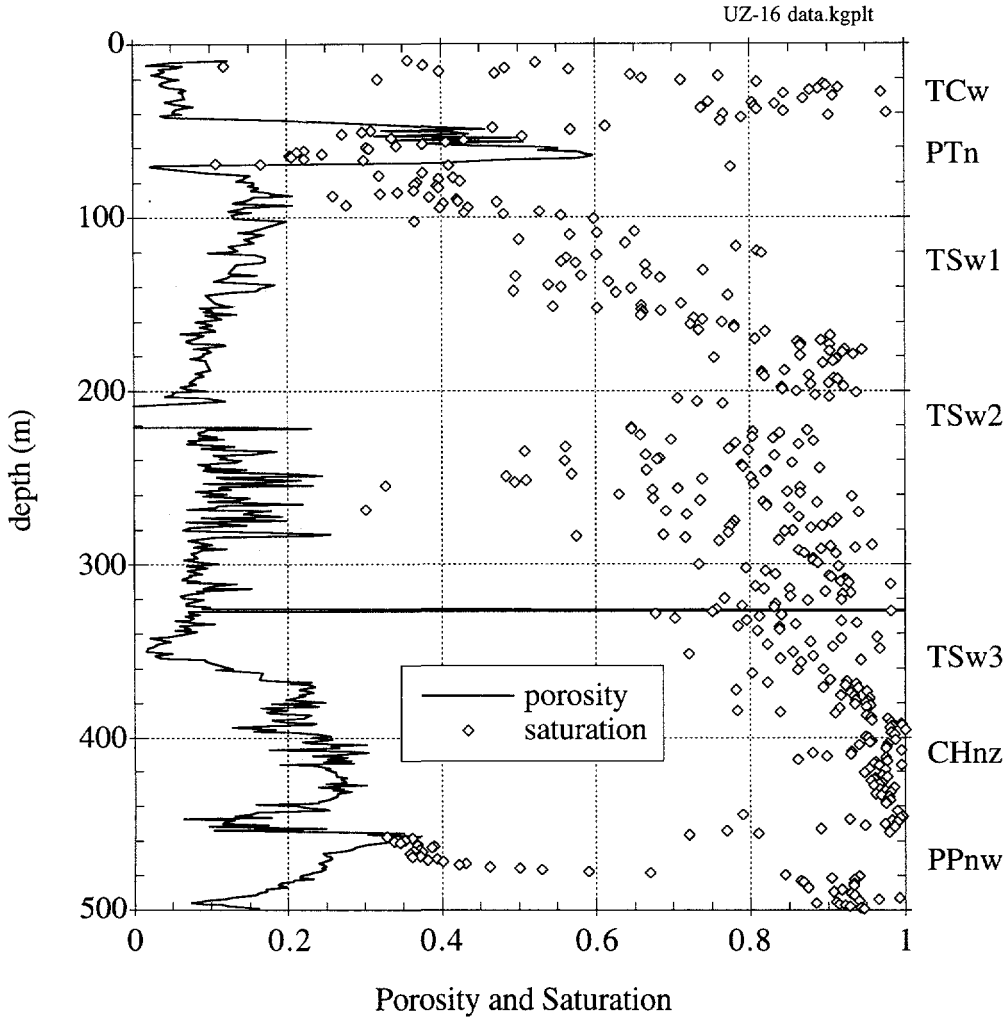

Figure 6.2. Measured porosities and saturations at UZ-16. The data were calculated in a controlled relative humidity (65%) and temperature (60°C) environment (DTN: GS940508312231.006). Unrealistic porosity values (greater than one or less than zero) were not used in the numerical simulations.

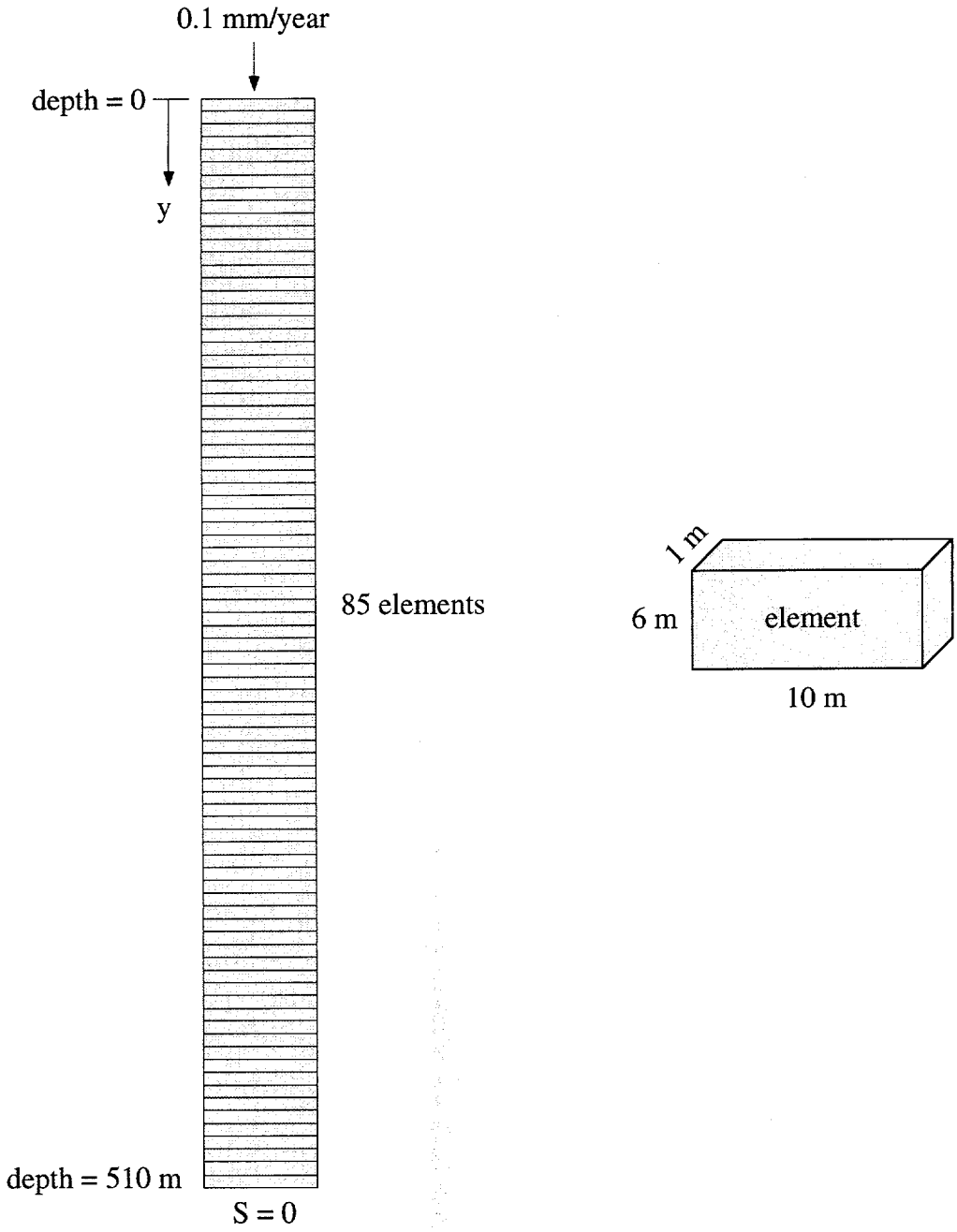

Figure 6.3. TOUGH2 model used in the one-dimensional simulations of drillhole UZ-16.

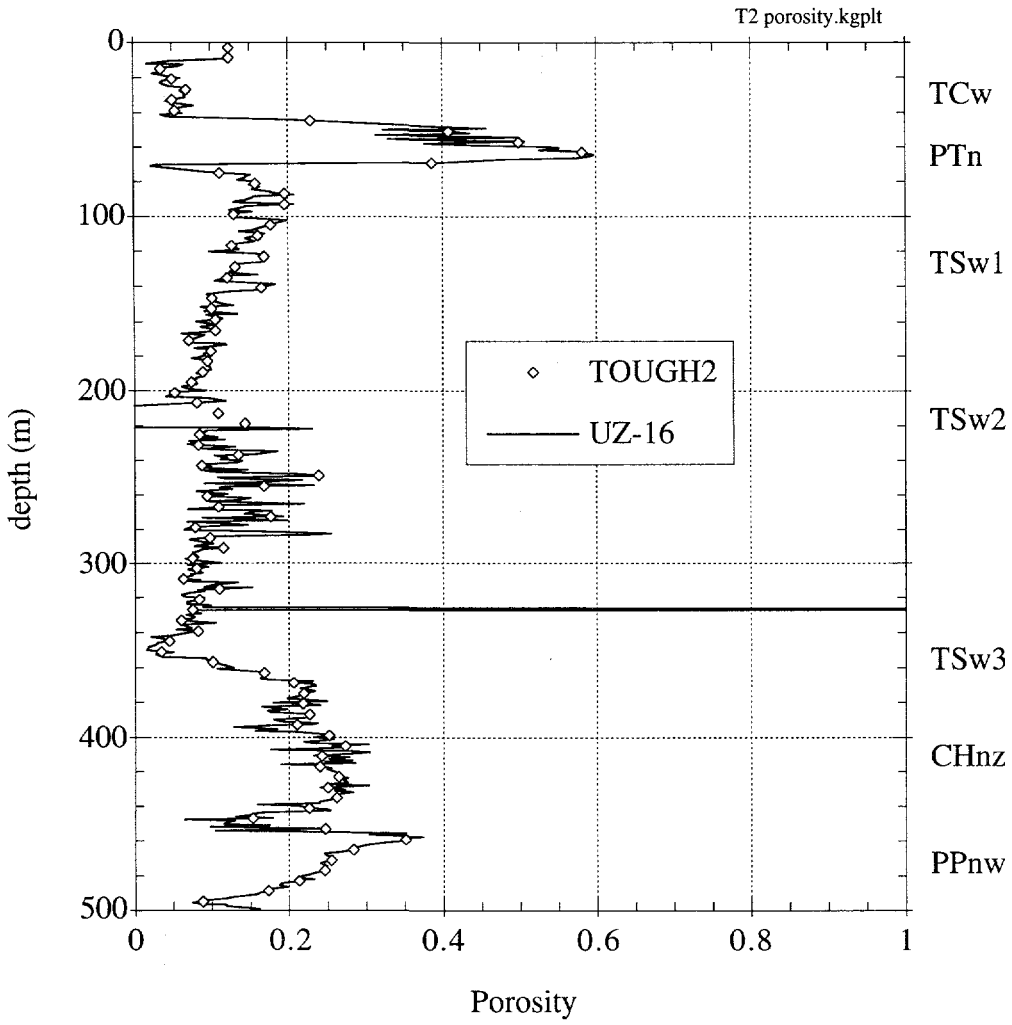

Figure 6.4. Comparison between porosities assigned to each element in TOUGH2 and the measured porosities at UZ-16. Measured porosities greater than one and less than zero were not used in the interpolation.

The additional regressions shown in Figure 5.3 are used to obtain the unsaturated van Genuchten parameters for each matrix element. The fracture properties are derived in a manner consistent with the procedure described in section 5.1.2, and the relevant regressions are shown in Figure 5.4. The unit specifications shown in Table 6.1 are necessary to determine the fracture spacing and matrix residual saturation of the elements within a particular unit given in Table 3.2. The fracture spacings are then used with the fracture porosities (correlated to the matrix porosities as shown in Figure 5.4) to calculate fracture apertures, and the fracture apertures are used to calculate fracture permeabilities and air entry pressures. The Prow Pass unit is assumed to be non-welded beyond 453 meters, so the fracture spacing and matrix residual saturation were assumed to be the same as those listed for the CHnz unit in Table 3.2.

If the ECM model is used, the domain contains 85 elements, each with it own unique set of material properties and characteristic curves consisting of a combination of fracture and matrix parameters derived from the regressions. If the DK model is used, the domain contains 85 fracture elements *and* 85 matrix elements, each with it own unique set of material properties and characteristic curves derived from the regressions (see Appendix B for a discussion of the formulation of the DK parameters). The following section presents one-dimensional TOUGH2 simulations for both models, and comparisons are made to the measured saturations.

6.2 1-D ECM and DK Simulations of UZ-16

Figure 6.5 shows the hydrostatic saturation distribution simulated by TOUGH2 using the ECM with no infiltration. The saturations are seen to be generally lower than the measured saturations at UZ-16, especially in the CHnz unit ($355 \leq$ depth ≤ 453 m). Figure 6.6 shows the resulting saturations when a steady infiltration source of 0.1 mm/year is applied to the top element of the ECM model (in the DK models, infiltration is applied to the fracture elements). The predicted saturations are seen to fall within the scatter of measured saturations except in two regions: the TCw unit and the CHnz unit. As discussed in the previous section, the predicted saturations in the CHnz unit are not expected to match well with the measured saturations because of the anomalous correlation between porosity and permeability in that unit. The measured saturations in the TCw unit are considerably lower than the predicted values presumably because of near surface processes that act to dry out the TCw unit (e.g. evapo-transpiration and capillary wicking).[†] An additional possibility that is investigated in this section is that the ECM model is

[†] To correct for this discrepancy in the TCw unit, a constant saturation (say, ~0.4) could be specified at the top boundary to represent surface processes that include all losses due to evaporation, capillary wicking, etc. A higher

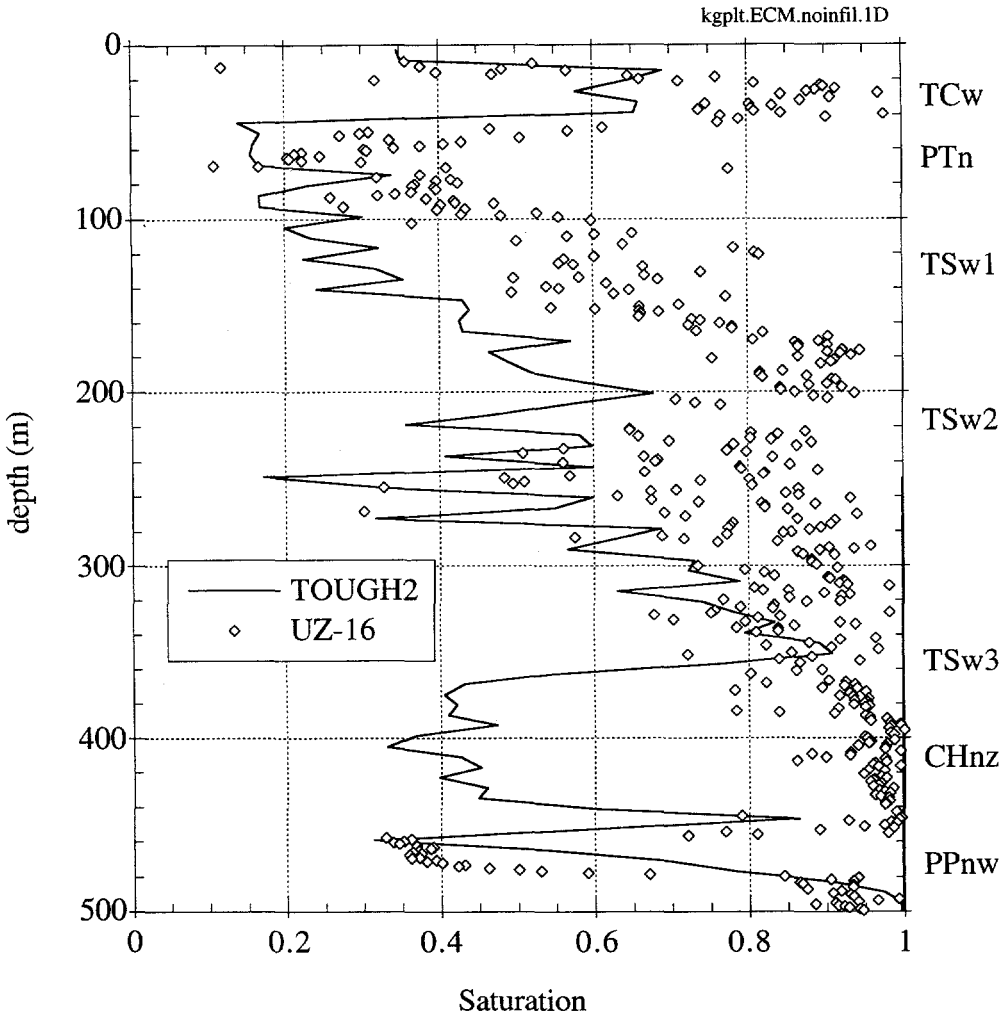

Figure 6.5. Comparison between hydrostatic saturations predicted by the ECM in TOUGH2 (no infiltration) and the measured saturations at UZ-16.

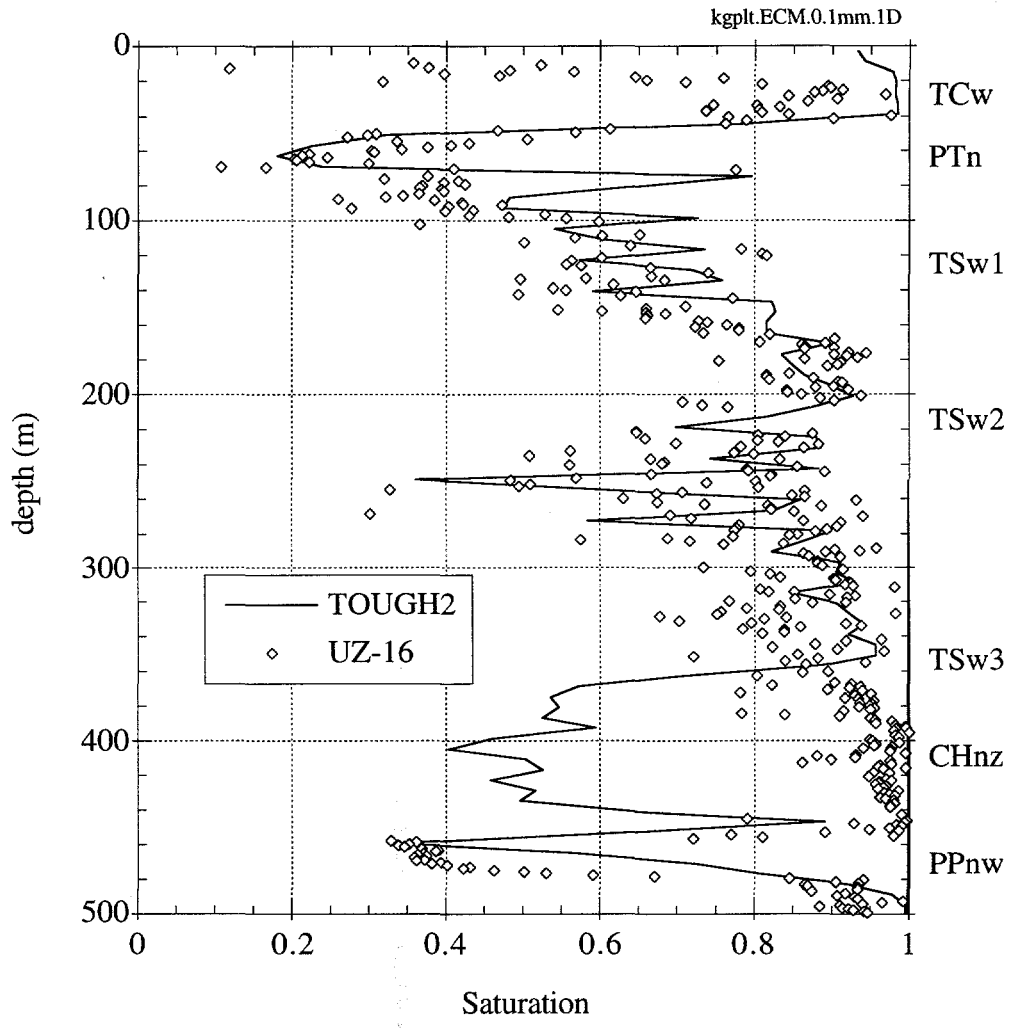

Figure 6.6. Comparison between steady-state one-dimensional TOUGH2 ECM saturations and the measured saturations at UZ-16. The simulated infiltration rate was 0.1 mm/year.

overestimating the matrix saturation in the TCw unit. In previous chapters, the DK model showed lower saturations in the upper unit as a result of higher fluxes being carried through the fractures. In addition, reducing the fracture-matrix connection area in those studies further reduced the saturations in the TCw unit. Thus, the following analysis describes simulations using the TOUGH2 DK model.

Figure 6.7 shows the predicted saturations resulting from the TOUGH2 DK model (see Table 3.3) along with the measured saturation. The results are nearly identical to the ECM saturations. The saturations near the upper part of the TCw are slightly lower than those predicted by the ECM, but they are still significantly higher than the measure values. Figure 6.8 shows the results of the DK model with a fracture-matrix connection area that has been reduced by two orders of magnitude to represent small-scale processes that reduce the conductance between the fractures and matrix elements (see Appendix B). The saturations are slightly lower along the upper TCw unit than the previous models, but they are considerably higher than the measured saturations. Elsewhere in the domain, the ECM and DK saturations are nearly identical. This is in contrast to the results of Benchmark 2, which showed that reducing the fracture-matrix conductance by two orders of magnitude decreased the matrix saturations noticeably. It is postulated that the significant layering being modeled in each unit of this case reduces the discrepancy between matrix saturations in the ECM and DK models in this one-dimensional system. The heterogeneities act to increase the mass flow between the fractures and matrix as a result of processes such as capillary barrier effects in the fracture and matrix domains. In general, the dual permeability models produce nearly identical results to the ECM model for these low infiltration rates (matrix flow predominates). To better replicate the saturations in the TCw unit, it appears that surface processes such as evaporation will need to be considered. We now focus our attention on the CHnz unit and the proper correlation between porosity and permeability for this zeolitized unit.

Because the CHnz unit has relatively high porosities and low permeabilities that do not fit the regression used in Figure 5.3, the following analysis forces the permeability of elements in the CHnz unit to be equal to the expected value for the permeability given by TSPA-93 in Table 3.2. The other regressions in Figure 5.4 are then used to obtain the remaining hydraulic parameters. Figure 6.9 shows the predicted saturations resulting from this adjustment to the TOUGH2 ECM model. The match between the predicted and measured saturations is greatly improved over the previous results using the correlated values for permeabilities in the CHnz unit. Therefore, correlations between permeability (or saturated conductivity) and porosity in the zeolitized units should be developed independently of data from non-zeolitized units to produce reasonable results.

---

infiltration rate would then be needed to simulate saturations in the lower units that are commensurate with the measured saturations.

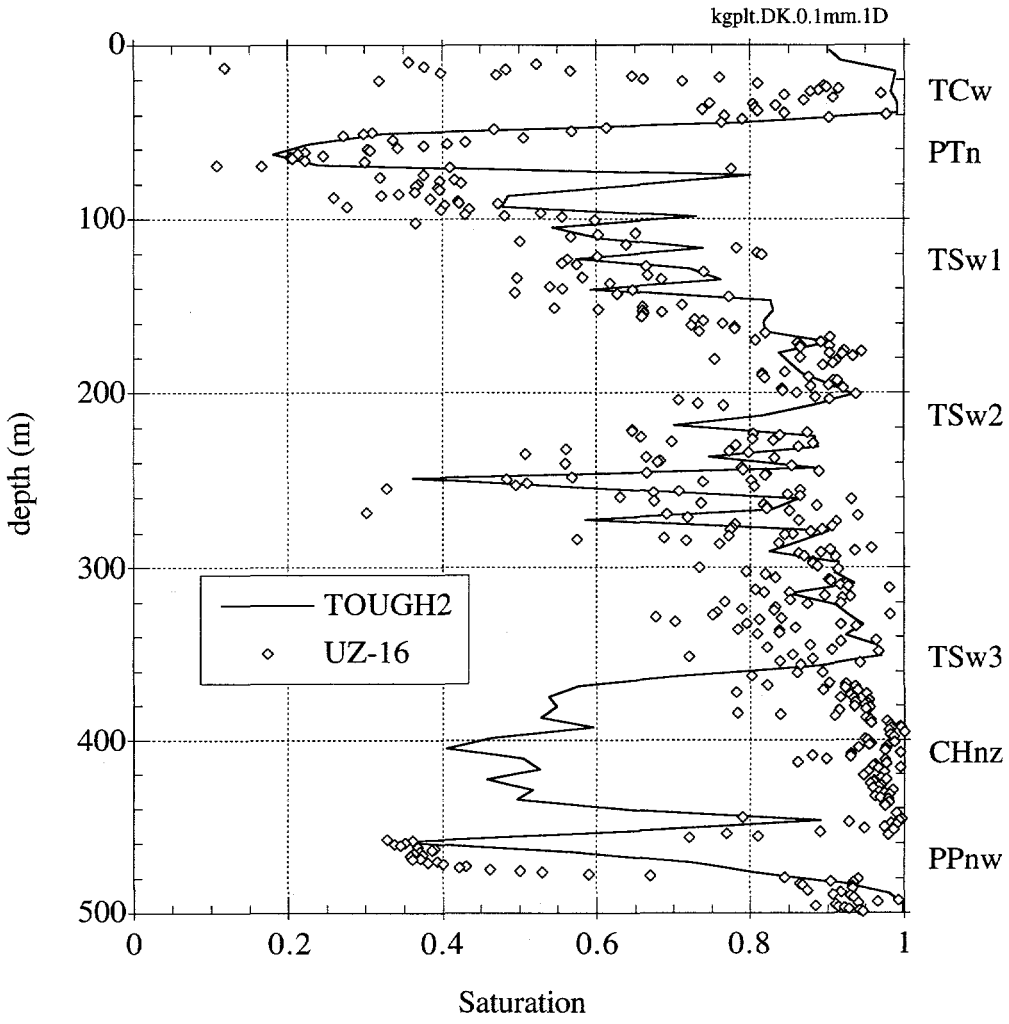

Figure 6.7. Comparison between steady-state one-dimensional TOUGH2 DK matrix saturations and the measured saturations at UZ-16. The simulated infiltration rate was 0.1 mm/year.

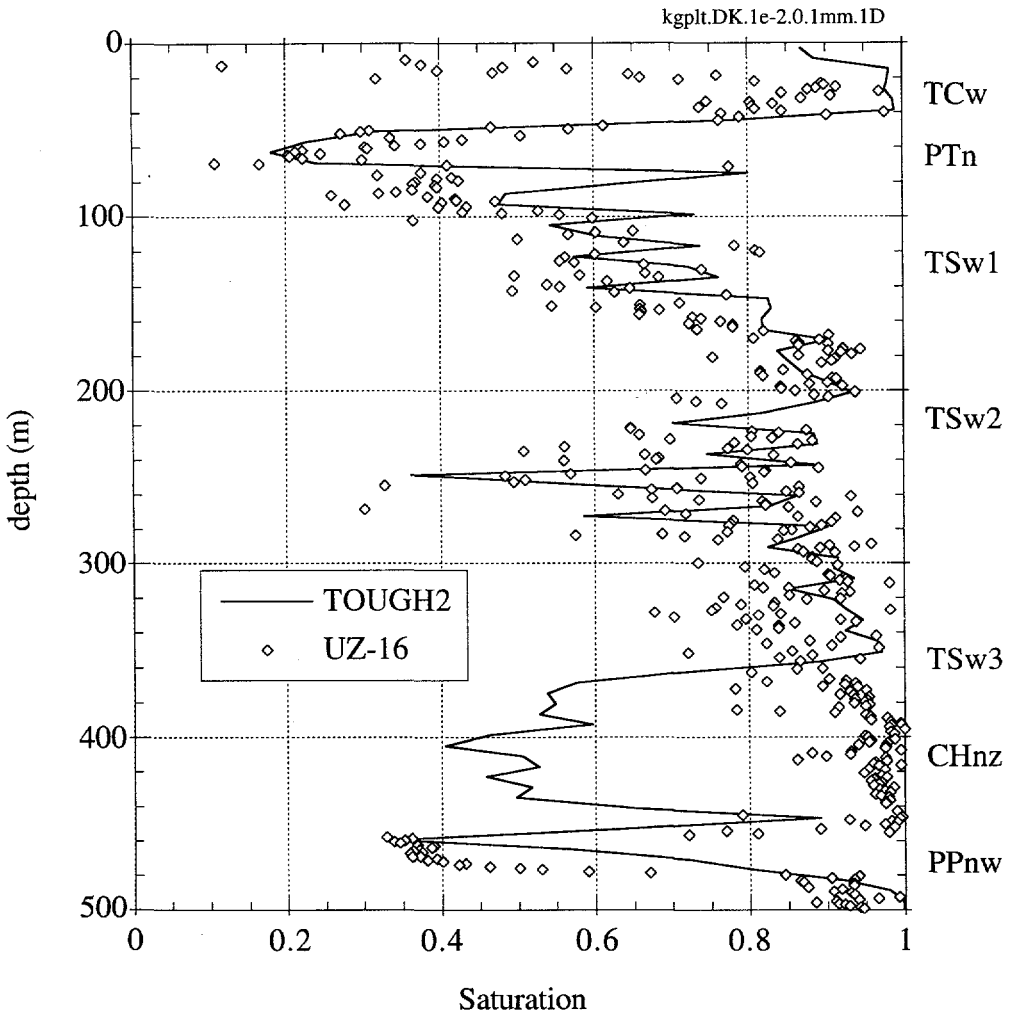

Figure 6.8. Comparison between steady-state one-dimensional TOUGH2 DK matrix saturations and the measured saturations at UZ-16. The fracture-matrix conductance was reduced by two orders of magnitude in TOUGH2. The simulated infiltration rate was 0.1 mm/year.

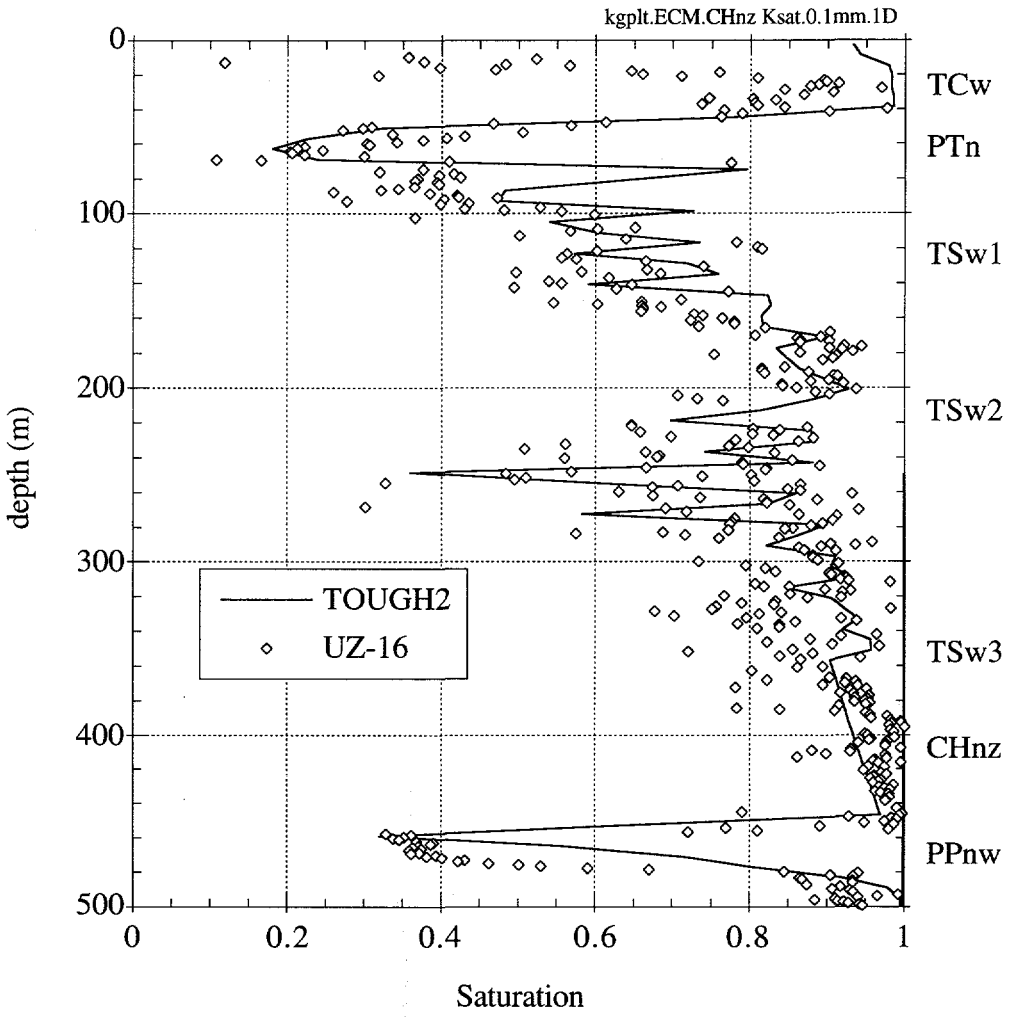

Figure 6.9. Comparison between steady-state one-dimensional TOUGH2 ECM saturations and the measured saturations at UZ-16. The saturated conductivity of the CHnz unit was specified as a constant (Table 3.2), rather than deriving it from matrix porosity. The simulated infiltration rate was 0.1 mm/year.

6.3 2-D ECM and DK Simulations of UZ-16

In this section, the one-dimensional vertical domain described in the previous section is stretched in the horizontal direction by adding additional columns of identical elements. The resulting domain is a two-dimensional region (10 elements (500 m) wide x 85 elements (510 m) high) stratified vertically but homogeneous in the x-direction. All parameters remain identical to those described for the one-dimensional case (the CHnz conductivity is specified rather than correlated). Also, the gravity vector is tilted 6.7° to add an appropriate dip to the two-dimensional domain. Figure 6.10 shows the two-dimensional domain and the corresponding matrix porosities. This two-dimensional region allows investigation of processes such as lateral diversion and localized infiltration.

Figure 6.11 shows the predicted saturation distribution and superimposed velocity profile using the ECM and a constant infiltration rate of 0.1 mm/year. The velocities are predominantly downward with slight evidence of lateral flow above the PTn unit. The saturations of each element are plotted in Figure 6.12 with the measured saturations. In this plot, the measured saturations are plotted as symbols while the predicted saturations are plotted as a small horizontal line. This facilitates visualization of the range of predicted saturations in this two-dimensional system. As in Benchmark 3, the range of saturations results from the imposed no-flow vertical boundaries and lateral diversion. Figure 6.12 shows that the range of predicted saturation in this two-dimensional case matches closely with the measured saturations over most of the data. The measured saturations in the TCw are still considerably lower than the predicted range of saturations, and the measured saturations just beneath the PTn are slightly lower than those predicted by TOUGH2 using ECM.

Figure 6.13 shows the matrix saturation and velocity distribution resulting from the DK model in TOUGH2 using an infiltration rate of 0.1 mm/year. The results are similar to those predicted by the ECM, as are the saturations plotted in Figure 6.14 for the DK simulation. The predicted saturations are seen to be higher in the TCw unit and slightly higher than the measured saturations just below the PTn unit.

One final sensitivity analysis is performed in an attempt to rectify these discrepancies. The infiltration boundary is altered to localize the source of infiltration to just one element at x=75 m. The rate of infiltration is increased from 0.1 mm/year (across ten elements) to 1 mm/year (across one element) to make the total mass flow into the system equivalent. Figure 6.15 shows the resulting steady-state matrix saturations and velocities. The localized infiltration causes the flow to be focused just beneath the source. Significant diversion of the flow occurs in the TCw as a result

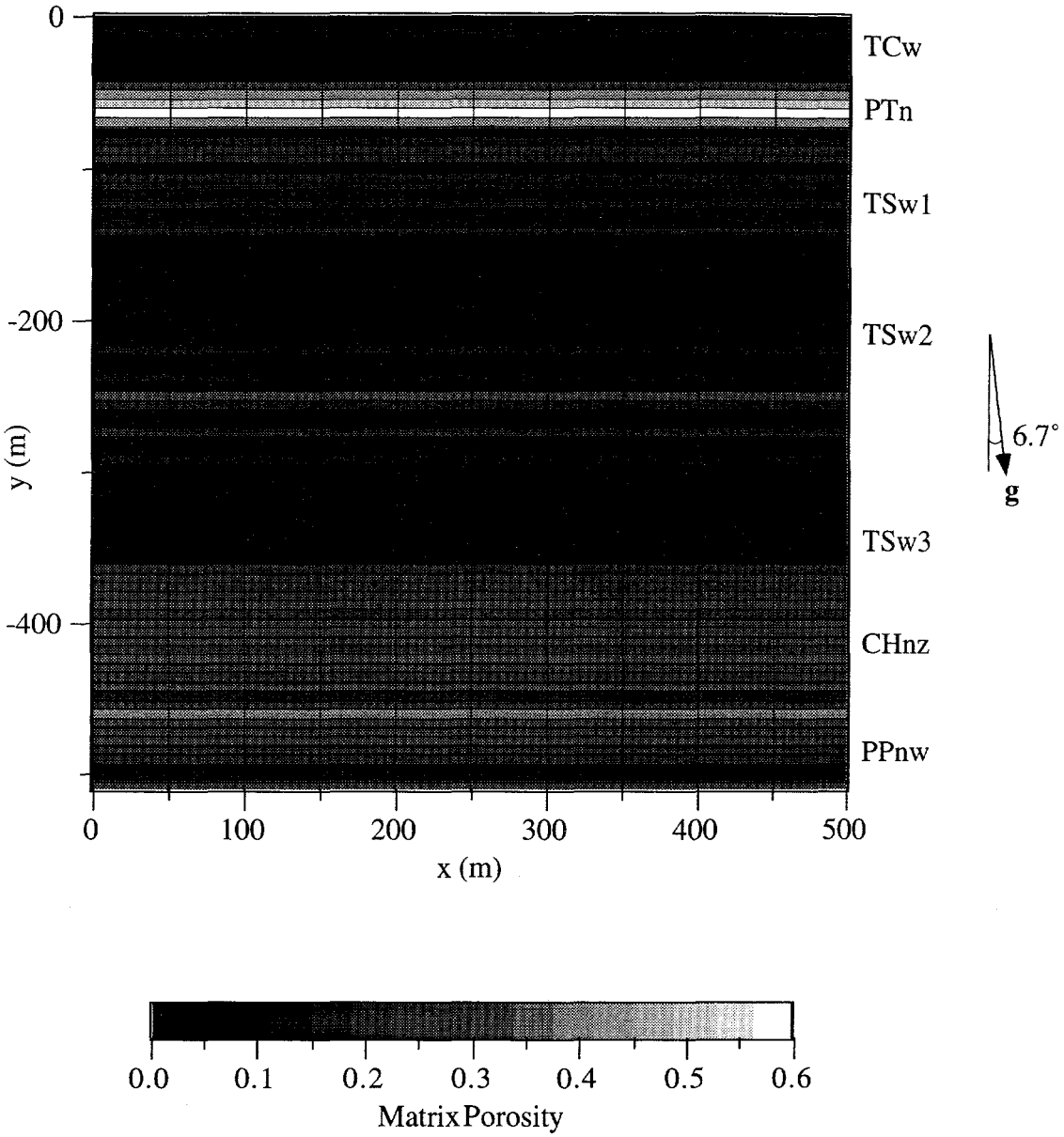

Figure 6.10. Two-dimensional TOUGH2 model of the domain near UZ-16. Each computational element is 6 m high x 50 m wide x 1 m thick. The matrix porosities were interpolated from measured matrix porosities at UZ-16 (see Figure 6.4).

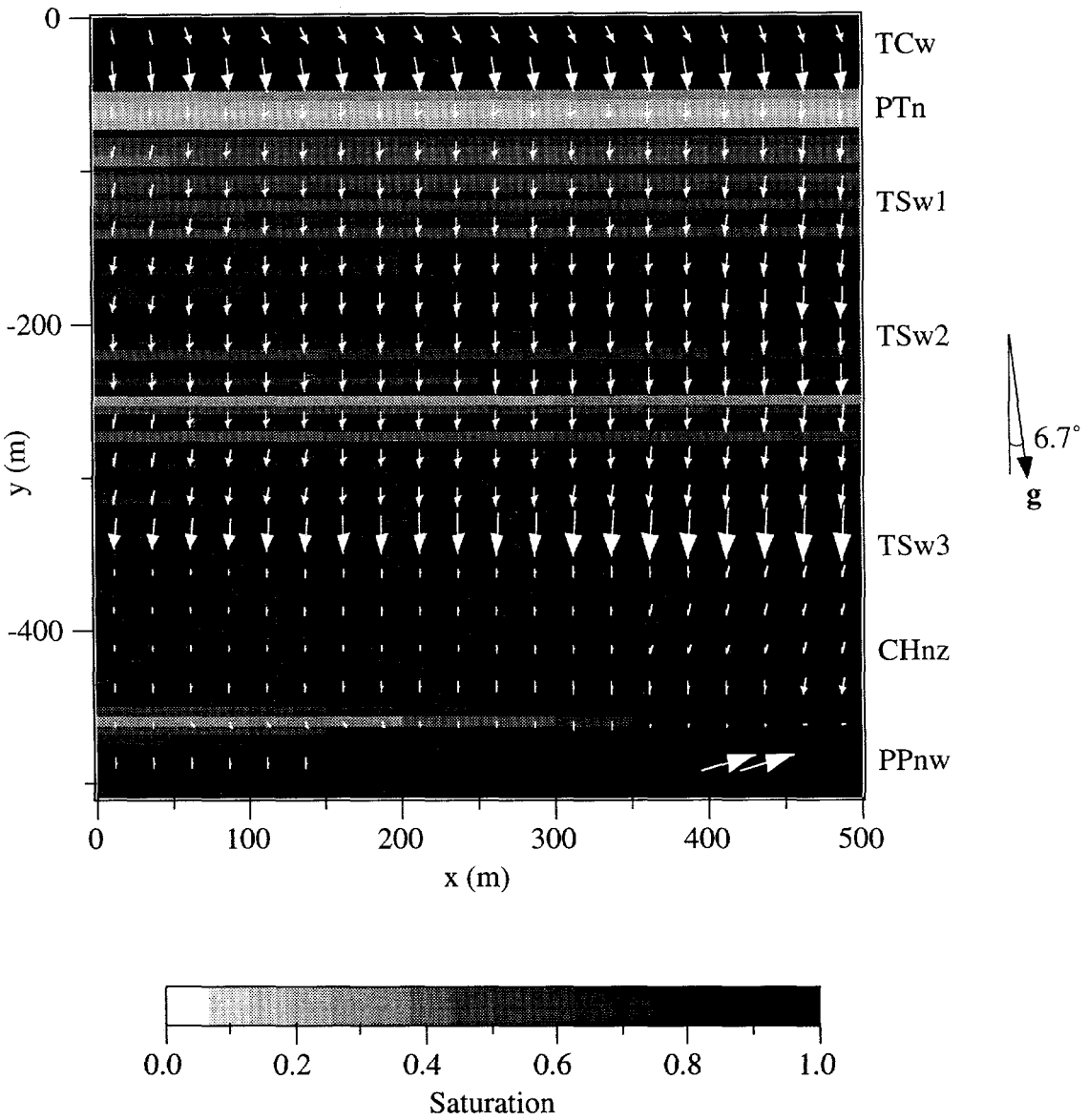

Figure 6.11. Two-dimensional steady-state TOUGH2 ECM saturations and pore velocities resulting from simulations of the domain near UZ-16. The infiltration rate was uniform at 0.1 mm/year. The vectors are scaled to a maximum pore velocity of 3 mm/year (several vectors along the bottom exceed this value and are not shown so that the smaller vectors throughout the domain can be resolved).

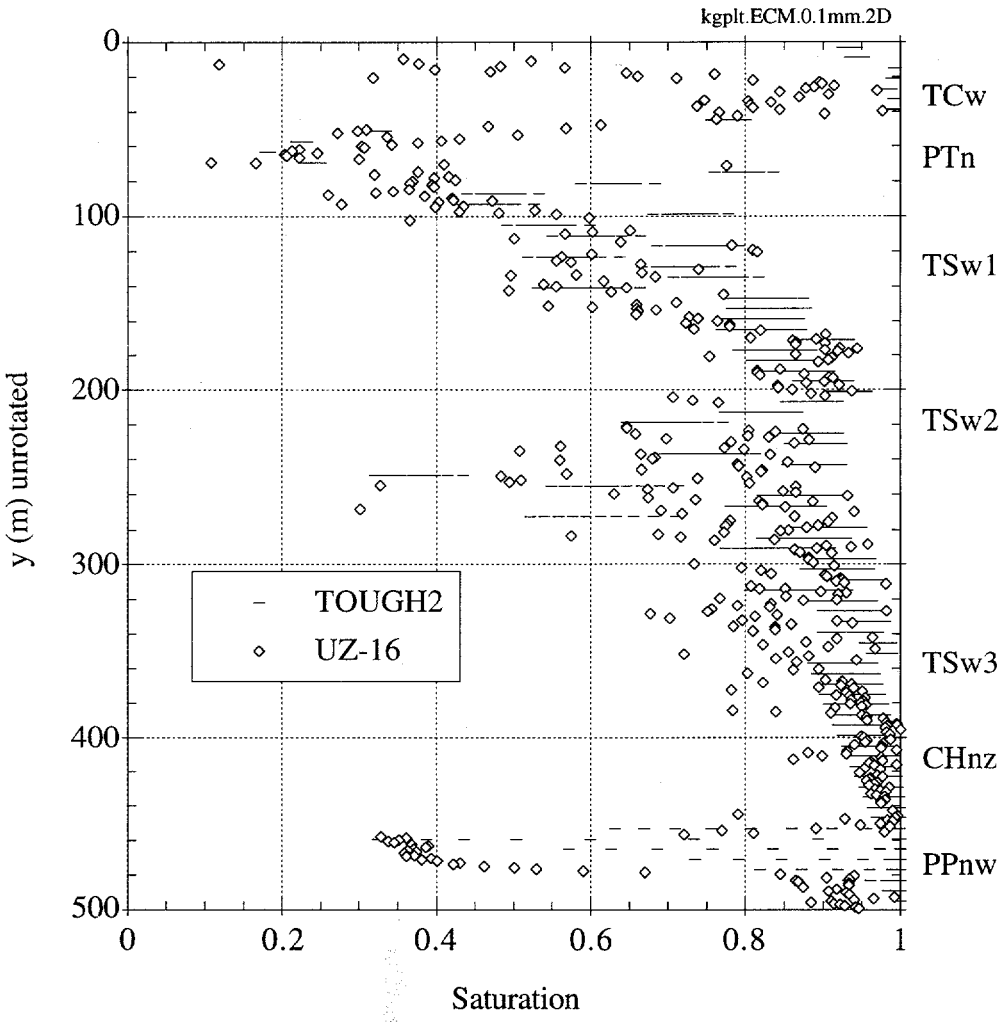

Figure 6.12. Comparison of predicted 2-D TOUGH2 saturations and measured saturations at UZ-16. The ECM model was used in TOUGH2 with a uniform infiltration rate of 0.1 mm/year. Each element's saturation is plotted as a small horizontal line such that a nearly continuous line spans the range of saturations for each row of elements.

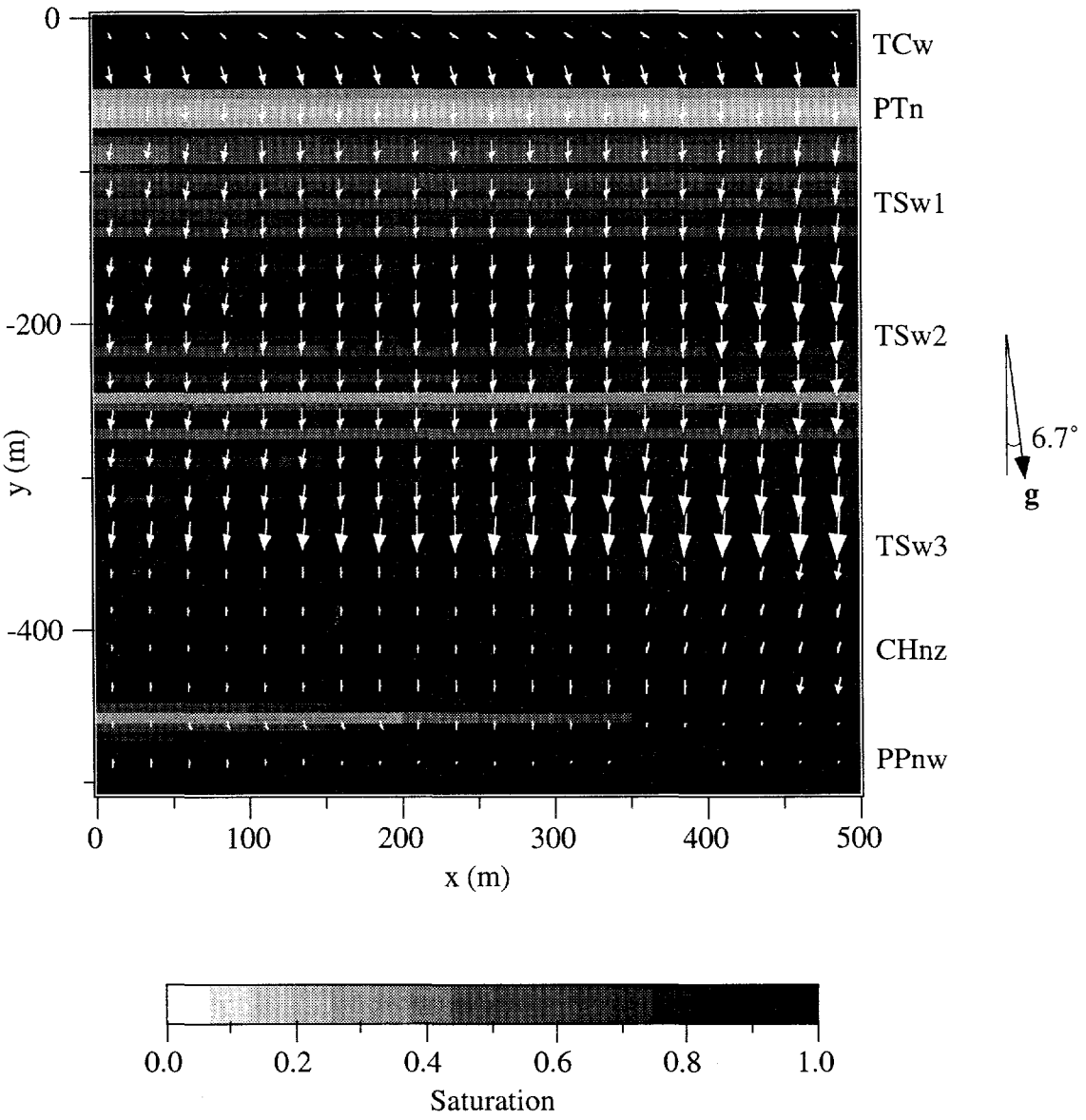

Figure 6.13. Two-dimensional steady-state TOUGH2 DK matrix saturations and pore velocities resulting from simulations of the domain near UZ-16. The infiltration rate was uniform at 0.1 mm/year. The vectors are scaled to a maximum pore velocity of 3.6 mm/year.

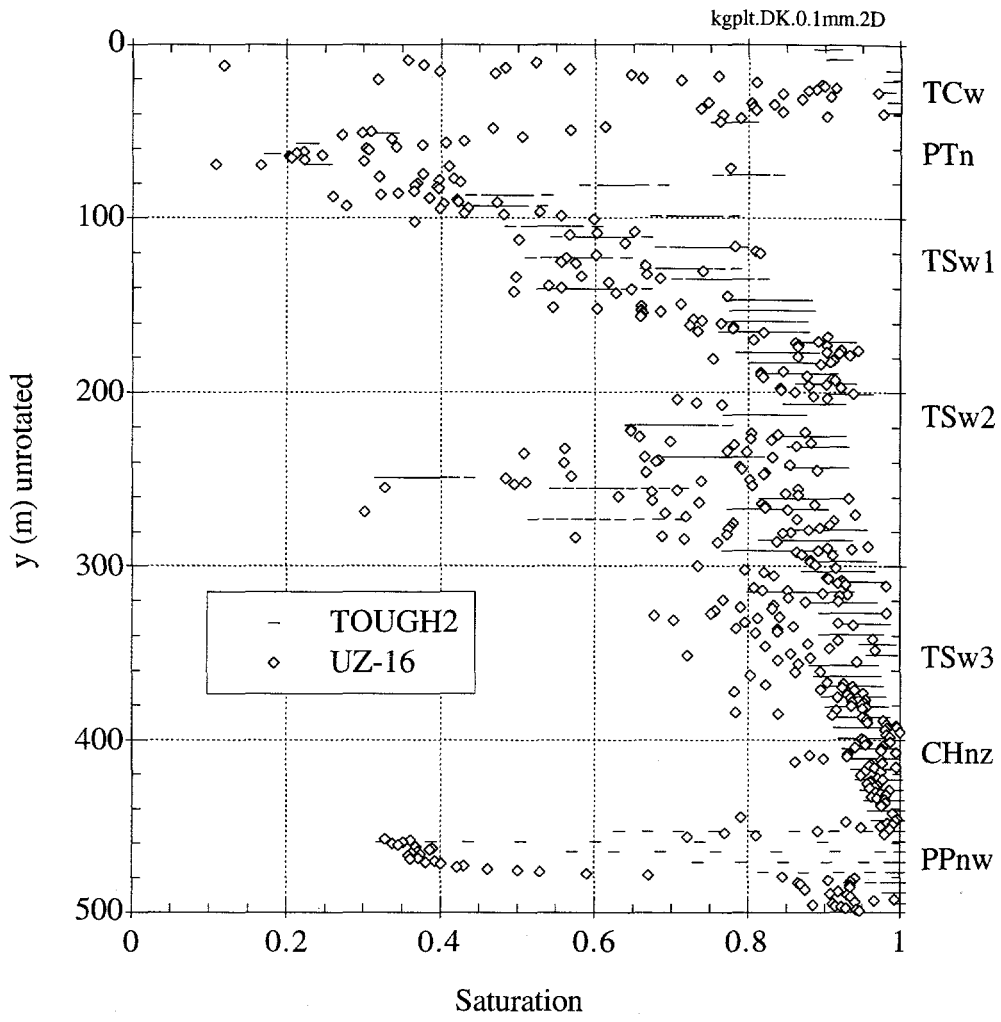

Figure 6.14. Comparison of predicted 2-D TOUGH2 saturations and measured saturations at UZ-16. The DK model was used in TOUGH2 with a uniform infiltration rate of 0.1 mm/year. Each element's saturation is plotted as a small horizontal line such that a nearly continuous line spans the range of saturations for each row of elements.

of lower saturations further away from the source (see discussion on capillary diversion in section 4.2.2). Just beneath the source, flow passes through the PTn and then spreads throughout the TSw unit. The resulting steady-state saturation distribution shows higher saturations beneath the source, but considerably lower saturations away from the source at $x \approx 400$ m in the welded units. Figure 6.16 shows the full range of predicted saturations (each element's saturation is plotted as a small horizontal line) as well as the measured saturations plotted as symbols (diamonds). The saturations in the TCw still remain high, but lower than the previous models. The predicted saturations just below the PTn now fall more closely in the range of measured saturations as a result of the reduced saturation at the top of the TSw unit away from the localized source of infiltration. Elsewhere, the predicted saturations match well with the measured values.

6.4 Summary

Simulations using data obtained from UZ-16 have been performed in this chapter. Attempts were made to replicate the measured saturations using one- and two-dimensional ECM and DK models in TOUGH2. Hydraulic parameters were derived through regressions from measured matrix porosities at UZ-16. Results showed that a separate regression for the conductivity and porosity of the CHnz must be used to obtain reasonable matches in saturation. The relatively high porosities and low permeabilities of the zeolitized Calico Hills unit do not fit the regression used for the other units. Forcing the permeability of the CHnz unit to be the expected value given in TSPA-93 (Table 3.2) yielded good matches with the measured saturations.

The ECM and DK models were found to produce nearly identical results except at the very top of the TCw unit. The DK model produced slightly lower matrix saturations there, which is consistent with previous analyses in this report. However, the measured saturations in the TCw are considerably lower than any predicted values. It was concluded that surface processes contributing to mass loss such as evaporation must be incorporated to better replicate the measured saturation in the TCw unit.

Two-dimensional models of the UZ-16 data produced ranges of saturations throughout the domain that were consistent with the measured saturations and those of the one-dimensional model. However, localized infiltration in the two-dimensional DK model produced greater ranges of saturations that better matched the measured range of saturations just beneath the PTn. Lateral flow along the top of the PTn was also observed in the two-dimensional case with local infiltration.

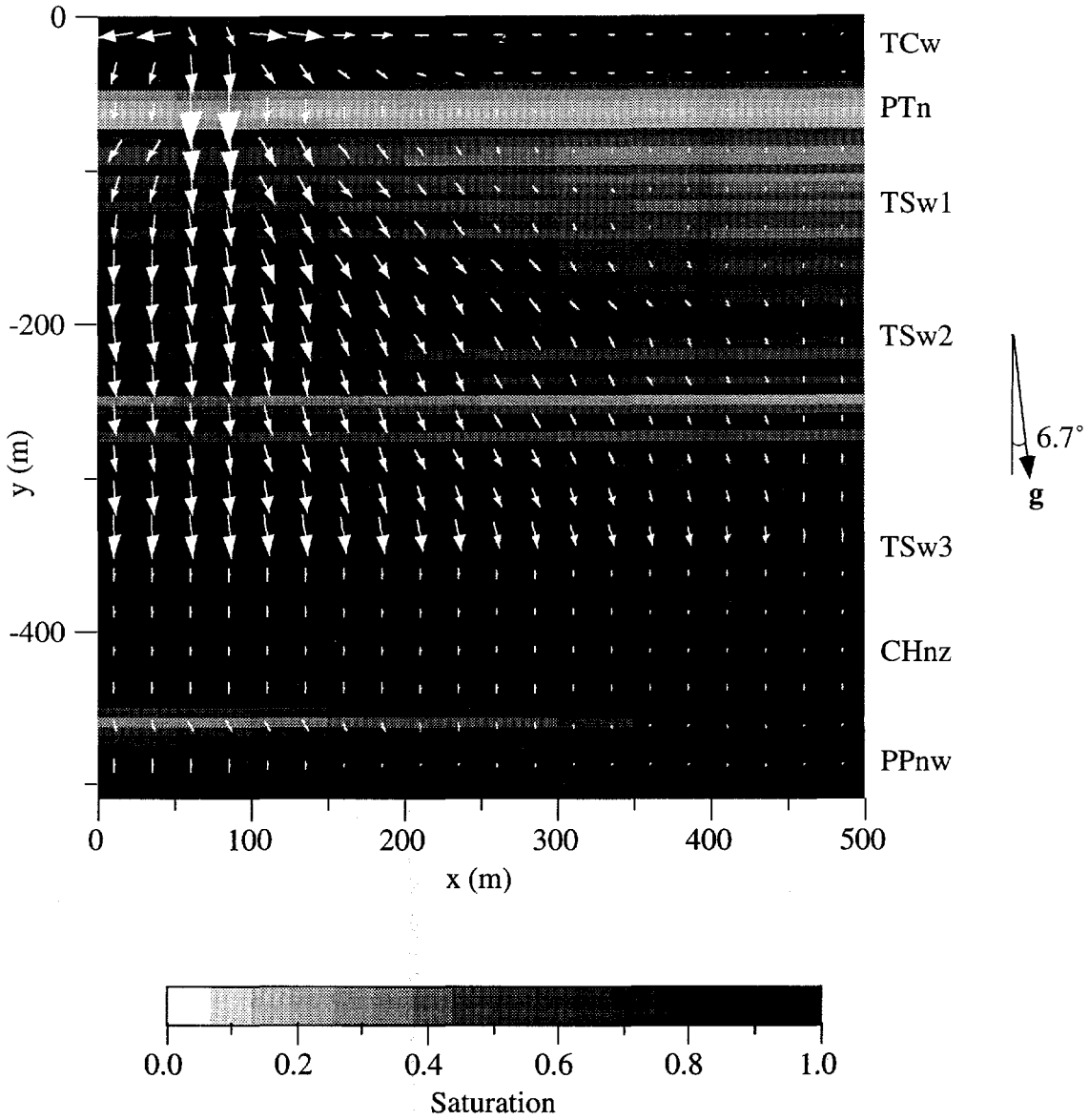

Figure 6.15. Two-dimensional steady-state TOUGH2 DK matrix saturations and pore velocities resulting from simulations of the domain near UZ-16. The infiltration source was applied locally at one element (x=75 m) at a rate of 1 mm/year. The vectors are scaled to a maximum pore velocity of 4.7 mm/year.

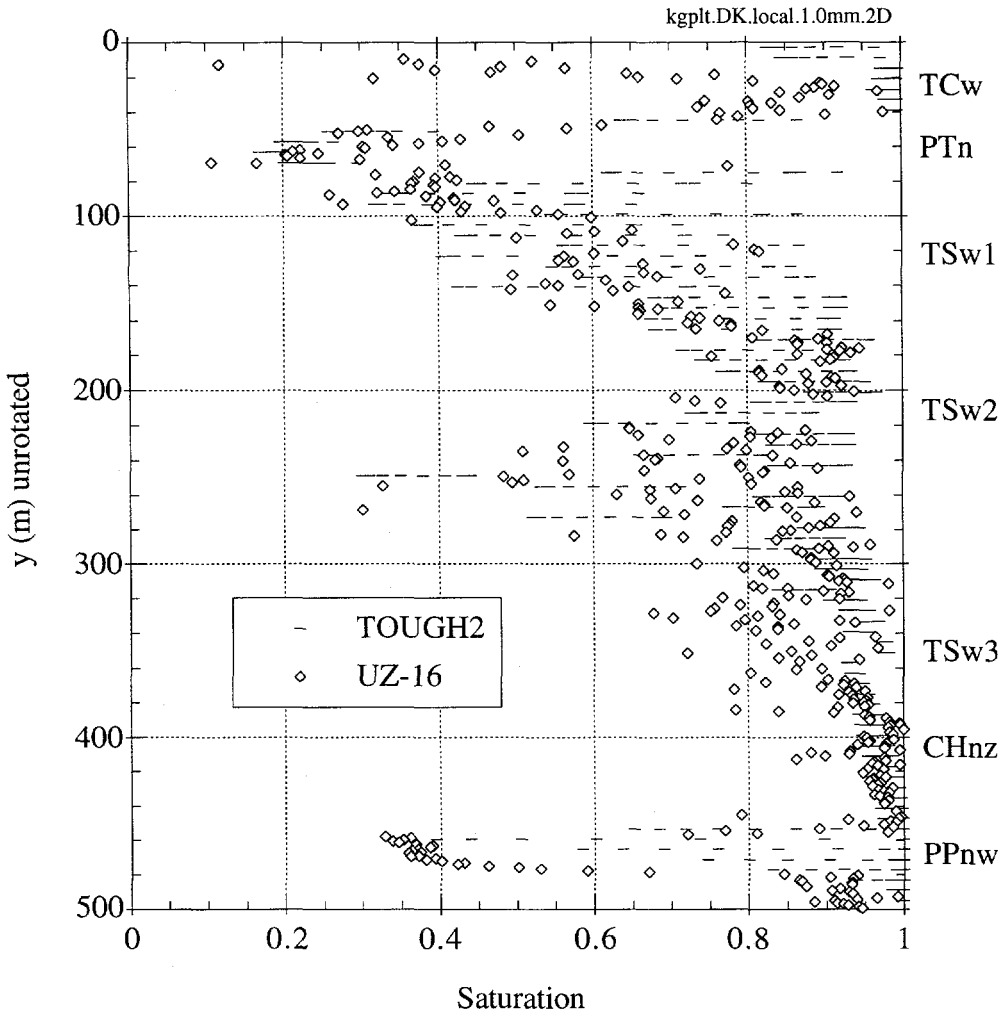

Figure 6.16. Comparison of predicted 2-D TOUGH2 saturations and measured saturations at UZ-16. The DK model was used in TOUGH2 with a localized infiltration applied at one element (x=75 m) at a rate of 1.0 mm/year. Each element's saturation is plotted as a small horizontal line such that a nearly continuous line spans the range of saturations for each row of elements.

In general, these simulations have provided a "reality check" for the processes and parameters being proposed for the GWTT calculations. Although these deterministic models cannot be expected to provide unique solutions based on the limited data, the good match between the predicted and measured saturations at UZ-16 using a variety of conceptual models and boundary conditions builds confidence in the codes and procedures currently being used.

Chapter

SEVEN

Conclusions

A suite of benchmark studies and analyses have been performed to assess alternative conceptual models and codes for calculating flow in fractured media. Each benchmark was designed to address a specific aspect of modeling flow through a fractured rock domain representative of Yucca Mountain. In addition, field-scale simulations and comparisons to data at drillhole UZ-16 have been made to provide a "reality check" on the methods and models being used in this study. Important results, conclusions, and recommendations from each study are summarized below.

Benchmark 1: Homogeneous 1-D Infiltration

The implementation and function of the ECM in the numerical codes DUAL, FEHMN, and TOUGH2 were tested using simulations of 1-D infiltration into a homogeneous domain. Both FEHMN and TOUGH2 yielded accurate steady-state solutions when compared to a semi-analytical solution (Appendix A). DUAL could not replicate the semi-analytical saturation distribution—simulated steady-state saturations using DUAL were considerably lower than the semi-analytical solution and the results of FEHMN and TOUGH2.

Sensitivity analyses revealed that older versions of FEHMN may require modification of the parameter SUPM found in the FEHMN source files. This parameter defines an upper cut-off saturation which is used in the calculation of the two-phase characteristic curves. A value of SUPM between 0.99 and 1.0 was required to obtain good matches of saturations near the water table. However, a recently released version of FEHMN (FEHMN 95-05-01p-sun4) has circumvented this problem.

Single-phase models based on Richards' equation were investigated in FEHMN and TOUGH2 for this benchmark. Results showed that saturation profiles were nearly identical between single- and two-phase simulations through most of the unsaturated region. Near the water

table, the single-phase model produced slightly lower saturation than the two-phase model in TOUGH2. FEHMN produced nearly identical results throughout the entire domain.

Benchmark 2: Layered 1-D Infiltration

DUAL, FEHMN, and TOUGH2 were compared using simulations of steady infiltration into a layered one-dimensional domain. An interesting finding unrelated to the simulation results was that an initial uniform saturation of 0.85 was useful to expedite the steady-state solution. Thus, values for initial saturations expected to be close to the steady-state values are recommended for codes such as TOUGH2 and FEHMN, which require transient simulations to achieve a steady-state solution.

The comparison of the codes revealed that FEHMN and TOUGH2 produced very similar saturation profiles for infiltration rates ranging from 0.1 to 4.0 mm/year. Additional comparisons of these codes with previous analyses by Dykhuizen and Barnard (1992) showed that the results were consistent with other codes. DUAL had troubles simulating infiltration rates other than 0.2 mm/year. At this infiltration rate, resulting saturations from DUAL were lower than the saturations of either FEHMN or TOUGH2.

The ECM and DK models were also assessed using FEHMN and TOUGH2. It was found that the geometric conductance term between the fractures and matrix could be made equivalent between the two codes through the appropriate specification of a length scale parameter in FEHMN. The parameter, APUV1, in FEHMN should be set equal to the fracture spacing divided by $\sqrt{12}$ to provide equivalent conductances between the fractures and matrix in FEHMN and TOUGH2 (see Appendix B). Results of these models showed that the two codes produced similar saturation profiles for both the ECM and DK models at infiltration rates of 0.1 and 4.0 mm/year. However, some discrepancies were observed at 4.0 mm/year, at which the DK model showed evidence of further propagation of flow in the fractures than the ECM. Reducing the conductance between the fractures and matrix by two orders of magnitude to simulate small scale processes such as fingering and channeling had a noticeable effect on the saturation profiles and velocity profiles. In general, reducing the fracture-matrix conductance increased the flux through the fractures, thereby reducing the saturations in the matrix.[†] It would be desirable to quantify the fracture-matrix conductance term through field studies or laboratory experiments.

[†] In chapter 6, reduction of the fracture-matrix conductance did not significantly reduce the matrix saturations. It was hypothesized that the increased number of layers modeled in that study offset the effects of the reduced fracture-matrix conductance.

Further comparisons of the single- and two-phase models in FEHMN and TOUGH2 were made using the ECM model. Results showed that the single- and two-phase results were identical for FEHMN, and the simulation times for FEHMN were similar. TOUGH2 yielded similar single- and two-phase results through most of the unsaturated domain, but the single-phase model yielded slightly lower saturation near the water table. The calculation times using the single-phase version of TOUGH2 were nearly 20 times faster than the two-phase version.

Benchmark 3: Layered 2-D Infiltration

TOUGH2 and FEHMN were used to investigate infiltration into a two-dimensional layered domain with a 6.7° dip. Results showed that capillary diversion of flow occurred at the top of the PTn under unsaturated conditions (infiltration ≤ 0.1 mm/year). For higher infiltration rates (≥ 1.0 mm/year), the welded TCw and TSw units were nearly saturated and maintained low capillary pressures as opposed to the unsaturated PTn unit, which maintained higher capillary pressures. As a result, flow though the unsaturated PTn experienced a capillary diversion at the PTn-TSw interface. Results also showed that lateral diversion in the PTn was very sensitive to the choice of two-phase matrix parameters that were used in the PTn unit. In particular, smaller values of the air entry parameter, α, that were used for the PTn matrix yielded greater lateral diversion through the PTn.

The use of the DK model produced results similar to those presented for the one-dimensional system in Benchmark 2. Propagation of flow through the fractures in the TCw unit caused lower matrix saturations in the TCw and, hence, greater capillary diversion above the PTn. When the fracture-matrix geometric conductance was reduced by two orders of magnitude, the matrix saturations were reduced everywhere as a result of greater fracture flow throughout the entire domain.

Finally, the use of a localized source of infiltration produced a greater range of saturations throughout the two-dimensional domain. Matrix saturations were higher directly beneath the infiltration source, but further away from the infiltration source, the matrix saturations were greatly reduced. This resulted in more focused flow downwards beneath the source as well as a significant amount of lateral diversion in the TCw away from the source.

Benchmark 4: Heterogeneous 2-D Infiltration

Simulations using DUAL and TOUGH2 showed that both codes were capable of simulating flow in the heterogeneous domain with a large number of material parameters. Common trends were observed in the steady-state saturation distribution for an average infiltration rate of 0.065

mm/year. Regions of high saturation corresponded to regions of low porosity, while low saturations were found in regions of high porosity. In general, the saturations resulting from DUAL were lower than the saturations predicted by TOUGH2, which was consistent with discrepancies found in previous analyses in this report.

An assessment of alternative conceptual models of fracture flow using a ponded boundary condition for Benchmark 4 was also performed using TOUGH2. Results showed that the ECM model predicted large amounts of water entering the system, but very little propagation. The high infiltration near the saturated boundary was influenced by the fracture properties of the composite domain, while the restricted movement resulted from the high capillary suction of the matrix properties. The DK model resulted in significantly more extensive flow and higher saturations through the fracture continuum, but less water entered the system. Channeling, capillary diversions, and preferential flow patterns were observed as a result of the heterogeneities in the fracture and matrix hydrologic parameters. Reduction of the fracture-matrix conductance term (see Appendix B) caused even more extensive flow and higher saturations to occur through the fractures. More tortuous flow paths were also observed as a result of the reduced retardation from matrix imbibition.

Reality Check: Comparison to UZ-16 Data

Simulations using field data obtained from drillhole UZ-16 at Yucca Mountain were performed. Attempts were made to replicate the measured saturations using one- and two-dimensional ECM and DK models in TOUGH2. Hydraulic parameters were derived through regressions from measured matrix porosities at UZ-16. Results showed that a separate regression for the conductivity and porosity of the CHnz must be used to obtain reasonable matches in saturation. The relatively high porosities and low permeabilities of the zeolitized Calico Hills unit do not fit the regression used for the other units. Forcing the permeability of the CHnz unit to be the expected value given in TSPA-93 (Table 3.2) yielded good matches with the measured saturations.

The ECM and DK models were found to produce nearly identical results except at the very top of the TCw unit, which showed the DK model producing slightly lower matrix saturations. The measured saturations in the TCw were considerably lower than any predicted values. It was concluded that surface processes contributing to mass loss such as evaporation must be incorporated to better replicate the measured saturation in the TCw unit. Elsewhere in the domain, the ECM and DK results were nearly identical, even when the fracture-matrix conductance was reduced by two orders of magnitude in the DK model. This contrasts with the homogeneous

models studied in Benchmarks 2 and 3, which showed significant reductions in the matrix saturations as a result of a reduction in the fracture-matrix conductance. One hypothesis for the discrepancy is that the significant amounts of heterogeneity included in this analysis had pronounced effects on forcing equilibrium-like conditions between the fractures and matrix under steady-state conditions. Processes such as capillary barriers may have occurred within the fracture and matrix domains, causing more favorable conditions for equilibrium between the fractures and matrix.

Two-dimensional models of the UZ-16 data produced ranges of saturations throughout the domain that were consistent with the measured saturations and those of the one-dimensional model. However, localized infiltration in the two-dimensional DK model produced greater ranges of saturations that better matched the measured saturations just beneath the PTn. Lateral flow along the top of the PTn was also observed in the two-dimensional case with local infiltration.

Remarks and Recommendations:

In general, these benchmarks and analyses have provided assessments, verifications, and a "reality check" for the processes and parameters being proposed for the GWTT calculations. Both FEHMN and TOUGH2 appear to be capable of simulating the desired domains chosen to represent various cross-sections of Yucca Mountain using a variety of alternative conceptual models of fracture flow. Because of its success in these benchmarks and the relatively long "track record" associated with TOUGH2, it is recommended that TOUGH2 be used for UZ calculations in GWTT-95. However, efforts should be made to continue the use of FEHMN in these calculations for further comparisons and calculation of a groundwater travel time.

The dual permeability model should be implemented in GWTT-95 so that both steady-state and transient infiltration boundaries can be simulated. Results of this study have shown that the DK model is necessary to show reasonable propagation of fracture flow under high infiltration rates. Although GWTT-95 may only incorporate steady-state infiltration, future iterations should investigate the effects of transient and spatially varying boundary conditions. It should be noted, however, that the success of the dual permeability model will rely on computational factors. The extreme heterogeneities (which significantly increase the number of different materials required for the fracture and matrix elements) and the subdivision of the matrix elements (to increase accuracy) will negatively impact the computational performance of the dual permeability model. Further studies should be considered to assess these aspects. In addition, parameters that affect the accuracy of the DK model, including the fracture-matrix conductance, need to be more thoroughly assessed through laboratory and/or field analyses.

Chapter

EIGHT

References

Arnold, B.W., S.J. Altman, T.H. Robey, R.W. Barnard and T.J. Brown, 1995, Unsaturated-Zone Fast-Path Flow Calculations for Yucca Mountain Groundwater Travel Time Analysis (GWTT-94), SAND95-0857, Sandia National Laboratories, Albuquerque, NM.

Bear, J., 1972, Dynamics of Fluids in Porous Media, Dover Publications, Inc., New York, pp. 444-446.

Bodvarsson, G.S., Z. Aunzo, G. Chen, C. Haukwa, A. Flint, L. Flint, E. Kwicklis, 1995, Recent Development of the LBL/USGS Site-Scale Model of Yucca Mountain, Nevada, in Proceedings of the Sixth Annual International High Level Radioactive waste Mangement Conference, Las Vegas, NV, pp. 157-159.

Brooks, R.H. and A.T. Corey, 1966, Properties of Porous Media Affecting Fluid Flow, J. Irrigation and Drainage Div., Proc. ASCE, Vol. 92, No. IR2, pp. 61-88. (NNA.870407.0356)

Dudley, A.L., R.R. Peters, J.H. Gauthier, M.L. Wilson, M.S. Tierney, and E.A. Klavetter, 1988, Total System Performance Assessment Code (TOSPAC) Volume 1: Physical and Mathematical Bases, SAND85-0002, Sandia National Laboratories, Albuquerque, NM. (NNA.881202.0211)

Dykhuizen, R.C. and R.W. Barnard, 1992, Groundwater Flow Code Verification "Benchmarking" Activity (COVE-2A): Analysis of Participants' Work, SAND89-2558, Sandia National Laboratories, Albuquerque, NM.

Fabryka-Martin, J.T., S.J. Wightman, W.J. Murhpy, M.P. Wickham, M.W. Cafee, G.J. Nimz, J.R. Southon, P. Sharma, 1993, Distribution of Chlorine-36 in the Unsaturated Zone at Yucca Mountain: An Indicator of Fast Transport Paths, published in Conference Proceedings FOCUS '93: Site Characterization and Model Validation, Las Vegas, NV, pp. 58-68.

Freeze, R.A. and J.A. Cherry, 1979, Groundwater, Prentice-Hall, Inc., New Jersey, p. 29. (NNA.870406.0444)

Glass, R.J. and V.C. Tidwell, 1991, Research Program to Develop and Validate Conceptual Models for Flow and Transport Through Unsaturated, Fractured Rock, SAND90-2261 Sandia National Laboratories, Albuquerque, NM. (NNA.910906.0001)

Klavetter, E.A. and R.R. Peters, 1986, Estimation of Hydrologic Properties of an Unsaturated, Fractured Rock Mass, SAND84-2642, Sandia National Laboratories, Albuquerque, NM. (NNA.870317.0738)

Narasimhan, T.N. and J.S.Y. Wang, 1992, Conceptual, Experimental and Computational Approaches to Support Performance Assessment of Hydrology and Chemical Transport at Yucca Mountain, SAND89-7018, Sandia National Laboratories, Albuquerque, NM.

Nicholl, M.J. and R.J. Glass, 1995, Effective Media Models for Unsaturated Fractured Rock: A Field Experiment, in Proceedings of the Sixth Annual International High Level Radioactive Waste Management Conference, Las Vegas, NV, pp. 39-40.

Prindle, R.W. and P.L. Hopkins, 1990, On Conditions and Parameters Important to Model Sensitivity for Unsaturated Flow Through Layered, Fractured Tuff: Results of Analyses for HYDROCOIN Level 3 Case 2, SAND89-0652, Sandia National Laboratories, Albuquerque, NM.

Pruess, K., 1991, TOUGH2—A General-Purpose Numerical Simulator for Multiphase Fluid and Heat Flow, LBL-29400, Lawrence Berkeley Laboratory, Berkeley, CA. (NNA.940202.0088)

Pruess, K. and T.N. Narasimhan, 1985, A Practical Method for Modeling Fluid and Heat Flow in Fractured Porous Media, Society of Petroleum Engineers Journal, Vol. 25, No. 1, pp. 14-26. (NNA.890522.0235)

Pruess, K., TOUGH User's Guide, LBL-20700, Lawrence Berkeley Laboratory, Berkeley, CA, 1987. (NNA.890315.0010)

Pruess, K., 1983, GMINC—A Mesh Generator for Flow Simulations in Fractured Reservoirs, LBL-15227, Lawrence Berkeley Laboratory, Berkeley, CA. (NNA.910405.0041)

Reeves, M., N.A. Baker, and J.O. Duguid, Review and Selection of Unsaturated Flow Models, Document No. B00000000-01425-2200-00001 Rev. 00, Civilian Radioactive Waste Management System, Management & Operating Contractor Report, April 4, 1994.

Richards, L.A., 1931, Capillary Conduction of Liquids Through Porous Mediums, *Physics*, Vol. 1, pp. 318-333.

Roberts, J.E. and J.M. Thomas, 1990, Mixed and Hybrid Methods, Handbook of Numerical Analysis, Volume II: Finite Element Methods, eds. P.G. Ciarlet and J.L. Lions, North-Holland, Amsterdam, pp. 523-639. (NNA.940303.0055)

Robey, T.H., 1990, The Mixed Finite Element Method, Ph.D. Dissertation, University of New Mexico, Albuquerque, NM. (NNA.930125.0074)

Robey, T.H., 1994, Development of Models for Fast Fluid Pathways Through Unsaturated Heterogeneous Porous Media, SAND93-7109, Sandia National Laboratories, Albuquerque, NM.

Thoma, S.G., D.P. Gallegos, and D.M. Smith, 1990, Effect of Mineral Layers on Capillary Uptake from Fracture Surfaces: Implications for Waste Disposal in Unsaturated, Fractured Rock: Letter report submitted to U.S. NRC Office of Nuclear Regulatory Research, July 1990.

Tsang, Y.W. and K. Pruess, 1990, Further Modeling Studies of Gas Movement and Moisture Migration at Yucca Mountain, Nevada, LBL-29127, Lawrence Berkeley Laboratory, Berkeley, CA.

van Genuchten, M. Th., 1980, A Closed-Form Equation for Predicting the Hydraulic Conductivity of Unsaturated Soils, Soil Sci. Soc. Am. J., Vol. 44, pp. 892-898. (NNA.890522.0287)

Warren, J.E. and P.J. Root, 1963, The Behavior of Naturally Fractured Reservoirs, Soc. Pet. Eng. J., Trans., AIME, Vol. 3, No. 5, pp. 245-255. (NNA.890522.0276)

Wilson, M.L., J.H. Gauthier, R.W. Barnard, G.E. Barr, H.A. Dockery, E. Dunn, R.R. Eaton, D.C. Guerin, N. Lu, M.J. Martinez, R. Nilson, C.A. Rautman, T.H. Robey, B. Ross, E.E. Ryder, A.R. Schenker, S.A. Shannon, L.H. Skinner, W.G. Halsey, J. Gansemer, L.C. Lewis, A.D. Lamont, I.R. Triay, A. Meijer, and D.E. Morris, 1994, Total-System Performance Assessment for Yucca Mountain—SNL Second Iteration (TSPA-1993), SAND93-2675, Sandia National Laboratories, Albuquerque, NM.

Zimmerman, R.W., G. Chen, T. Hadgu, and G.S. Bodvarsson, 1993, A Numerical Dual-Porosity Model With Semianalytical Treatment of Fracture/Matrix Flow, *Water Resources Research*, Vol. 29, No. 7, pp. 2127-2137.

Zyvoloski, G.A., B.A. Robinson, Z.V. Dash, and L.L. Trease, 1995a, Users Manual for the FEHMN Application, LA-UR-94-3788, Rev. 1, Los Alamos National Laboratory, Los Alamos, NM.

Zyvoloski, G.A., B.A. Robinson, Z.V. Dash, and L.L. Trease, 1995b, Models and Methods Summary for the FEHMN Application, LA-UR-94-3787, Rev. 1, Los Alamos National Laboratory, Los Alamos, NM.

Data References

U.S. Geological Survey, 1994, "Core Analysis of Bulk Density, Porosity, Particle Density and In Situ Saturation for Borehole UE-25 UZ #16", DTN: GS940508312231.006.

Appendix

A

Semi-Analytical Solution for an Equivalent Continuum Model of 1-D Steady-State Infiltration

In order to compare various numerical codes and their implementation of the equivalent continuum model for unsaturated flows, a semi-analytical solution has been developed as a reference. The one dimensional, steady-state equation for conservation of mass of a liquid in an unsaturated homogeneous domain can be written as follows:

$$\frac{d}{dy}\left(\frac{k\,k_r}{\mu}\left(\frac{dP_l}{dy}+\rho\,g\right)\right)=0 \qquad \text{(A.1)}$$

where k is the permeability, k_r is the relative permeability, μ is the viscosity of water, P_l is the liquid pressure, ρg is the specific gravity of water, and y is the vertical coordinate (positive upwards) for the composite domain composed of both fractures and matrix. The liquid pressure can be expressed as a function of the capillary pressure and the gas pressure:

$$P_l = P_g - P_c$$

Since the gas pressure is assumed constant, equation (A.1) becomes

$$\frac{d}{dy}\left(\frac{k\,k_r}{\mu}\left(\frac{dP_c}{dy}-\rho\,g\right)\right)=0 \qquad \text{(A.2)}$$

Integrating equation (A.2) with respect to y yields the following:

$$\frac{k\,k_r}{\mu}\left(\frac{dP_c}{dy} - \rho\, g\right) = c_1 = -q \tag{A.3}$$

where c_1 is a constant of integration. The constant of integration is determined by setting the left-hand side of equation (A.3) equal to the specified infiltration rate (Darcy velocity [m/sec]). The imposed downward infiltration rate is negative since the velocity defined by the left-hand side of equation (A.3) is positive upwards. Equation (A.3) can be rearranged and integrated to yield the following:

$$\int_{y_1}^{y_2} dy = \int_{P_c(y_1)}^{P_c(y_2)} \frac{dP_c}{\rho\, g - \frac{\mu\, q}{k\, k_r}} \tag{A.4}$$

Therefore, the elevation can be determined as a function of capillary pressure:

$$y_2 = y_1 + \int_{P_c(y_1)}^{P_c(y_2)} \frac{dP_c}{\rho\, g - \frac{\mu\, q}{k\, k_r}} \tag{A.5}$$

In equation (A.5), the only unknown is the relative permeability, k_r, which must be expressed as a function of capillary pressure. An expression relating saturations to capillary pressures is also desired so that saturations can be plotted as a function of y. The van Genuchten equations (1980) describing relative permeability and saturation as a function of capillary pressure can be used to obtain these relations:

$$k_{r,j} = \frac{\left(1 - \left(\alpha_j P_c\right)^{\beta_j - 1}\left(1 + \left(\alpha_j P_c\right)^{\beta_j}\right)^{-\lambda_j}\right)^2}{\left(1 + \left(\alpha_j P_c\right)^{\beta_j}\right)^{\lambda_j / 2}} \tag{A.6}$$

$$S_j = S_{r,j} + \left(S_{s,j} - S_{r,j}\right)\left(1 + \left(\alpha_j P_c\right)^{\beta_j}\right)^{-\lambda_j} \qquad \text{(A.7)}$$

j = matrix or fracture

where α and β are fitting parameters, λ is equal to $1-1/\beta$, S_r is the residual saturation, S_s is the maximum saturation, and the subscript j denotes either the fracture or matrix materials.

If the domain were comprised of a single porosity material, equation (A.6) could be used directly in equation (A.5) to determine the capillary pressure distribution. Equation (A.7) could then be used to determine the saturation distribution. However, since the equivalent continuum model is being addressed here, the domain is comprised of both fractures and matrix where only the pressure is assumed to be in equilibrium between the two. The saturations, and hence relative permeabilities, can be drastically different in the two media. Therefore, the relative permeability that must be used in equation (A.5) is a combination of the fracture and matrix relative permeabilities given in equation (A.6). The intrinsic permeability, k, is also a combination of fracture and matrix intrinsic permeabilities. The resulting product of the intrinsic permeability and the relative permeability in equation (A.5) is expressed as follows.

$$k\,k_r = k_f\,k_{r,f}\,\phi_f + k_m\,k_{r,m}\left(1-\phi_f\right) \qquad \text{(A.8)}^{\dagger}$$

where the subscripts f and m denote the fracture and matrix materials. Equations (A.6) and (A.8) can be used in equation (A.5) to determine the capillary pressure distribution using numerical quadrature. Once the capillary pressure distribution is determined, the individual fracture and matrix saturations can be solved using equation (A.7). These individual saturations are then used in the following equation to determine the composite saturation:

$$S = \frac{S_f\,\phi_f + S_m\left(1-\phi_f\right)\phi_m}{\phi_f + \left(1-\phi_f\right)\phi_m} \qquad \text{(A.9)}$$

Equations (A.5)–(A.9) can be used to determine the equivalent continuum saturation distribution resulting from one-dimensional infiltration into a homogeneous, unsaturated domain consisting of both fractures and matrix materials. As an illustrative example of the effects of combining fracture

† Note that the fracture porosity in equations (A.8) and (A.9) is defined relative to the total volume (m^3 pore in fracture/m^3 total), while the matrix porosity is defined relative to the matrix volume (m^3 pore in matrix/m^3 matrix).

and matrix materials in the equivalent continuum model, Figure A.1 shows the fracture, matrix, and composite saturations as a function of capillary pressure for TSw2. In addition, Figure A.2 shows the relative permeabilities of the fracture, matrix, and composite materials as a function of capillary pressure. The material properties for TSw2 are taken from Klavetter and Peters (1986) and are listed in Table A.1.

Table A.1. Material properties for TSw2 (Klavetter and Peters, 1986).

	Fracture	Matrix
permeability, k [m^2]	1.7×10^{-12}	1.9×10^{-18}
porosity, ϕ	1.8×10^{-4}	0.11
α [1/Pa]	1.31×10^{-4}	5.78×10^{-7}
β	4.23	1.798
$\lambda = 1 - 1/\beta$	0.764	0.444
S_r	0.0395	0.08
S_s	1.0	1.0

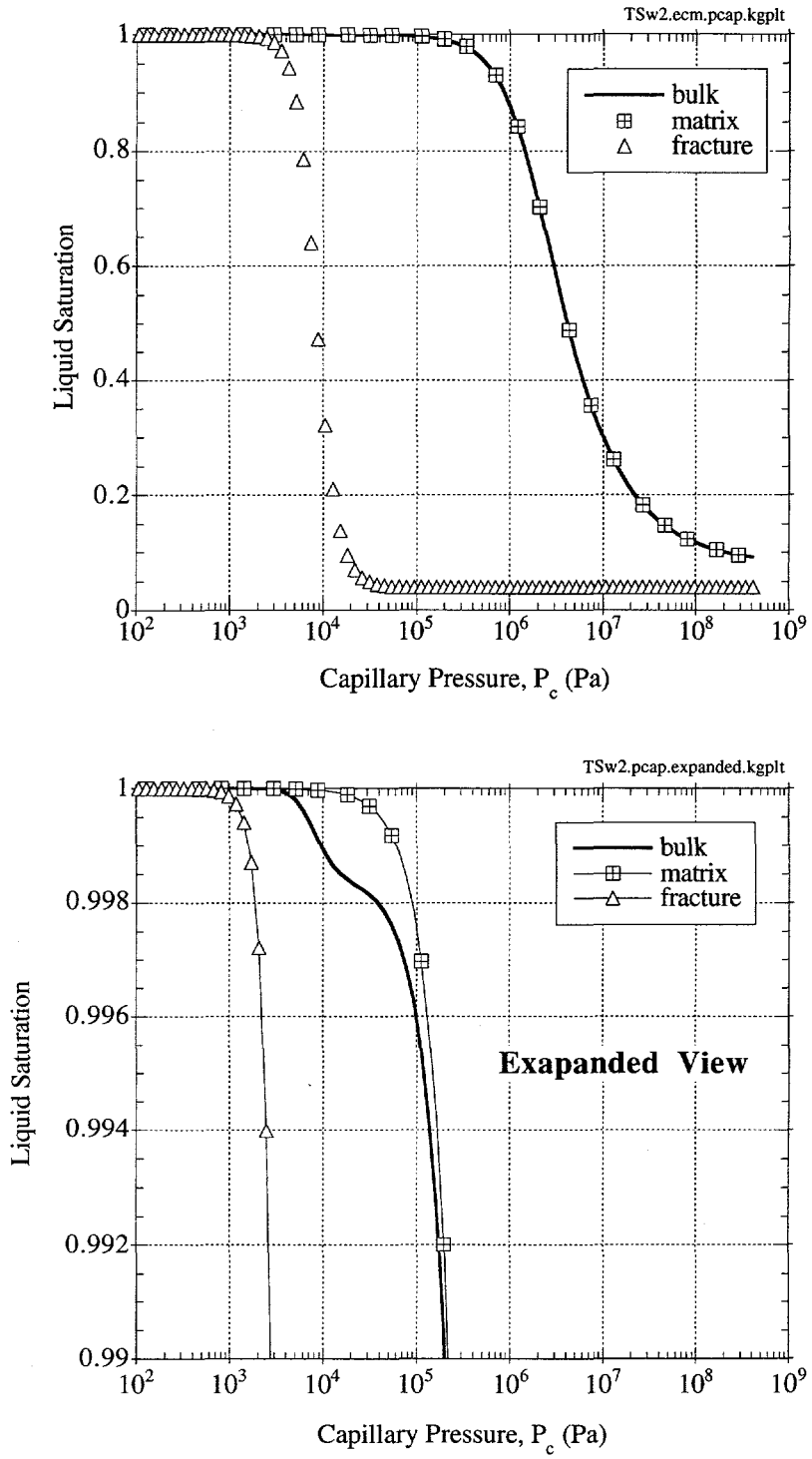

Figure A.1. Liquid saturations of the composite (bulk), matrix, and fracture materials as a function of capillary pressure for TSw2 (material parameters given in Klavetter and Peters, 1986).

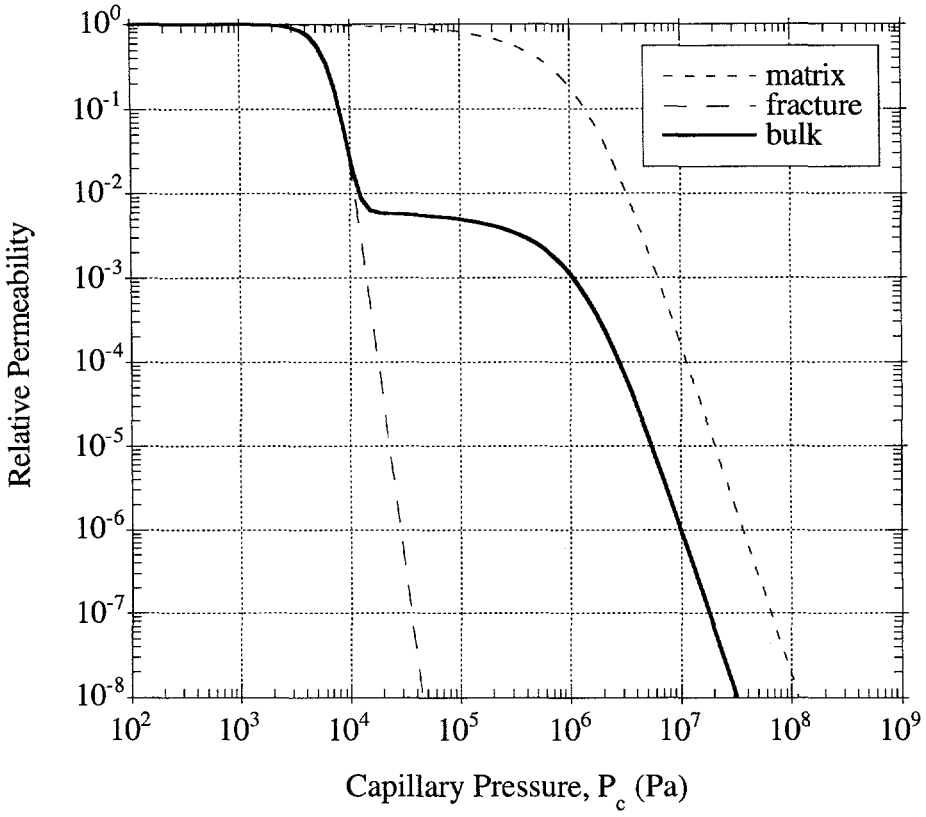

Figure A.2. Relative permeabilities of the composite (bulk), matrix, and fracture materials as a function of capillary pressure for TSw2 (material parameters given in Klavetter and Peters, 1986).

Appendix

B

Dual Permeability Fracture-Matrix Conductance in FEHMN and TOUGH2

An important parameter affecting the response of a dual permeability system is the conductance between the fractures and matrix. In FEHMN and TOUGH2, the conductance terms are defined differently, but they can be made equivalent through the proper definition of a length scale used in FEHMN. The following analysis details the formulation of the conductance terms in FEHMN and TOUGH2, which leads to the definition of an equivalent length scale for FEHMN.

B.1 Fracture-Matrix Conductance in FEHMN

The mass flow rate (kg/sec) between a fracture and matrix element in FEHMN is given by the following equation (Zyvoloski et al., 1995b):

$$\dot{m}_{f \to m} = T\left(\rho \frac{k\, k_r}{\mu}\left(P_{l,f} - P_{l,m}\right)\right) \tag{B.1}$$

where T is the geometric conductance term, ρ is the water density, μ is the water viscosity, k is the permeability, k_r is the relative permeability, $P_{l,f}$ is the liquid pressure of the fracture, and $P_{l,m}$ is the liquid pressure of the matrix. The geometric conductance term, T, is given as follows:

$$T = \frac{V}{L_{fo}^2\left(1 - \phi_f\right)} \approx \frac{V}{L_{fo}^2} \tag{B.2}$$

where V is the volume of the computational cell (m^3), L_{fo} is an input parameter defined as a length scale (m), and ϕ_f is the fracture porosity. Figure B.1 shows a sketch of flow occurring between fracture and matrix elements in a dual permeability system and the use of some of the parameters given in Equations (B.1) and (B.2).

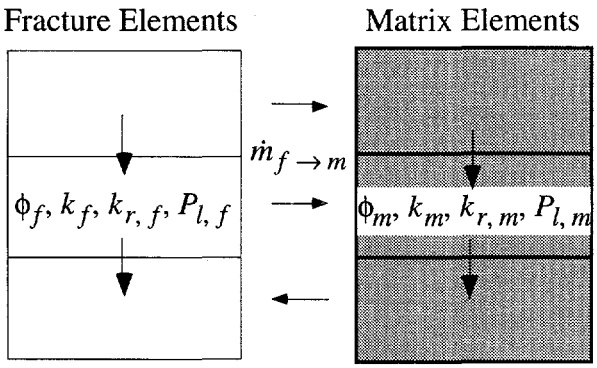

Volume of each computational cell = V
(in TOUGH2, volume of fracture elements = V• ϕ_f)

Figure B.1. Sketch of dual permeability system with mass flow occurring between the fracture and matrix elements.

B.2 Fracture-Matrix Conductance in TOUGH2

The mass flow rate (kg/sec) between a fracture and matrix element in TOUGH2 is given by the following equation:

$$\dot{m}_{f \to m} = \rho A_{f-m} \frac{k k_r}{\mu} \left(\frac{P_{l,f} - P_{l,m}}{L_{f-m}} \right) \tag{B.3}$$

where $A_{f\text{-}m}$ is the connection area between the fracture and matrix elements and $L_{f\text{-}m}$ is a distance between the fracture and matrix elements. Comparing equations (B.1) and (B.3), the geometric conductance term, T, in FEHMN is equivalent to the following term in TOUGH2:

$$T' = \frac{A_{f-m}}{L_{f-m}} \tag{B.4}$$

The connection area, $A_{f\text{-}m}$, is based on the geometry of a regular set of fractures and matrix blocks lumped into a computational cell, which is often much larger than the actual matrix block size as shown in Figure B.2.† On the matrix block scale (left sketch in Figure B.2), the connection

† Note that Figure B.2 is used only as an illustrative tool to visualize and formulate the fracture-matrix connection area. It does not represent the dual permeability computational model used in the benchmarks. Figure 1.1 shows a better representation of the computational grid used in the dual permeability models.

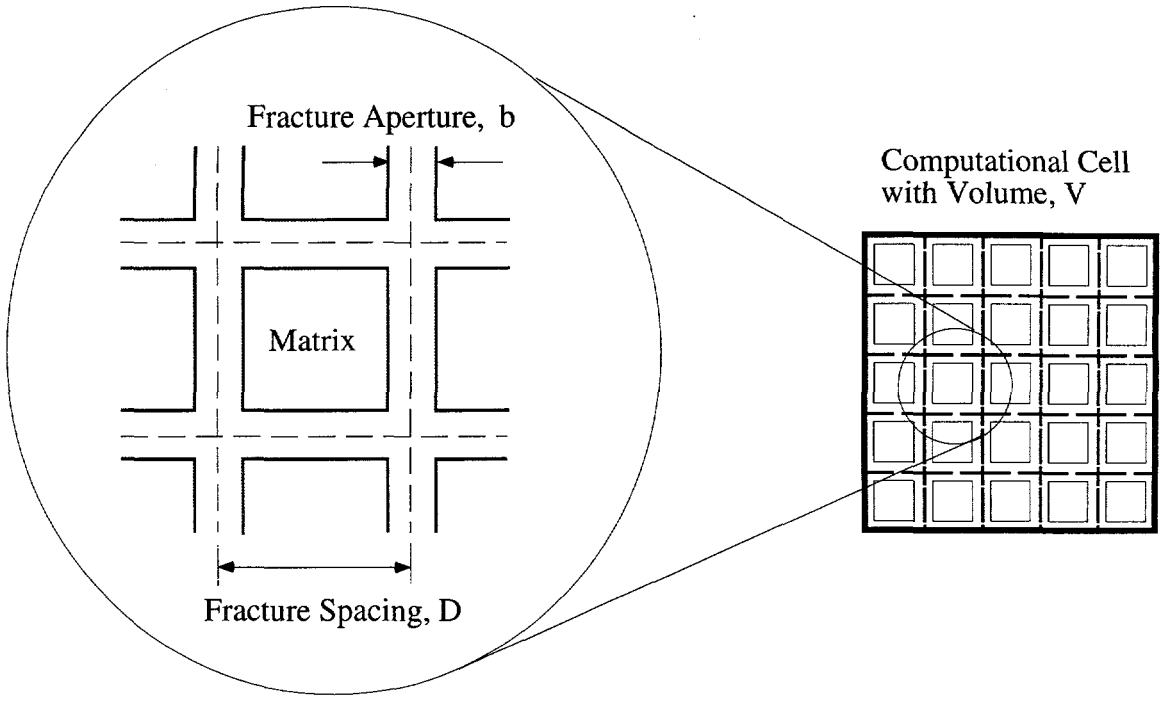

Figure B.2. Conceptual sketch of fractures and matrix blocks lumped into a computational cell for calculation of the connection area between the fracture and matrix elements.

area between the fractures and matrix can be calculated as the length of the sides of the matrix block contacting fractures. In this study, however, the fractures are assumed to be unidirectional (as opposed to bidirectional as shown in Figure B.2) based on the methods of measuring fracture frequency (spacing) from core logs. Therefore, only two sides of the matrix blocks are exposed to the fractures. In Figure B.2, this would correspond to either the vertical or horizontal set of fractures, but not both. The connection area between the fractures and matrix on the matrix block scale, $A'_{f\text{-}m}$, can then be written as follows assuming cubic matrix blocks:

$$A'_{f-m} = 2\left(D-b\right)^2 \tag{B.5}$$

The area in equation (B.5) is then multiplied by the number of matrix blocks that can occupy a single computational cell with volume, V, to yield the connection area between the fracture and matrix element on the computational scale, $A_{f\text{-}m}$:

$$A_{f-m} = A'_{f-m}\frac{V}{D^3} \approx \frac{2V}{D} \tag{B.6}$$

Equation B.6 defines the connection area between fracture and matrix elements assuming one-dimensional fracture sets in the dual permeability models used in this report. Although this relation

could also have been derived using a simpler illustration containing just parallel fractures, Figure B.2 provides a conceptual picture of how the fracture-matrix connection area can be derived using two- and three-dimensional fracture sets as well.

The distance between the fracture and matrix elements, $L_{f\text{-}m}$, is estimated based on methods described in Zimmerman et al. (1993), Pruess (1983), and Warren and Root (1963). Since only one element is used to describe the matrix, the distance used in equation (B.3) is determined such that the quasi-steady flux between the fractures and matrix is comparable to the flux between a fracture and a continuous matrix unit. For a unidirectional fracture domain assumed here, the distance is given by Pruess (1983) as follows:

$$L_{f-m} = \frac{D-b}{6} \approx \frac{D}{6} \tag{B.7}$$

Equations (B.6) and (B.7) can be used in equation (B.4) to yield the geometric conductance term for TOUGH2:

$$T' \approx \frac{12\,V}{D^2} \tag{B.8}$$

B.3 Equivalent Length Scale

If dual permeability models are to be compared between FEHMN and TOUGH2, the geometric conductance terms given in equations (B.2) and (B.8) should be equal. Equating these two equations yields the following expression for the length scale used in FEHMN as a function of the fracture spacing, D:

$$L_{fo} = \frac{D}{\sqrt{12}} \tag{B.9}$$

The length scale in equation (B.9) is input as APUV1 in the DPDP macro in FEHMN. It is interesting to note that the expression in equation (B.9) yields a conductance between the fractures and matrix (equation B.2) that is three times larger than the conductance resulting from a length scale equal to half the fracture spacing.

B.4 Important Issues

The calculated connection area between the fractures and matrix is based on the assumption that the entire area between the fractures and matrix is available to flow. This would mean that all sides of the matrix blocks shown in Figure B.2 are wetted and available for flow between the fractures and matrix. However, small scale processes such as fingering within a single fracture (Glass and Tidwell, 1991) and mechanical aspects such as fracture coatings (Thoma et al., 1990) may effectively reduce the conductance between the fractures and matrix. In addition, observations of flow in a fracture network have shown that only a fraction of the fractures are actually flowing (Nicholl and Glass, 1995). As a result, the calculated connection area between the fractures and matrix may be significantly overestimated. If only a tenth of the fracture plane is wetted due to fingering, and only a tenth of the fractures in a given region are flowing, then the connection area between the fractures and matrix can be effectively reduced by two orders of magnitude. This hypothetical reduction in the connection area has been used in several of the analyses in this report.

Finally, the permeability and relative permeability given in equations (B.1) and (B.3) also play an important role in the overall conductance between the fractures and matrix. If upstream weighting of these parameters is used in the codes, then the fracture permeabilities may be used in the calculations if flow is from the fracture element to the matrix element. Intuitively, one would think that the matrix permeabilities should be used in calculations of the flux between fractures and the matrix. In TOUGH2, if the distance between the centroid of the fracture and the interface of the fracture and matrix elements is specified as zero, then the matrix permeabilities are used (this approximation has been used in the dual permeability analyses in this report). It is unclear whether FEHMN has the capabilities to allow for a similar adjustment. If not, then the permeabilities that are used in equations (B.1) and (B.3) may be different between FEHMN and TOUGH2 when upstream weighting is used in FEHMN.

Appendix
C

RIB Information

Information from the Reference Information Base Used in this Report

This report contains no information from the Reference Information Base.

Candidate Information for the Reference Information Base

This report contains no candidate information for the Reference Information Base.

Candidate Information for the Geographic Nodal Information Study and Evaluation System

This report contains no candidate information for the Geographic Nodal Information Study and Evaluation System.

YUCCA MOUNTAIN SITE CHARACTERIZATION PROJECT

UC814 - DISTRIBUTION LIST

1 D. A. Dreyfus (RW-1)
Director
OCRWM
US Department of Energy
1000 Independence Avenue SW
Washington, DC 20585

1 L. H. Barrett (RW-2)
Acting Deputy Director
OCRWM
US Department of Energy
1000 Independence Avenue SW
Washington, DC 20585

1 S. Rousso (RW-40)
Office of Storage and Transportation
OCRWM
US Department of Energy
1000 Independence Avenue SW
Washington, DC 20585

1 R. A. Milner (RW-30)
Office of Program Management
and Integration
OCRWM
US Department of Energy
1000 Independence Avenue SW
Washington, DC 20585

1 D. R. Elle, Director
Environmental Protection Division
DOE Nevada Field Office
US Department of Energy
P.O. Box 98518
Las Vegas, NV 89193-8518

1 T. Wood (RW-14)
Contract Management Division
OCRWM
US Department of Energy
1000 Independence Avenue SW
Washington, DC 20585

4 Victoria F. Reich, Librarian
Nuclear Waste Technical Review Board
1100 Wilson Blvd., Suite 910
Arlington, VA 22209

5 Wesley Barnes, Project Manager
Yucca Mountain Site Characterization
Office
US Department of Energy
P.O. Box 98608--MS 523
Las Vegas, NV 89193-8608

1 Director
Office of Public Affairs
DOE Nevada Operations Office
US Department of Energy
P.O. Box 98518
Las Vegas, NV 89193-8518

8 Technical Information Officer
DOE Nevada Operations Office
US Department of Energy
P.O. Box 98518
Las Vegas, NV 89193-8518

1 P. K. Fitzsimmons, Technical Advisor
Office of Assistant Manager for
Environmental Safety and Health
DOE Nevada Operations Office
US Department of Energy
P.O. Box 98518
Las Vegas, NV 89193-8518

1 J. A. Blink
Deputy Project Leader
Lawrence Livermore National Laboratory
101 Convention Center Drive
Suite 820, MS 527
Las Vegas, NV 89109

2 J. A. Canepa
Technical Project Officer - YMP
N-5, Mail Stop J521
Los Alamos National Laboratory
P.O. Box 1663
Los Alamos, NM 87545

1 Repository Licensing & Quality
Assurance
Project Directorate
Division of Waste Management
US NRC
Washington, DC 20555

1 Senior Project Manager for Yucca
Mountain
Repository Project Branch
Division of Waste Management
US NRC
Washington, DC 20555

1 NRC Document Control Desk
Division of Waste Management
US NRC
Washington, DC 20555

1 Chad Glenn
NRC Site Representative
301 E Stewart Avenue, Room 203
Las Vegas, NV 89101

1 E. P. Binnall
Field Systems Group Leader
Building 50B/4235
Lawrence Berkeley Laboratory
Berkeley, CA 94720

1 Center for Nuclear Waste
Regulatory Analyses
6220 Culebra Road
Drawer 28510
San Antonio, TX 78284

2 W. L. Clarke
Technical Project Officer - YMP
Attn: YMP/LRC
Lawrence Livermore National Laboratory
P.O. Box 5514
Livermore, CA 94551

1 V. R. Schneider
Asst. Chief Hydrologist -- MS 414
Office of Program Coordination
and Technical Support
US Geological Survey
12201 Sunrise Valley Drive
Reston, VA 22092

1 J. S. Stuckless, Chief
Geologic Studies Program
MS 425
Yucca Mountain Project Branch
US Geological Survey
P.O. Box 25046
Denver, CO 80225

1 N. Z. Elkins
Deputy Technical Project Officer
Los Alamos National Laboratory
Mail Stop 527
101 Convention Center Drive, #820
Las Vegas, NV 89109

2 Michaele C. Brady
Technical Project Officer - YMP
Sandia National Laboratories
Organization 6302, MS 1399
101 Convention Center Drive, Suite 880
Las Vegas, NV 89102

1 Ray Wallace
US Geological Survey
106 National Center
12201 Sunrise Valley Drive
Reston, VA 22092

1 L. R. Hayes
Technical Project Officer
Yucca Mountain Project Branch
MS 425
US Geological Survey
P.O. Box 25046
Denver, CO 80225

1 A. L. Flint
US Geological Survey
MS 721
P.O. Box 327
Mercury, NV 89023

1 R. E. Lewis
Yucca Mountain Project Branch
MS 425
US Geological Survey
P.O. Box 25046
Denver, CO 80225

1 D. Zesiger
US Geological Survey
101 Convention Center Drive
Suite 860, MS 509
Las Vegas, NV 89109

2 L. D. Foust
Nevada Site Manager
TRW Environmental Safety Systems
101 Convention Center Drive
Suite P-110, MS 423
Las Vegas, NV 89109

1 C. E. Ezra
YMP Support Office Manager
EG&G Energy Measurements Inc.
MS V-02
P.O. Box 1912
Las Vegas, NV 89125

1 E. L. Snow, Program Manager
Roy F. Weston, Inc.
955 L'Enfant Plaza SW
Washington, DC 20024

1 Technical Information Center
Roy F. Weston, Inc.
955 L'Enfant Plaza SW
Washington, DC 20024

1 Technical Project Officer - YMP
US Bureau of Reclamation
Code D-3790
P.O. Box 25007
Denver, CO 80225

1 B. T. Brady
Records Specialist
US Geological Survey
MS 421
P.O. Box 25046
Denver, CO 80225

1 M. D. Voegele
Technical Project Officer - YMP
M&O/SAIC
101 Convention Center Drive
Suite 407
Las Vegas, NV 89109

1 Paul Eslinger, Manager
PASS Program
Pacific Northwest Laboratories
P.O. Box 999
Richland, WA 99352

1 A. T. Tamura
Science and Technology Division
OSTI
US Department of Energy
P.O. Box 62
Oak Ridge, TN 37831

1 P. J. Weeden, Acting Director
Nuclear Radiation Assessment Div.
US EPA
Environmental Monitoring Sys. Lab
P.O. Box 93478
Las Vegas, NV 89193-3478

1 ONWI Library
Battelle Columbus Laboratory
Office of Nuclear Waste Isolation
505 King Avenue
Columbus, OH 43201

1 C. H. Johnson
Technical Program Manager
Agency for Nuclear Projects
State of Nevada
Evergreen Center, Suite 252
1802 N. Carson Street
Carson City, NV 89710

1 John Fordham, Deputy Director
Water Resources Center
Desert Research Institute
P.O. Box 60220
Reno, NV 89506

1 The Honorable Cyril Schank
Chairman
Churchill County Board of
Commissioners
190 W. First Street
Fallon, NV 89406

1 T. Hay, Executive Assistant
Office of the Governor
State of Nevada
Capitol Complex
Carson City, NV 89710

3 R. R. Loux
Executive Director
Agency for Nuclear Projects
State of Nevada
Evergreen Center, Suite 252
1802 N. Carson Street
Carson City, NV 89710

1 Brad R. Mettam
Inyo County Yucca Mountain
Repository Assessment Office
P. O. Drawer L
Independence, CA 93526

1 Lander County Board of Commissioners
315 South Humbolt Street
Battle Mountain, NV 89820

1 Vernon E. Poe
Office of Nuclear Projects
Mineral County
P.O. Box 1600
Hawthorne, NV 89415

1 Les W. Bradshaw
Program Manager
Nye County Nuclear Waste Repository
Project Office
P.O. Box 1767
Tonopah, NV 89049

1 Florindo Mariani
White Pine County Coordinator
P. O. Box 135
Ely, NV 89301

1 Judy Foremaster
City of Caliente Nuclear Waste
Project Office
P.O. Box 158
Caliente, NV 89008

1 Philip A. Niedzielski-Eichner
Nye County Nuclear Waste
Repository Project Office
P.O. Box 221274
Chantilly, VA 22022-1274

1 Dennis Bechtel, Coordinator
Nuclear Waste Division
Clark County Department of
Comprehensive Planning
301 E. Clark Avenue, Suite 570
Las Vegas, NV 89101

1 Juanita D. Hoffman
Nuclear Waste Repository
Oversight Program
Esmeralda County
P.O. Box 490
Goldfield, NV 89013

1 Eureka County Board of Commissioners
Yucca Mountain Information Office
P.O. Box 714
Eureka, NV 89316

1 Economic Development Dept.
City of Las Vegas
400 E. Stewart Avenue
Las Vegas, NV 89101

1 Community Planning & Development
City of North Las Vegas
P.O. Box 4086
North Las Vegas, NV 89030

1 Community Development & Planning
City of Boulder City
P.O. Box 61350
Boulder City, NV 89006

1 Commission of European Communities
200 Rue de la Loi
B-1049 Brussels
BELGIUM

2 Librarian
YMP Research & Study Center
MS 407
P.O. Box 98521
Las Vegas, NV 89193-8521

1 Amy Anderson
Argonne National Laboratory
Building 362
9700 S. Cass Avenue
Argonne, IL 60439

1 Glenn Van Roekel
Director of Community Development
City of Caliente
P.O. Box 158
Caliente, NV 89008

1 G. S. Bodvarsson
Head, Nuclear Waste Department
Lawrence Berkeley Laboratory
1 Cyclotron Road, MS 50E
Berkeley, CA 94720

1 Michael L. Baughman
Intertech Services Corp.
P.O. Box 93537
Las Vegas, NV 89193

1 L. Berkowitz
TRW ESS
600 Maryland Ave., SW
TES2/601F
Washington, DC 20024

1 G. Zyvoloski
Los Alamos National Laboratory
EES-5, MS-F665
Los Alamos, NM 87545

1 B. Robinson
Los Alamos National Laboratory
EES-5, MS-F665
Los Alamos, NM 87545

1 A. Wolfsberg
Los Alamos National Laboratory
EES-5, MS-F665
Los Alamos, NM 87545

1 J. Fabryka-Martin
Los Alamos National Laboratory
CST-7, J514
Los Alamos, NM 87545

1 K. Pruess
Earth Sciences
Lawrence Berkeley Laboratory
1 Cyclotron Road, 50E
Berkeley, CA 94720

1 Y. Tsang
Earth Sciences
Lawrence Berkeley Laboratory
1 Cyclotron Road, 50E
Berkeley, CA 94720

1 R. Zimmerman
Earth Sciences
Lawrence Berkeley Laboratory
1 Cyclotron Road, 50E
Berkeley, CA 94720

1 T. Buscheck
Lawrence Livermore National Laboratory
P. O. Box 808, L-206
Livermore, CA 94550

1 L. Flint
U. S. Geological Survey
P.O. Box 327, MS 721
Mercury, NV 89023

1 D. Hudson
U. S. Geological Survey
P.O. Box 327, MS 721
Mercury, NV 89023

1 E. Kwicklis
U. S. Geological Survey
Box 25046, MS 421
Lakewood, CO 80225

1 D. Hoxie
U. S. Geological Survey
101 Convention Center Drive, Suite 860
Las Vegas, NV 89109

1 Y. Chen
UNLV
Department of Mechanical Engineering
4505 Maryland Parkway
Box 454027
Las Vegas, NV 89154-4027

1 B. Boehm
UNLV
Department of Mechanical Engineering
4505 Maryland Parkway
Box 454027
Las Vegas, NV 89154-4027

1 J. Duguid
M&O INTERA
101 Convention Center Drive
TES1/8564
Las Vegas, NV 89109

1 Y. Xiang
INTERA, Inc.
TRW Environmental Safety Sys. Inc.
101 Convention Center Drive, Suite 110
Las Vegas, NV 89109

1 C. Li.
INTERA, Inc.
101 Convention Center Drive
Las Vegas, NV 89109

1 M. Reeves
INTERA, Inc.
6850 Austin Center Blvd., Suite 300
Austin, TX 78731

1 S. Lingineni
CRWMS/M&O
101 Convention Center Drive
Las Vegas, NV 89109

1 R. W. Nelson
INTERA, Inc.
TRW Environmental Safety Sys. Inc.
101 Convention Center Drive, MS-425
Las Vegas, NV 89109

1 W. Zhou
INTERA, Inc.
3609 South Wadsworth Blvd., #550
Denver, CO 80235

1 E. Smistad
Department of Energy
101 Convention Center Drive
P200-216
Las Vegas, NV 89109

1 Abe Van Luik
101 Convention Center Drive
P200-219
Las Vegas, NV 89109

1 A. Simmons
YMSCO
101 Convention Center Drive
Las Vegas, NV 89109

1 R. Green
CNWRA
6220 Culebra Road
San Antonio, TX 78238-5166

1 R. G. Baca
CNWRA
6220 Culebra Road
San Antonio, TX 78238-5166

Qty.	MS	Name, Org.
2	1330	C. B. Michaels, 6352 100/1.2.5.4.4/SAND95-1546/QA
20	1330	NWMT Library, 6352
1	1326	H. A. Dockery, 6312
5	1326	S. J. Altman, 6312
5	1326	B. W. Arnold, 6312
1	1326	R. W. Barnard, 6312
1	1326	G. E. Barr, 6312
1	1326	N.D. Francis, 6312
1	1326	J. H. Gauthier, 6312
1	1326	G. W. Perkins, 6312
1	1326	T. H. Robey, 6312
1	1326	S. A. Shannon, 6312
1	1326	A. Schenker, 6312
1	1326	L. H. Skinner, 6312
1	1326	M. L. Wilson, 6312
1	1325	L. S. Costin, 6313
1	1324	P. B. Davies, 6115
1	1324	M. Cromer, 6115
1	1324	R. J. Glass, 6115

20	1324	C. K. Ho, 6115
1	1324	S. A. McKenna, 6115
1	1324	L. Meigs, 6115
1	1324	C. A. Rautman, 6115
1	1324	V. C. Tidwell, 6115
1	1324	S. W. Webb, 6115
1	0827	M. Martinez, 1511
1	0835	R. R. Eaton, 1511
1	9018	Central Technical Files, 8523-2
5	0899	Technical Library, 13414
1	0619	Print Media, 12615
2	0100	Document Processing, 7613-2 for DOE/OSTI